Active Brownian motion in a narrow channel

Xue Ao

Active Brownian Motion in a Narrow Channel

Dissertation

zur Erlangung des akademischen Grades

Dr. rer. nat.

eingereicht an der

Mathematisch-Naturwissenschaftlich-Technischen Fakultät

der Universität Augsburg

Von

Xue Ao

Dezember 2014

Universität
Augsburg
University

Erstgutachter: Prof. Dr. Peter Hänggi

Zweitgutacher: Prof. Dr. Hubert Krenner

Tag der mündlichen Prüfung: 9. Jan. 2015

Dedicated to my parents.

Contents

List of Figures

Abbreviations

1D	one Dimensional
2D	two Dimensional
3D	three Dimensional
BM	Brownian Motion
JP	Janus Particle
FJ	Fick-Jacobs
MSD	Mean-Squared Displacement
PDF	Probability Density Function
GPU	Graphic Processing Unit
CUDA	Compute Unified Device Architecture

Chapter 1

Introduction

1.1 Active particles: Molecular motors

Nature has amazingly fabricated biological machines with molecular elements which are responsible for most forms of movement encountered in the cellular realm [1]. These molecular machines are able to transport chemical energy and provide numerous functions for cell, such as synthesizing specific molecular products and pumping as a motor which are able to convert chemical energy into the specifically directed motion. Since the molecular machines do not act in isolation but to achieve their functions cooperatively, the cell is like a factory including complex organizations of the motors carrying on biochemical activities [2–4].

Among the molecular motors within the cell, the best known are the cytoplasmic motors. They can use sophisticated mechanisms to take nanometer steps along tracks in the cytoplasm delivering the necessary cargoes, even under the influence of strong thermal fluctuations. Myosins move along the actin filaments, while dyneins and kinesins take microtubules as their substrate of routes [5], illustrated in Fig.

1.1. Thus for such purpose of active transport, these small motors adhering the filaments are undergoing the bias random walk.

This interesting biological fact gives rise to a question, that is, whether we can artificially create such smart micron and nanoscale machines which can execute the equivalent or similar functions as biological systems perform [6, 7]? Obviously, one way is to simply copy the structure existing in biology which can be experimentally programmable. Specifically, the nucleotide sequences can be delicately programmed for the purpose of realizing certain functions, such as asymmetric ligation and cleavage, as well as changing its conformation in designed landscapes. As the development of imitating the motion of molecular motor in biology, artificial molecular walkers have been synthesized by experimentalists [6, 8–17]. Another way is to create artificial motors under the assistance of external fields. Examples are the mimic flagellar movement triggered by magnetic fields and thermally activated nano-electromechanical motors [16]. Various kinds of motors driven by electric fields or photochemical stimuli can possess functions as sockets (see Fig. 1.2(a)), switches, rotors, brakes, rotaxane and ratchets [17–24].

Besides these two attempted methodologies, another approach is to design synthetic nanomotors, neither with the help of configuration changes controlled by programmed biological sequence, nor with the presence of an external field. The idea is to construct micro or nanomotor moving directly powered chemically, without moving part. In short, by producing asymmetric-distributed chemical reacts around, the swimmers without moving parts can make a directed motion spontaneously due to phoresis mechanism. For instance, illustrated in Fig. 1.2(b,c), a half-coated particle is able to self-propell
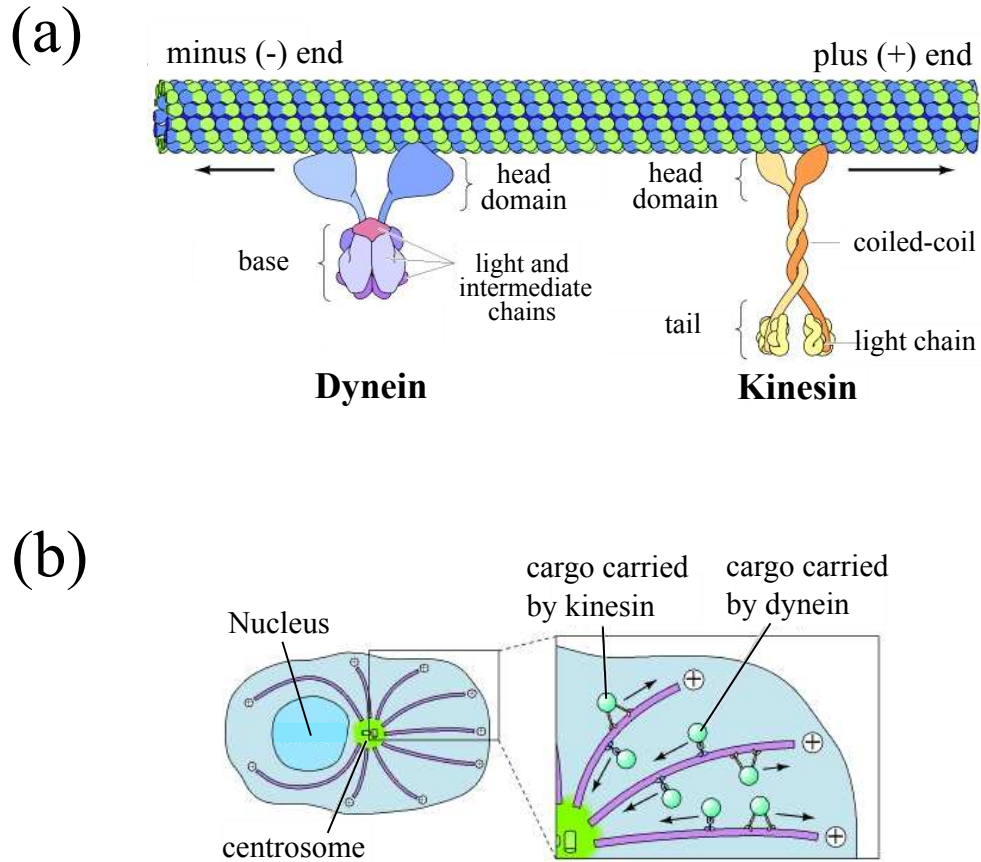
FIGURE 1.1: Biological active transport by motor proteins, adopted from Ref. [1]. (a) Microtubule motor proteins: dyneins and kinesins. (b) Transport of vesicles (cargos) along the microtubules in the cell, carried by motor proteins.

in the suspension with the presence of light. While this two-faced "Janus particle" (JP) is illuminated, the coated side is heated above a critical temperature T_c, which results in a local demixing that finally propels the particle [25].

The conception of fabricating a self-propelled motor is very promising, as it can avoid miscellaneous procedures, such as designing conformational dynamics, building up tracks, or programmed landscapes for directing their motion, as well as bringing forth an external field [7]. In last decade, fascinate discoveries have been explored for active swimmers or particles due to the development of appropriate synthesis methods [26–35]. Many topics address the physics properties of

self-propelled particles, such as self-assembly. In this thesis, we focus on the diffusive random motion of the self-propelled microscopic swimmers suspended in the low Reynolds fluid, which is called "active Brownian motion", compared with passive Brownian motion of traditional particles.
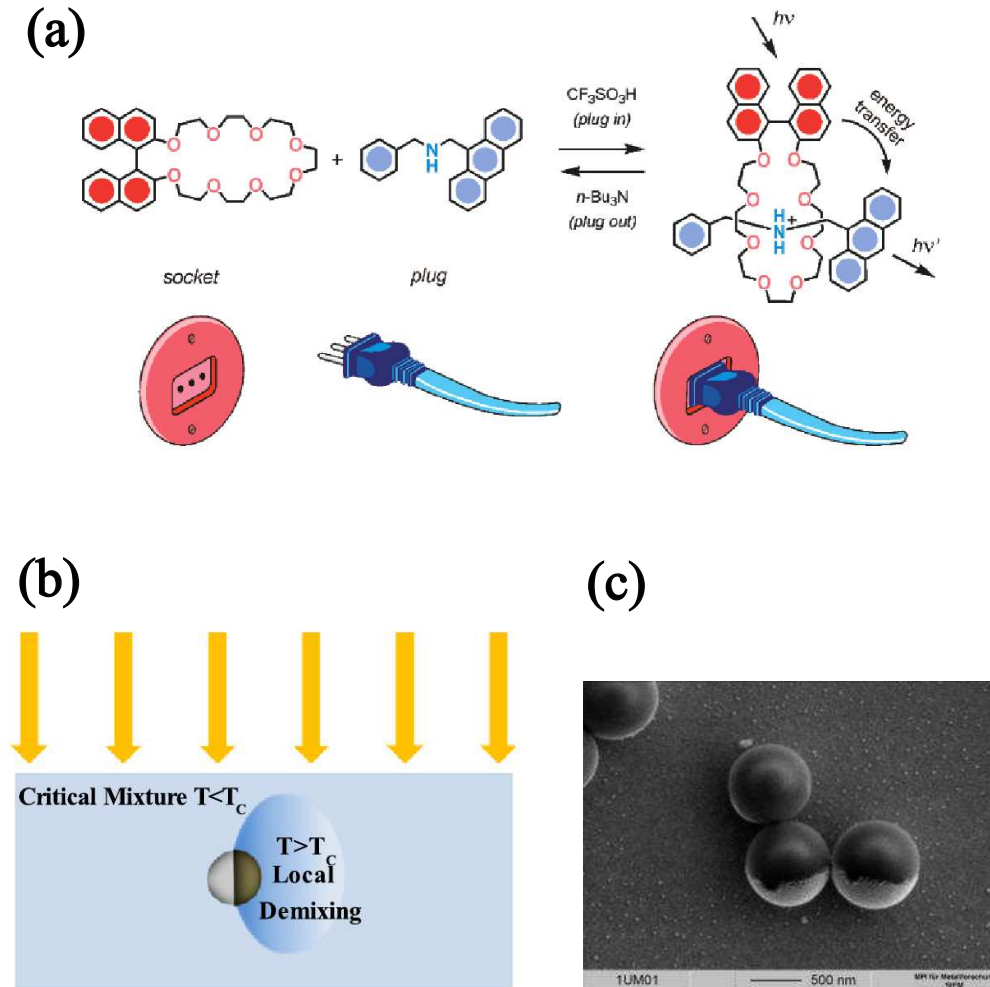
FIGURE 1.2: Artificial molecular machine and self-propelled motor. (a) Artifical molecular socket is shown, with the plug in state resulted by photo-induced energy transfer, adopted from Ref. [6]. (b) Schematic explanation of self-propulsion mechanism of a without a moving part or an external field. A JP is illuminated and the cap is heated above T_c inducing a local demixing that eventually propels the particle. adopted from Ref. [25].

1.2 Brownian motion: Overview of the history

It is known that the diffusion universally happens in all states of matter over an extremely wide time variation. It plays a significant role in physical, chemical, and biochemical processes [36]. Fick's second law provide the macroscopic description of diffusion [37]. From a microscopic aspect, the diffusion is actually the stochastic process consist of the erratic motion of suspended articles. Such random motion is called Brownian motion (BM), with a name after the botanist Robert Brown, who first systematically studied this erratic motion [38].

Based on the molecular-kinetic theory of heat, Albert Einstein proposed the theory connecting microscopic dynamics underlying in suspension and the macroscopic observations around 1905 [39, 40]. In his theory, he provided the derivation of the diffusion coefficient in the function of the fluid viscosity. Around the same time, this relation was confirmed by other theoretical studies with various approaches by William Sutherland [41], Marian von Smoluchowski [42], and Paul Langevin [43]. Based on this Stokes-Einstein relation, the fluctuation-dissipation theorem was generalized in 1951 [44], and followed by the linear response theory found by Ryogo Kubo later in 1957 [45].

It has been a long and tough road towards the high-resolution time measurements of BM over the last century, after the experimental confirmation performed by Jean Perrin [46]. In favor of developed techniques, the energy equipartition theorem thus can be proved with direct evidences [47], and the entire transition from ballistic to diffusive BM can be detected [48].

It is necessary to mention that the original theory for BM is limited to treat free Brownian particles. More practically, more realistic situations are needed to be considered, such as the particles moving in a potential energy landscape or constricted spatially in a geometry. Those may result in a diffusion which is remarkably different from the bulk diffusion of free case, and both experimental and theoretical studies have been underway in this field.

1.3 Patterned structures as confined geometries

Confined BM is ubiquitously occurring in the geometrical confinement in nature such as cells, as well as in artificial patterned structures contributed by experimental development of passing two decades [49–72]. From the natural occurrence to artificial microdevice, zeolites [52, 73], ion channels [49, 56, 74, 75], artificial nanopores [76, 77] as well as microfluidic devices [59, 60, 78] are explored elaborately for deep understanding. Here we mainly address a few types of confined geometry mentioned in the next paragraph.

Zeolites, crystalline aluminosilicates with 3D structure, are studied and developed as a variety of applications since the 1960's [79]. In the forms of microporous patterns, they mainly consist of silicon and oxygen atoms, like the sand. The silicon atom is surrounded by oxygens, forming a tetrahedral "block". With these basic blocks, uncountable types of structure can be constructed with pores in 1D, 2D or 3D [79, 80], illustrated in Fig. 1.3(a,b). The diffusion through channels and pores in zeolites is much different than bulk diffusion, for which zeolites can be *molecular sieves* filtering molecules according to size, shape and polarity [81, 82].
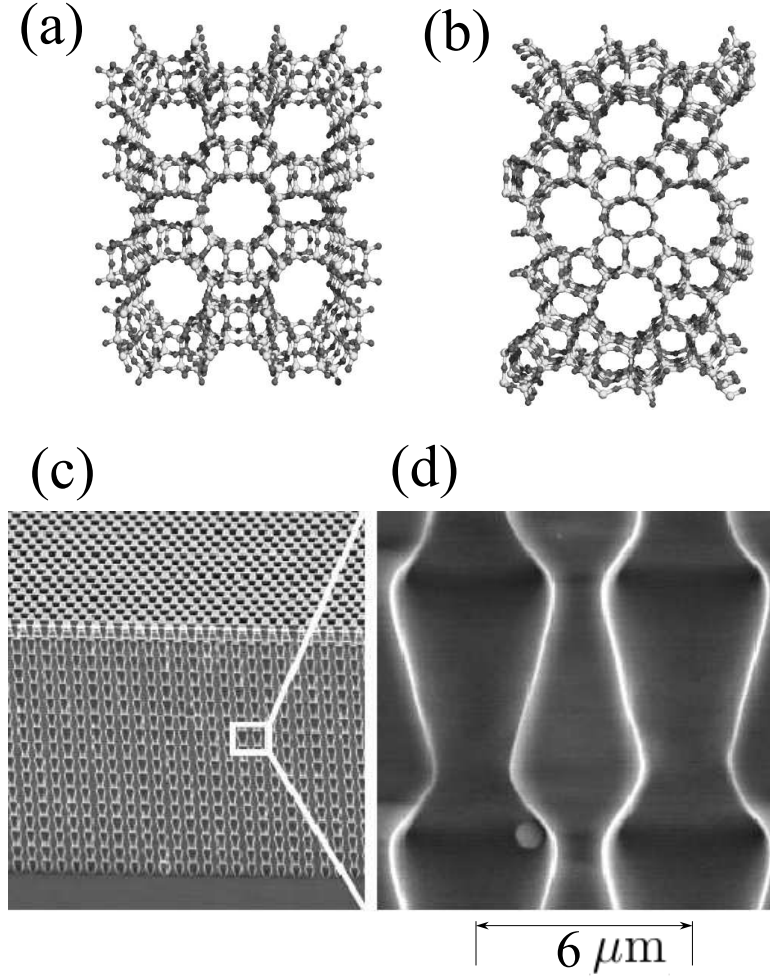
FIGURE 1.3: Zeolites and microchannels as examples of confined geometries. (a)(b) Adopted from Ref. [79], the structures of zeolites mordenite (a) and silicalite (b) are shown, with clearly visible pores. (c) Scanning electron micrograph of a cleaved modulated macroporous silicon wafer. (d) Scanning electron micrograph of a cleaved modulated macroporous silicon ratchet membrane. (c)(d) are adopted from Ref. [60].

Microchannels, acting as Brownian ratchets, can induce the directed motion of Brownian particles [59, 60, 78]. Due to the geometrical variation along the transport direction, as the example shown in Fig. 1.3(c,d), the particle dynamics can be boosted or restricted by the corresponding entropic barriers. There are various achievements of these microchannels to manipulate and design functional devices such as size-dependent separators [55, 56, 60, 61, 83–86]. The numerical and analytical studies are in progress for a better understanding [87, 88].

Limited by the geometric restrictions, the particle dynamics turns out to be suppressed and in some situations rectified [89, 90]. The nonhomogeneity of the confinement structures can play an important role for practical functions and producing uncommon properties [65, 70]. Theoretical studies in earlier years are carried out on cellular processes, such as molecular transport through membranes [58, 91–93]. Motivated from this, the particle transport in microdomains with small openings is extensively investigated [94, 95]. This issue is called Brownian transport in "entropic barriers", which is a more generalized and basic problem schematized by the Fick-Jacobs approach [62]. The regulation functions produced by the confinements with specific shape is found to lead to some interesting transport properties [68]. Studies for deep and detailed understanding of the confined transport of Brownian particles are carried out [69, 70, 88, 95–98], for the development of applications in biology and materials.

1.4   Outline

Motivated by the significance of biology, within this thesis, we focus on the diffusion process of the non-chiral and chiral active swimmers in narrow corrugated channels. With respect of the impossibility of fully analytical solution of Fokker-Planck equations with non-flat boundary, we employ the Langevin approaches for modeling the bulk dynamics, and the confined active BM is simulated numerically by solving the finite difference equations under the sliding boundary condition. Considering confined geometries with different asymmetry, we analyze the parameter dependence of the autonomous current

and diffusivity, and discuss the role of chirality and geometrical asymmetry of the confinement on affecting the function of autonomous rectification.

This thesis is organized as follows: In Chap. 2, we overview the experimental works and elaborate the self-propulsion mechanisms of active particles. Previous modeling by Langevin approach is correspondingly retrospected. In Chap. 3, we address the issue of traditional Brownian transport in confinement, and introduce the Fick-Jacobs approach as an approximation for solving the effective diffusion coefficient. In Chap. 4, we first introduce the Langevin equation for active particles in bulk, and then combined with a proposed boundary algorithm, the procedures for numerical study on the confined active motion are presented. In Chap. 5, we investigate on the autonomous rectification of JPs due to the asymmetric confinement. According to the asymmetry, two categories of channels are distinguished: left-right asymmetric channels and upside-down asymmetric channels. It is proved that the chirality is required for ratcheting in upside-down asymmetric channels. The minimal asymmetry requirements for rectification is discussed. In Chap. 6, we investigate the diffusion of nonchiral and chiral active particles numerically in confinement with different geometries. In particular, we find that the diffusivity is controlled by the chirality, rather than the channel geometry.

Chapter 2

Active Brownian Motion

Microswimmers performing directed motion, are rather different from traditional Brownian particles which are dominated by thermal fluctuations. Since some decades ago, self-propelled particles have been widely found and studied in biological systems, such as the actin polymerizing bacteria *Listeria* monocytogenes in cells and *E. Coli* bacteria probing their surrounding medium [99–102]. Recently, non-biological microswimmers are created and have been investigated, which can transform chemical energy into kinetic energy making use of self-diffusiophoretic and self-electrophoretic force. With these artificial microswimmers, numerous promising applications in several fields can be realized, such as drug delivery through tissues and performances in lab-on-a-chip devices [103–105].

In this chapter, we introduce the active particles from motivations to the mechanism of self-propulsion, with sketches of several experiments and theoretical model in Langevin approach. According to recent experiments, this scheme is thus extended by considering self-propulsion force with varying direction, which leads to the chiral active motion. A corresponding model is introduced for the dynamics of free chiral active particles.

2.1   Motivation

Biological transport issues possess much importance, such as moving nanoscale components for the purpose of building molecular machines, and drug delivering by nano-particles to the specific targets [103]. It is found that nanoscale components are likely be transported with the assistance of artificial swimming devices in similar size. For this reason, significant developments in nanotechnology have been recently achieved for swimming devices with the potential for supporting biological transport [106].

It deserves to be mentioned that, a number of challenges for this task need to be considered when we look into the system on these length scales in fluid [107]. First consider the ordinary swimming mechanism for a human being in water. The directed movement can be achieved after the periodic body motions, from which the body can obtain a directed momentum from surrounding water [108]. However, situation is in much difference for miniature devices immersed in fluid. The microscopic objects can swim with velocities of the order of $1\mu\mathrm{m}\cdot\mathrm{s}^{-1}$, with the corresponding Reynolds numbers of the order of 10^{-4}. With the inertial effects considered to be ignored, it rules out the ordinary swimming mechanism mentioned is unavailable to achieve net progress due to the time-reversible dynamics of the micro-objects [109]. One of examples is "scallop" with one ringlet is not able to swim but only make a reciprocal motion by constantly uttering its arms, which is described by Purcell in his pioneering work [110].

Another challenge is to overcome the randomized orientation induced

by the ubiquity of BM. Endowed with randomly rotation by thermal force, it is impossible for a symmetrical microscopic object to maintain moving in a certain direction without the help of a proper steering mechanism or an external bias. It is remarkable that the Nature overcomes such molecular transport problem by developing protein tracks in the cytoplasm, which can constrict the molecular motors with cargo in order to avoid perturbations [5, 111].

Faced with the challenges mentioned above, ideally the microswimmers should autonomously play active movement without external steering tracks or bias force. Practically, it is due to the biological facts that it is difficult to create such nano-tracks or powering fields for transport. Besides, the principal of minimizing external interventions is always expected to achieve more sufficient transport processes [107]. This chapter focuses on a class of self-motile microscopic devices, designed out of the idea of autonomous chemical power producing as well as asymmetry. The general principal of this kind of swimmers is to generate an asymmetry in their surroundings by catalytic decomposition of a dissolved fuel in their surface, which can result in self-propulsion.

2.2 Self-propulsion mechanisms

2.2.1 Overview of experimental works

Two decades ago as early studies, the propelled motion of millimeter-scale objects were investigated by Whitesides's group, with the propulsion provided by the catalytic decomposition of hydrogen peroxide occurring on a Pt surface [112]. They explored that the synthesized active swimmers were propelled away from their Pt-coated sites, by

the propulsion generated from the production of O_2 bubbles, which was the result of the decomposition of H_2O_2.

Later, self-propelled nano-rods were proposed and realized by Mallouk and co-workers [29, 113–115]. They prepared the nano-rods with Au and Pt in contact with one another, and used the dilute solution of H_2O_2 as the suspension. A localized electrophoretic and proton field was generated due to the electrodeposition of Au and Pt, which prompted the nano-rods moving to the direction of their Pt ends. Extensive studies have provided numerous approaches for self-propelled nano-rod systems making use of such self-electrophoresis mechanism [27, 28, 30, 33, 116–124]

Recently, a study of self-propelled spherical particles with on coated side was reported by Howse and his co-workers [26]. They showed that the Pt-coated polystyrene particles can be self-propelled sufficiently in the dilute H_2O_2 suspension, due to self-diffusiophoresis mechanism. Further analysis were carried out following this study [34]. As a most recent development, a novel approach for generating self-propulsion of a half-coated particle was proposed by Vople *et al.*, with the assistant of illumination for tuning of self-propulsion velocity [125].

There are also other realizations of self-propulsion microswimmers, such as sphere dimer [30, 35] and micromotors with geometric asymmetry [126, 127]. In this section, we focus on the introduction of the two ordinary mechanisms for generating self-propulsion: self-electrophoresis and self-diffusiophoresis mechanism.

Phoresis is a term originally from biology describing interspecies biological interaction in ecology [128]. The colloidal particles will move if they are immersed in a fluid with a gradient of external fields, thus

phoretic transport occurs due to the consequence of the interaction between an inhomogeneous field with the interfacial boundary region of the individual particle [129–134]. The phoresis can be in different types due to varying kinds of the external fields. If the external field is resulted from an electrical potential, it is electrophoresis that caused. Similarly, the diffusiophoresis is due to the concentration gradient of neutral particles, and thermophoresis induced by a temperature gradient and osmophoresis arising from an osmotic pressure gradient [7].

2.2.2 Self-electrophoresis mechanism

Electrophoretic transport as mentioned occurs in an applied electric field, which drifts a charged particle moving in the electrostatic Coulomb force. If the electric field is not externally applied but generated by the particle itself, the self-propulsion motion of the particle can be achieved by such *self-electrophoresis* mechanism. Based on this scheme, the pioneering experimental work by Paxton *et al.* has made this type of self-propulsion swimmer realized by the bi-metallic nano-rods [114, 119].

The scheme of Paxton's work is illustrated in Fig. 2.1. With diameter of 370 nm and in the length of 2 μm, the nano-rod is synthesized with the platinum and gold ends, the self-electrophoretic force can be resulted from electro-chemical hydrogen peroxide decomposition at both ends. In particular, oxidation of Pt and reduction of Au occur on opposite ends, which would generate its own ion gradient. In fact, platinum is known as a catalyst for the non-electrochemical decomposition of hydrogen peroxide without the help of another electrode. However, the oxidation of H_2O_2 on a platinum electrode is applied
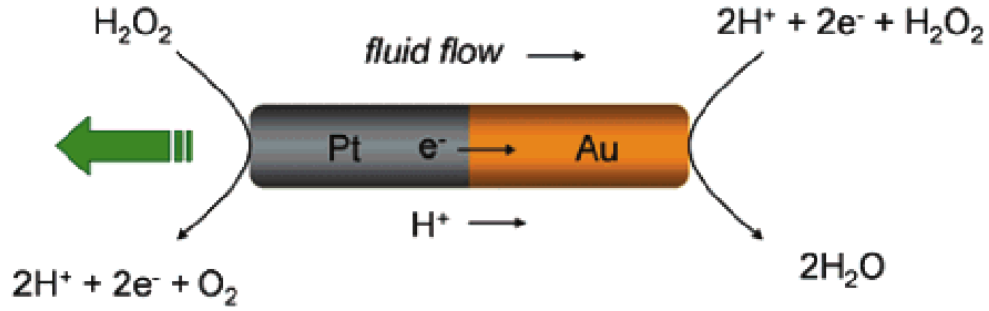
FIGURE 2.1: A schematic illustration of self-electrophoresis, adopted from [114]. Hydrogen peroxide is oxidized to generate protons in solution and electrons in the wire on the Pt end. The protons and electrons are then consumed with the reduction of H_2O_2 on the Au end. The ion flux induces motion of the particle relative to the fluid, propelling the particle toward the platinum end with respect to the stationary fluid.

as a connection to the reduction of H_2O_2 on the surface of Au at the opposite end of the rods, following the reactions:

$$\text{Pt}: \quad H_2O_2 \;\rightarrow\; O_2 \;+\; 2H^+ + 2e^-,$$

$$\text{Au}: \quad H_2O_2 \;+\; 2H^+ \;+\; 2e^- \;\rightarrow\; 2H_2O.$$
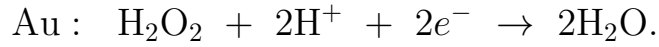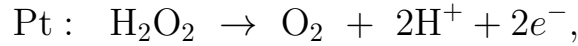
There is a measurable current on the surface of a Pt/Au rod from platinum end to gold end in the operative experiment. Obeying the conservation law of charge and the stoichiometry of the reactions, an ion current carried by the counter-ion H^+ in the solution between the electrodes will give rise to a net charge transport as accompany with the electron current. This will cause the particle migration with a velocity U_{eq} that predicted by the Helmholtz-Smoluchowski equation [119, 135]:

$$U_{\text{eq}} \;=\; \frac{\mu_e J}{k}. \tag{2.1}$$

In this relation Eq. 2.1, μ_e represents the electrophoretic mobility of the bimetallic particle, which turns out as a function of the dielectric constant, the solution viscosity, *etc*. The current density is denoted by J which is resulted from the electrochemical reactions,

and the conductivity of the solution in bulk is denoted by k. This relationship predicts that the fluid velocity is proportional to the current and inversely proportional to the solution conductivity, and the authors test this electrokinetic hypothesis by experimental strategies and obtained the nano-rod with the maximum self-propulsion velocity as 6.6 μm $\cdot$ s^{-1} [119].

In Ref. [119], the authors also relate this issue to an hypothetical system proposed by Anderson [136] and by Lammert *et al.* [137], that an active transport can be carried on to pump ions *etc.* entering the cell on one end and ejected at the other. The dynamic electric field caused by the gradient is preserved tangential to the surface of the cell. With the ion-pumping process going on, this gradient will be superimposed over cellular double layer in steady state. Under the dynamic electric field, ions within the cellular double layer will be drifted, which leads to the streaming of the fluid in the interfacial area. Consequently, a slip velocity is generated as a propulsion.

2.2.3 Self-diffusiophoresis mechanism

Diffusiophoresis describes a spontaneous movement of particles in a fluid, which is caused by the concentration gradients across a particles interfacial region [136]. Reported in Ref. [138], that diffusiophoresis is able to induce migration of particles towards higher salt areas with a diffusion rate fifty times larger than that of Brownian diffusion. This type of discoveries provides a suggestion of self-propulsion mechanism that the object can generate the interfacial gradients by chemical reactions taking place on specific parts of its surface, termed by *self-diffusiophoresis* mechanism [107].
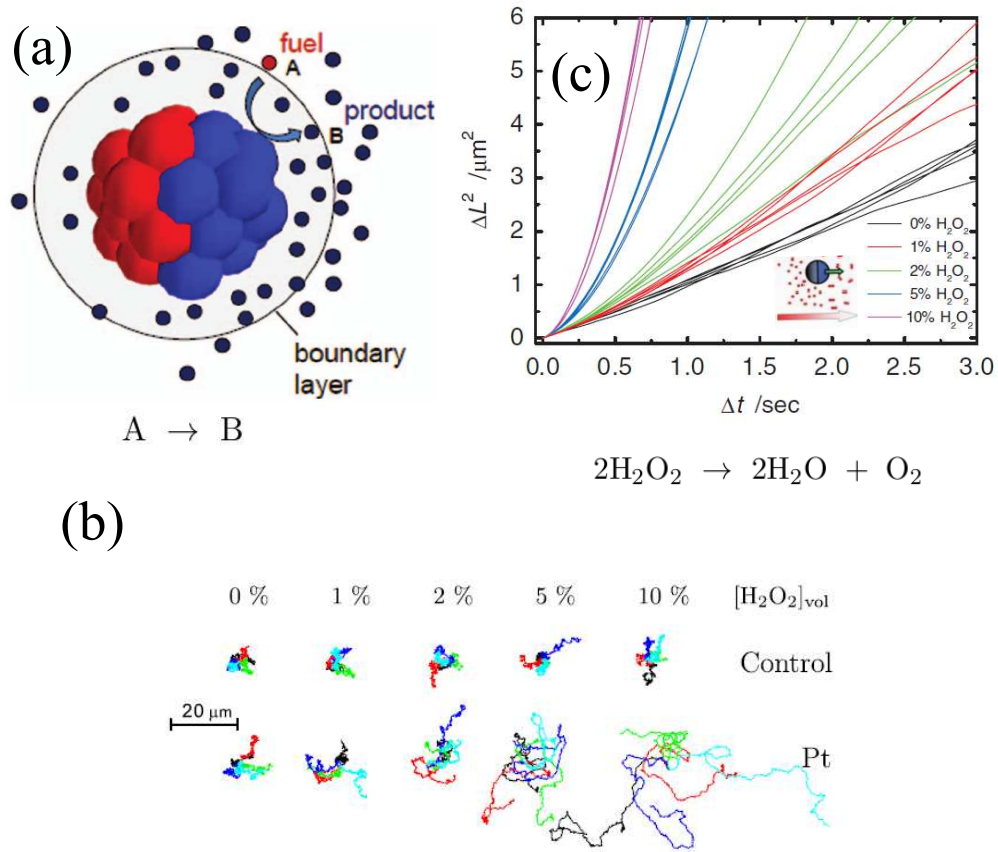
FIGURE 2.2: Illustration and an example of self-diffusiophoresis [26]. (a) A Janus motor composed of catalytic (blue) and noncatalytic (red) spheres. The figure indicates the chemical reaction A $\rightarrow$ B that converts fuel A to product B and shows the inhomogeneous distribution of B molecules around the JPs. The boundary layer around the JP within which the intermolecular forces act is also shown. (b) Trajectories over 25 seconds for 5 particles of the non-coated and platinum-coated particles in solution of hydrogen peroxide with varying concentrations. (c) MSD as a function of time corresponding to different hydrogen peroxide concentrations.

The feasibility of the self-diffusiophoresis mechanism for active swimmers was first proposed by the theoretical study of Howse *et al.* [139] in 2005. They demonstrate that a spherical particle can be synthesized with an asymmetric distributed surface of a catalyst, and this catalyst is able to be decomposed with the help of the solute molecules, illustrated in Fig. 2.2(a). Later in 2007, they realize the scheme and experimentally verified their proposal of self-diffusiophoretic propulsion mechanism by synthesizing the two-faced particle. It is called "Janus particle" (JP) after the name of two-faced

Greek god [26].

Described by authors in Ref. [26], they synthesize a JP by first preparing the polystyrene spherical beads with the diameter as 1.62 μm in a slightly deviation, and then coating one side of the spherical beads with a thin layer of platinum, while leaving the rest half as the polystyrene without conductivity. The artificial particle can be self-propelled when it is immersed in the solution of H_2O_2, with the maximum of the self-propulsion velocity as 3 μm $\cdot$ s^{-1}. The reason that they choose platinum is that the platinum can play a role as catalyzer of the reduction of hydrogen peroxide as follows:

$$2H_2O_2 \rightarrow 2H_2O + O_2.$$
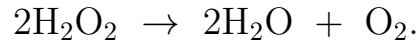
Here hydrogen peroxide plays a role as the fuel and this reaction produces more product molecules than consumed fuel molecules. With particle tracking method, Howse *et al.* manage to fully characterize the motion of the JPs by 2D trajectory and timing [time, $x(\mu m)$, $y(\mu m)$]. The authors record the trajectories and investigate the properties of the motion under different hydrogen peroxide concentration levels, as shown in Fig. 2.2.

Particle trajectories are displayed in Fig. 2.2(b), with a Pt-coated bead and a non-coated bead for comparison in various concentration of hydrogen peroxide. Different from the traditional BM of the control beads, the direction motion of JPs are becoming more obviously while the concentration of hydrogen peroxide is increasing. The MSD as a function of elapsed time for JPs are shown in Fig. 2.2(c), which is in average of 3000 trajectories under various concentration of fuel respectively. It can be indicated from the curve of 0%H_2O_2, ΔL^2 is linear to Δt, the passive BM is undergoing. With the increasing of

the concentration of hydrogen peroxide, JPs are driven by osmotic pressure gradient, which is generated by asymmetrically distributed chemical reaction. As a result, there are parabolic components appearing in these mean-squared displacement (MSD) curves.

Note that in this issue the self-propelled motion is functioned by the rotational diffusion, which leads to a coupling of the rotational and translational motion. Thus the theoretical analysis has been carried out on the dynamics of JPs under the scheme of 2D BM coupled with free rotational diffusion mode [26]. With the self-propulsion velocity denoted as v_0 and Brownian diffusion coefficient as D_0, the 2D MSD is obtained as

$$\Delta L^2 \;=\; 4D_0\Delta t \;+\; \frac{v_0^2\tau_\theta^2}{2}[\frac{2\Delta t}{\tau_\theta} \;+\; e^{-2\Delta t/\tau_\theta} \;-\; 1]. \qquad (2.2)$$

In Eq. 2.2, τ_θ represents the average timescale over which the trajectory direction is maintained with $\tau_\theta = 2/D_\theta$. The authors show that on the short times scale $t \ll \tau_\theta$, the particles are dominated by a self-propelled movement. The velocity of this directed movement follows Michaelis-Menten kinetics as a function of the concentration of H_2O_2. In the longer time scale $t \gg \tau_\theta$, JP's motion returns to a Brownian random walk with an enhanced diffusion coefficient $D_{\text{eff}} \;=\; D_0 \;+\; v_0^2\tau_\theta/4$. The main reason for this distinction is that the directed motion will be finally interfered by fluctuated orientation given the particle running for a longer time. The authors prove that the experimental data are consistent with the predictions of theoretical analysis. These results can be contributed to provide strategies for designing artificial systems in a pioneering stage.

Besides this work by Howse *et al.*, the methods of producing artificial microswimmers benefitted from self-diffusiophoresis mechanism

are developed also by some other groups [140–142]. It is remarkable that Volpe *et al.* propose a novel species of artificial active particles, which are self-propelled by the local asymmetric demixing of a critical liquid mixture upon illumination [125]. This propulsion force can be tracked back to diffusiophoresis when the JP is under the control of local concentration gradient of the solvent. It is found that the self-propulsion velocity of JPs can be efficiently tuned by illumination, which is emphasized to be an advantage.

2.2.4 Model of self-propelled motion in the bulk

A model of self-propelled motion is introduced in the pioneering work by Howse *et al.* [26], the MSD shows the non-Gaussian behavior of self-propelled particles, which is calculated by modeling the motion of the particle as 2D BM coupled with rotational diffusion. As a more comprehensive study in by Hagen *et al.* in Ref. [143] analytically studies the overdamped dynamics of a self-propelled particle by solving the Langevin equation. By calculating the first four moments of probability density for displacements as a function of time, the cases of spherical particle as well as the anisotropic ellipsoidal particle are well discussed respectively in bulk or confined to one or two dimensions. It is reported that the significant non-Gaussian behavior of the active movement can be characterized by non-vanishing kurtosis.

Confined within the scheme of this thesis, we only focus on the 2D motion of spherical particle with one degree of rotational freedom

which is discussed in the work by Hagen *et al.* [143]. The over-damped Langevin dynamics can be given by

$$\frac{d\vec{r}}{dt} = \beta \, D_0 \, [F\vec{u} - \nabla U + \vec{f}\,], \qquad (2.3)$$

$$\frac{d\vec{u}}{dt} = \beta \, D_\theta \vec{g} \times \vec{u}. \qquad (2.4)$$

The denotions appearing in Eqs. 2.3-2.4 are given as follows:

- $\vec{r}(t)$: coordinates of 2D motion;

- $F\vec{u}$: the self-propulsional force;

- θ: the angle between $\vec{e}_\mathrm{x}$ and $\vec{u} = (\cos\theta, \sin\theta)$;

- D_0: translational short-time diffusion constant;

- D_θ: rotational short-time diffusion constant;

- $\vec{f}(t)$: Gaussian white noise as thermal force characterized by

$$\langle f_i \rangle = 0, \ \langle f_i(t)f_j(t') \rangle = 2\delta_{i,j}\delta(t - t')/(\beta^2 D_0); \qquad (2.5)$$

- $\vec{g}(t)$: Gaussian white noise as random torque characterized by

$$\langle g_i \rangle = 0, \ \langle g_i(t)g_j(t') \rangle = 2\delta_{i,j}\delta(t - t')/(\beta^2 D_\theta); \qquad (2.6)$$

 The indexes i, j applied above are the coordinates x, y and $\langle \cdot \rangle$ denotes the ensemble average.

- $U(\vec{r})$: external potential;

- β: inverse of effective thermal energy $(k_\mathrm{B}T)^{-1}$.

Given the simplest case with $U \equiv 0$, Eq. 2.3 can be written explicitly as

$$\frac{dx}{dt} = \beta D_0 F \cos\theta + \beta D_0 \, f_\mathrm{x}, \qquad (2.7)$$

$$\frac{dy}{dt} = \beta D_0 F \sin\theta + \beta D_0 f_{\mathrm{y}}, \tag{2.8}$$

Under the constrict of 2D motion and one degree of rotation, the general vector Eq. 2.4 can be simplified as

$$\frac{d\theta}{dt} = \beta D_\theta \vec{g} \cdot \vec{e}_{\mathrm{z}}. \tag{2.9}$$

Thus, the general equations Eqs. 2.3-2.4 for the motion of JPs are simplified by considering Eqs. 2.7-2.9. For spherical particles diffusing through a liquid with low Reynolds number, the translational diffusion constant satisfies $D_0 = k_{\mathrm{B}}T/6\pi\eta R$ according to the Stokes-Einstein equation, where η represents the dynamic viscosity and R the radius of the particle. D_θ and D_0 fulfill the relation

$$\frac{D_0}{D_\theta} = \frac{4}{3} R^2. \tag{2.10}$$

Since Eq. 2.4 on θ is the linear combination of Gaussian variables, the probability density of θ is considered to be Gaussian as well, referred to Wick's theorem [144]. The authors prove that

$$P(\theta, t) = \frac{1}{\sqrt{4\pi D_\theta}} \exp\left[-\frac{(\theta - \theta_0)^2}{4D_\theta t}\right], \tag{2.11}$$

in which θ_0 is the initial angle. With the help of Eq. 2.11, the analytical results for the first and second moments of probability density can be achieved by integrating the averaged equations Eqs. 2.7-2.8 over time. The authors first obtain the mean position and MSD for 1D diffusion, and then extend the results to 2D diffusion with MSD as [143]

$$\langle (\vec{r}(t) - \vec{r}_0)^2 \rangle = \frac{16}{3} R^2 D_\theta t + 2(\frac{4}{3}\beta F R^2)^2 [D_\theta t - 1 + e^{-D_\theta t}]. \tag{2.12}$$

Introducing v_0 into Eq. 2.12 by the following replacement

$$v_0 = \beta D_0 F, \tag{2.13}$$

and combining the relation in Eq. 2.10, it turns out exactly the same expression of MSD in Eq. 2.2. This 2D model and the corresponding results are widely employed in the further theoretical and experimental studies of active movement as an important and basic picture.

2.3   Circular active motion

In the previous section, the active swimmers are assumed to averagely move along the self-propelled force. Under this scheme, the JPs always are directed in a straight line, which can only be fluctuated by rotational randomness [26]. However, there is large chance that the internal propulsion is not identical with the orientation of the active swimmer [145]. When a microswimmer utilizes the propulsional force from its surroundings, a torque can be resulted from the misalignment of self-propulsion which leads to chirality [146, 147]. Suppose there was no thermal noise, this kind of active swimmer would intend to move in a circle induced by an intrinsic torque, which is named "circle swimmer" or "chiral swimmer" [145, 148].

In nature, there are several examples of chiral swimmers, such as *E. coli* bacteria [149] and spermatozoa [150, 151] swimming in a circular trajectory, when they are constricted in two dimensions. Recently, the chiral movement was achieved artificially [19, 117, 152]. Current experiments prove evidence that a torque can be due to the presence of geometrical asymmetries in the particle fabrication [126, 153, 154].

The torque can also be resulted externally from laser irradiation [142], hydrodynamic fields [155], or the Lorentz force applied by a magnetic field on a charged active particle in the finite damping regime [156]. Here in this section, we focus on the introduction of shape-asymmetry induced chiral motion [126, 157].

2.3.1   Example: Active swimmer with asymmetric shape

It has been mentioned in Sec. 2.2.3, that a type of JP is experimentally realized under the assistant of illumination, with local asymmetric demixing of a critical liquid mixture as its reason for self-propulsion [125]. Recently, Kümmel *et al.* manage to realize a artificial chiral swimmer experimentally [126] with the same principle of self-diffusiophoresis generated, but with asymmetric L-shaped active swimmer instead of spherical active swimmer.

In their experiment, asymmetric L-shaped swimmers are first fabricated from photoresist SU-8 by photolithography, with the length of short arm of 6 μm and that of the long arm of 9 μm. With this inactive micro-object prepared, it is coated on the front side of its short arm with 20 nm thick Au layer by thermal evaporation. Then these active L-shaped particles are immersed in a mixture of water and 2,6-*lutidine* below the critical temperature $T_{\rm c}$ = 307 K, and the base temperature of the active L-shape particles is controlled below $T_{\rm c}$. The inset of Fig. 2.3(a) shows microscope images of the Au coated L-shaped swimmer. For their needs of investigations on two dimensional motion, a sealed sample sell with 7 μm height is applied to contain the suspension system. In this way, the particle is confined to move in 2D, and cannot turn upside down to switch between the two modes denoted as $L+$ and $L-$ shown in Fig. 2.3(a,b).

When the sample particle is homogeneously illuminated by light with $\lambda = 532\ nm$ at intensities $I \sim 1\mu W/\mu m^2$, the Au layer is slightly heated exceeding the critical temperature point T_c and the particles motion strongly depends on the incident light intensity. It is because the heated part of the particle induces a local demixing of the solvent close to it, and this results in a self-phoretic induced movement as described before.

The probability density functions of orientation under illumination is shown in Fig. 2.3(d), compared with uniformed distribution of the passive movement in Fig. 2.3(c). From 2.3(c), it can be found that the rotational and translational motion are independent for passive BM. While triggered by the illumination, the propulsion force is acting on the asymmetric active particle, which leads to the coupling of the rotational and translational motion. Evidence is provided in 2.3(d), for a peak appears in the curve of probability density function of orientation. It is also pointed out that, $L-$-shaped particle behaves different from $L+$-shape particle in the probability density function of orientation, with the peak shifting to be negative for a counter-clockwisely circular motion.

The authors propose two coupled Langevin equations for the translational and rotational motion of the particles, subjected to an intrinsic propulsional force and a velocity-dependent torque induced by the shape-asymmetry of the particle. This model predicts a circular motion, which is in a good agreement with experiments.
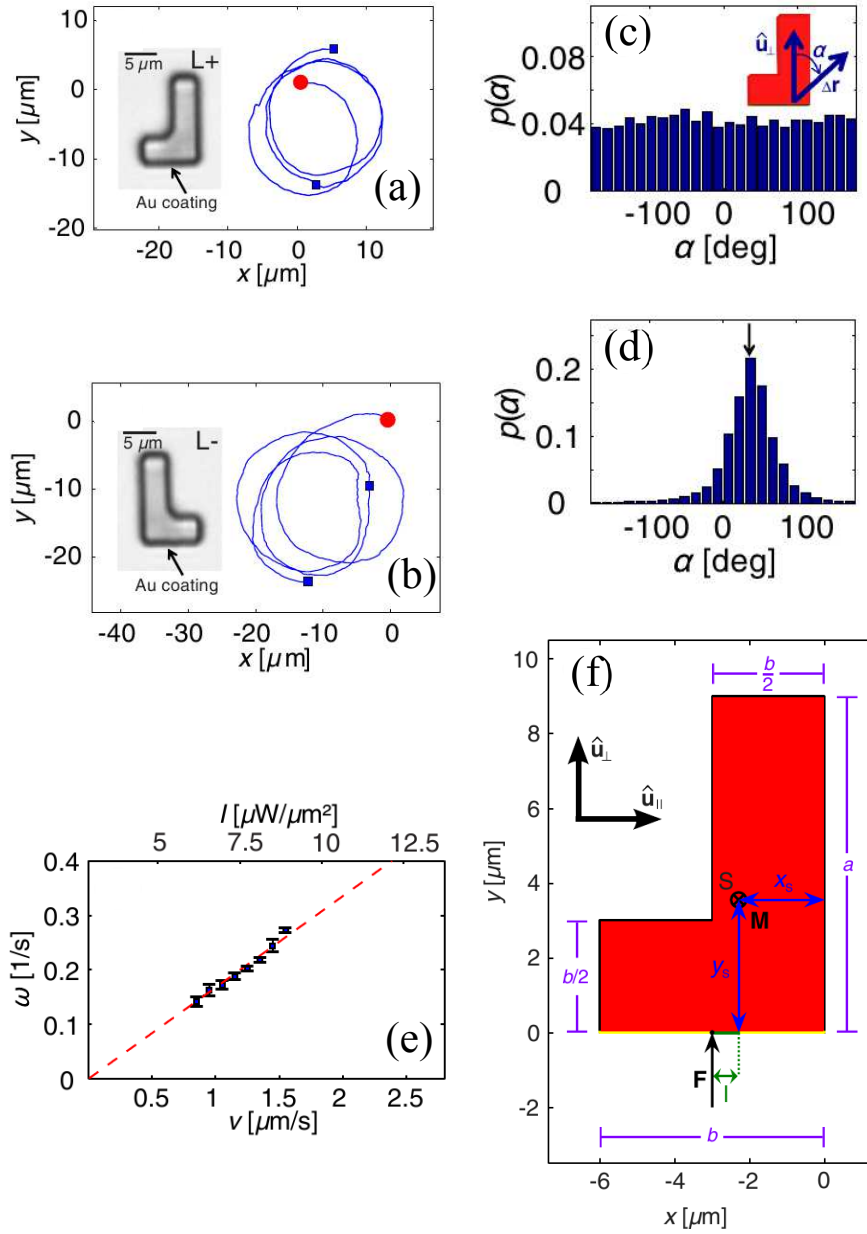
FIGURE 2.3: Illustrations and observations on *L*-shaped swimmers, adopted from [126]. (a),(b) Trajectories of *L*+ and *L*− swimmer respectively, under an illumination with $I = 7.5\ \mu W/\mu m^2$. (red bullets: the initial positions; blue little squares: positions after 1 minute) (c),(d) For *L*+-shape particle, the probability density function of the angle between normal direction of Au-coating side and the direction of displacement, in time intervals of 12 seconds under the illumination intensity (c) $I = 0\ \mu W/\mu m^2$ and (d) $I = 5\ \mu W/\mu m^2$. (e) Angular velocity of the circular motion of an *L*+-shaped swimmer as function of the velocity and the illumination intensity $I \propto v$, with linear fitting by the dashed line. (f) Geometrical sketch of an ideal *L*+-shaped swimmer. A torque *M* is induced by the internal force *F*, which is depending on the lever arm *l*.

2.3.2   Model of chiral motion in the bulk

To understand the observed behavior of the motion of chiral swim-
mers, the bulk dynamics described by Langevin equations is com-
monly applied in recent paper for analytical and numerical studies
[126, 145, 157]. Here we introduce the Langevin dynamics proposed
in Ref. [157], which is employed as the dynamic equations for our
simulation results shown later.

In Ref. [157], the authors investigate the self-assembled doublets of
JPs which are self-propelled individually, illustrated in Fig. 2.4. In
short, following the method described in Ref. [26] by Howse *et al.*,
the individual platinum JPs are prepared and suspended in H_2O_2
solution. After storage for several days, the formation of doublets
and larger agglomerated are observed. This Janus doublet is under
translational propulsion as well as rotational propulsion while subject
to Brownian fluctuations. It can play linear translation, spiraling
and spinning motion as well according to the authors' observation.
The intrinsic reason is due to the anisotropic configuration of the
doublet particles, which is similar to L-shaped swimmers realized by
Kümmel *et al.* [126].

For simplicity, the authors treat the swimmers as isotropic objects,
ignoring the complexity of anisotropy in the diffusion resulted from
the shape. Experimental observation shows that the doublets are
likely to swim close to the substrate and display 2D motion parallel
to it. Thus, the system is considered here not as the 2D projection
of 3D motion, but as an intrinsically two dimensional system, with
(x, y) as its position coordinates and θ as its orientation illustrated in
Fig. 2.4(g). Different from Eqs. 2.4-2.3, the Langevin equations for
free Janus doublets under overdamped limit are written as follows
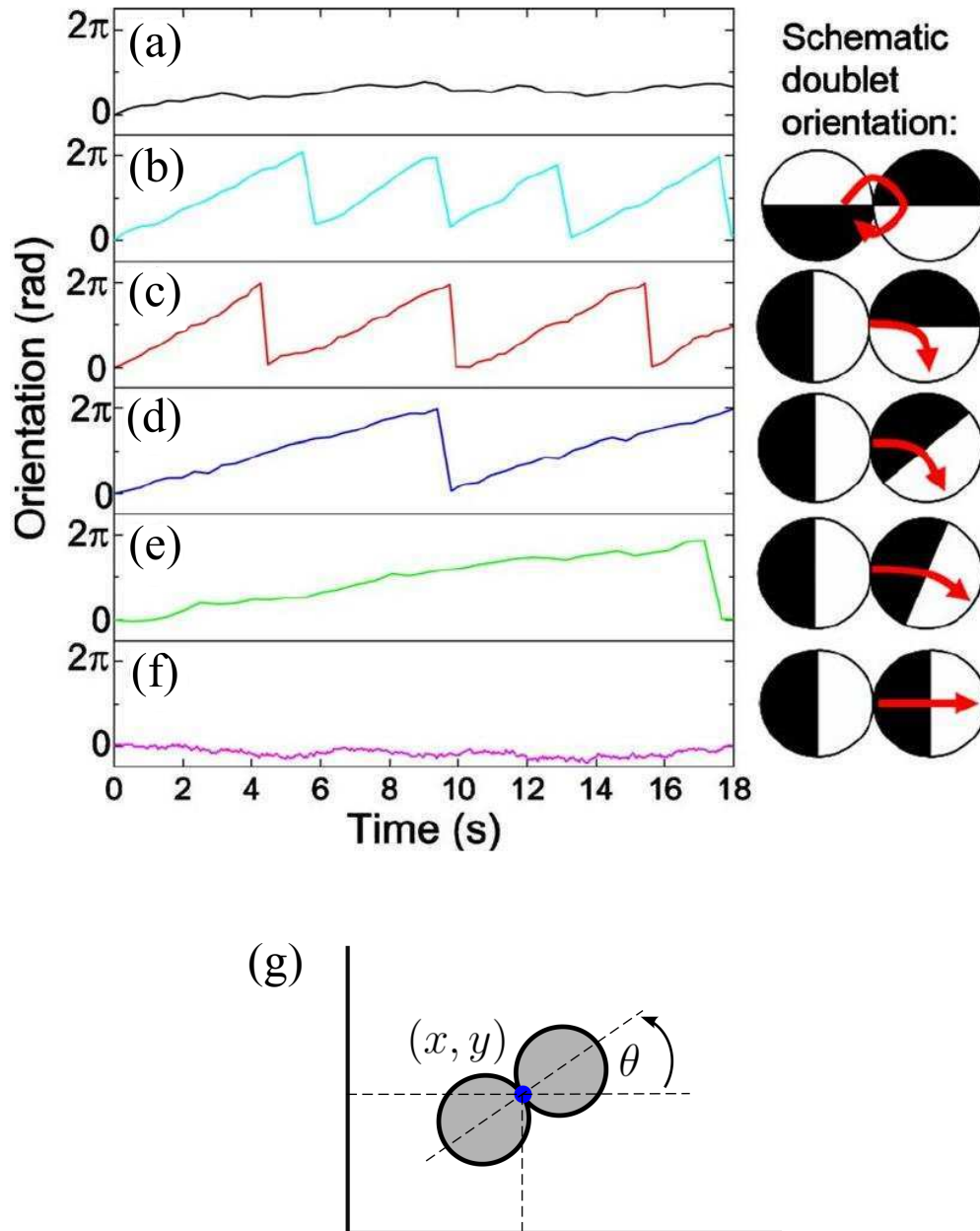
FIGURE 2.4: Illustrations of Janus doublets and plots of orientation versus time, adopted from [157]. (left) (a)Janus doublets in (b)-(f) Orientation of doublets versus time plots, under the increasing concentration of H_2O_2 (right) Illustration of Janus doublets with different configurations correspondingly to left plots. (g) Illustration of 2D translational and one degree of rotational freedom for Langevin dynamics.

with the external torque:

$$\frac{dx(t)}{dt} = v_0 \cos\theta + \xi_1, \tag{2.14}$$

$$\frac{dy(t)}{dt} = v_0 \sin\theta + \xi_2, \tag{2.15}$$

$$\frac{d\theta(t)}{dt} = \Omega + \zeta, \tag{2.16}$$

in which v_0 denotes self-propulsional velocity and Ω the corresponding torque. $\xi_{1,2}$ and ζ are Gaussian white noise terms which satisfy

$$\langle \xi_i \rangle = 0, \ \langle \xi_i(t)\xi_j(t') \rangle = 2D_0\delta_{i,j}\delta(t - t'), \quad \text{for } i, j = 1, 2 \tag{2.17}$$

$$\langle \zeta \rangle = 0, \ \langle \zeta(t)\zeta(t') \rangle = 2D_\theta\delta(t - t'), \tag{2.18}$$

in which D_0 and D_θ representing translational and rotational coefficient. The authors report that trajectories obtained by simulating Eqs. 2.14-2.16 show a good agreement with the experimental observations. They analyze the orientational MSD based on this Langevin approach as

$$\Delta \ \theta^2(t) \equiv \langle [\theta(t) - \theta(0)]^2 \rangle = \Omega^2 t^2 + 2D_\theta t. \tag{2.19}$$

The velocity auto-correlation function can be calculated with the help of Eq. 2.19 as

$$\langle \vec{v}(t) \cdot \vec{v}(0) \rangle = 4D_0\delta t + v_0 \cos(\Omega t) \ e^{-D_\theta t}. \tag{2.20}$$

Thus MSD can be obtained by the following integration

$$\Delta L^2(t) \equiv \langle [\vec{r}(t) - \vec{r}(0)]^2 \rangle = \int_0^t dt_1 \int_0^t dt_2 \ \langle \vec{v}(t_1) \cdot \vec{v}(t_2) \rangle, \tag{2.21}$$

which is finally obtained as

$$\Delta L^2(t) = 4D_0 t + \frac{2v_0^2 D_\theta t}{D_\theta^2 + \Omega^2} + \frac{2v_0^2(\Omega^2 - D_\theta)}{(D_\theta^2 + \Omega^2)^2}$$
$$+ \frac{2v_0^2 e^{-D_\theta t}}{(D_\theta^2 + \Omega^2)^2} [(D_\theta^2 - \Omega^2)\cos(\Omega t) - 2\Omega D_\theta \sin(\Omega t)]. \quad (2.22)$$

For very small time scale $t \ll \max\{2/D_\theta, 1/\Omega\}$, MSD is simplified as

$$\Delta L^2(t) = 4D_0 t + v_0^2 t^2, \quad (2.23)$$

which is similar to a single self-propelled particle. The authors then consider the long time behavior with $t \gg \max\{1/\Omega, 2/D_\theta\}$, and the effective diffusivity is

$$D_{\text{eff}} \equiv \lim_{t \to \infty} \frac{\Delta x^2(t)}{2t} = D_0 + \frac{v_0^2 D_\theta}{2(D_\theta^2 + \Omega^2)}. \quad (2.24)$$

2.4 Summary

In this chapter, we overview the development of the active microswimmers, and introduce self-electrophoresis and self-diffusiophoresis as the mechanisms for self-propulsion by a typical experiment for each. Theoretical model of the active particles using Langevin equations are presented referred to the previous studies, for non-chiral and chiral JPs in 2D respectively.

Chapter 3

Brownian transport in corrugated channels

In this chapter, we briefly review the previous literature on traditional Brownian transport of small particles in channels. We start from the motivations, then introduce the channel model with diffusion equations and boundary conditions. We discuss the exact solution of 1D system diffusing on the energy landscape, and after that the approximate solutions are obtained for 2D by Fick-Jacobs (FJ) approach, reducing the confined BM to diffusing on effective 1D potential landscape.

3.1 Motivations

Transport and diffusion of particles through microscopic structure is ubiquitous and of increasing interest in the last two decades [49, 95, 158]. The applications in chemistry and biology are numerous in recent years: the transport and catalysis in synthesized zeolites [52], micro-channels [57, 159, 160], molecular separator [161], or in solid-state nanopores as single-molecule sensors for the detection and

sequential analysis of DNA [85, 162–164]. In many respects, observing these interesting diffusion and transport phenomena requires a detailed understanding of diffusion processes occurring in confined geometries [165–167].

Note that boundaries cause the limitation of the volume of the phase space of diffusing particles, which can lead to the striking entropic effect [54]. As the examples of the diffusion determined by entropic barriers, translocation of charged particles through artificial ion pumps [56, 57, 75, 88, 168, 169] or biological channels serve as a general situation. As an addition, it is proved by the recent observation on the interact between diffusion over the entropic barriers and the time-periodic driven, that the absolute negative mobility is found [170, 171]. It is necessary to mention that, besides the small particles, the entropic forces can also play an important role in the dynamics of extended chains diffusing in a periodic channel. As an interesting example in applications, the translocation of a long polymer molecule moving through a pore with the width similar to the radius of the polymer circulation [172–175].

3.2   Model of channel diffusion in 3D

First we start from the typical transport process though confined geometries illustrated in Ref. [95]. We consider the diffusion of small spherical particles in channels along the x-axis direction. Assume that

- The radius of the particle is extremely small, almost point-like;

- The boundary of the channel consists of smooth and rigid walls;

- The boundary function are considered to be symmetric with 2D reflection on the x-axis for 2D channel, or invariant under rotation about x-axis for 3D channel.

As the boundary is assumed to be rigid, we disregard the situation of particle-adsorption by the wall. For simplicity, we do not consider the rotation of the particles. Thus, the boundary only constrict the position of particles inside the channel without the particle-wall interactive force specified. According to the assumptions above, since the particles are rather small compared with the width of bottle-neck of the channel, the particles are not stuck at a certain region but diffuse along the channel.

3.2.1 Equations for diffusion in the bulk

First we investigate the bulk dynamics of the small particles with radius R swimming in a fluid. Since the particle does not modify the surrounding fluid, that means the dynamics of the fluid is in laminar flow regime. We denote the position of particle as $\vec{r} \equiv (x, y, z)$ and the instantaneous velocity of the particle $\dot{\vec{r}}$. We assume the density of the particle is rather low, so that the hydrodynamic interactions between the particles can be neglected [176, 177]. Thus the particle is subjected to frictional force $\vec{F}_{\text{st}}$, thermal force $\vec{F}_{\text{th}}$ and inertial force $m\ddot{\vec{r}}$ [95]. We denote the friction coefficient as γ and the instantaneous velocity of the fluid around the particle is represented by $\vec{v}(\vec{r}, t)$. The frictional force thus follows the Stokes law [178–180]

$$\vec{F}_{\text{st}} = -\gamma[\dot{\vec{r}} - \vec{v}(\vec{r}, t)], \tag{3.1}$$

in which the friction coefficient is given by

$$\gamma = 6\pi\eta R, \tag{3.2}$$

with η being as the dynamic viscosity of fluid.

Here we consider the simplest situation with the fluid system in homogeneous temperature T. Immersed in the fluid with low Reynolds number, the particle is subjected to a random thermal force $\vec{F}_{\text{th}}$ written as [95]

$$\vec{F}_{\text{th}} = \sqrt{2\gamma k_{\text{B}}T}\vec{\xi}(t), \tag{3.3}$$

in which k_{B} is Boltzmann constant. $\vec{\xi}(t)$ in Eq. 3.3 is the Gaussian white noise with three components in x, y and $z-$directions with zero mean as

$$\langle \vec{\xi}(t) \rangle = 0, \tag{3.4}$$

and according to the fluctuation-dissipation theorem [181]

$$\langle \xi_{\text{i}}(t)\xi_{\text{j}}(t') \rangle = \delta_{\text{i,j}}\delta(t - t'), \tag{3.5}$$

with $i, j = x, y, z$.

Given the mass of the particle m, combining the inertia term, frictional force and thermal force, the dynamics of the particle is described by Langevin equation

$$m\ddot{\vec{r}} = \vec{F} - \gamma[\dot{\vec{r}} - \vec{v}(\vec{r}, t)] + \sqrt{2\gamma k_{\text{B}}T}\vec{\xi}(t). \tag{3.6}$$

In Eq. 3.6, an external force denoted by $\vec{F}$ is considered to act on the particle along the direction of channel axis in x-direction $\vec{F} = F\vec{e}_{\text{x}}$. For the small particle moving with a velocity of the order of $1\text{cm} \cdot \text{s}^{-1}$ in the fluid with low Reynold number, the inertia term

$m\ddot{\vec{r}}$ turns out to be small enough to be neglected compared to frictional and thermal force term [95, 110]. Given that the fluid velocity changing slowly with the spectral frequencies in the order less than 100Hz, we can only consider the overdamped limit or Smoluchowski approximation [42]. The Langevin equation in overdamped limit is obtained by simplifying Eq. 3.6

$$\dot{\vec{r}} \;=\; \vec{v}(\vec{r},t) \;+\; \frac{\vec{F}}{\gamma} \;+\; \sqrt{\frac{2k_{\mathrm{B}}T}{\gamma}}\vec{\xi}(t). \tag{3.7}$$

With the denotation $P(\vec{r},t)$ as the probability density of a particle at the position $\vec{r}$ at the moment t, the corresponding Fokker-Planck equation is written as [182]

$$\frac{\partial P(\vec{r},t)}{\partial t} \;=\; -\nabla \cdot \vec{J}(\vec{r},t), \tag{3.8}$$

in which $\vec{J}(\vec{r},t)$ is defined as the probability current density

$$\vec{J}(\vec{r},t) \;=\; [\vec{v}(\vec{r},t) \;+\; \frac{\vec{F}}{\gamma}]P(\vec{r},t) \;-\; \frac{k_{\mathrm{B}}T}{\gamma}\nabla P(\vec{r},t). \tag{3.9}$$

Since Eq. 3.8 describes bulk dynamics of Brownian particles under overdamped limit, the proper boundary conditions should be considered for the investigation of the confined diffusion.

3.2.2 Boundary conditions

Since the channel is a rigid wall defined as the geometrical constrict of the particle diffusion, the normal component of the probability current at the boundary should vanish to prevent the leaking of the

particle. The reflective boundary condition suffices a vanishing probability current at the boundaries which is written as [71, 95]

$$\vec{n}(\vec{r}) \cdot \vec{J}(\vec{r}, t) \;=\; 0 \quad \vec{r} \in \text{wall}, \tag{3.10}$$

in which $\vec{n}$ represents the unit vector in the normal direction at the walls. Note that an exact analytical solution to the Fokker-Planck Eq. 3.8 can be hardly obtained for an arbitrary periodic channel, except for a straight channel. In the following sections, we first consider the diffusion of Brownian particle in a periodic potential motivated from 1D transport system in nature. Based on this and combined with the idea of simulating the constrict of the channel by 1D entropic potential, the approximation solution of 2D or 3D channel diffusion equations can be obtained by converting it into a free diffusion on the effective 1D potential, which is the FJ approach introduced later.

3.3 Exact solution of transport in 1D periodic potentials

3.3.1 Free diffusion under a constant force

The diffusion of a Brownian particle in a periodical potential are highly motivated from the pure energetic nano-systems [36, 182]. Given Brownian particles diffuse in the absence of the boundaries, the dynamics of the particle in na asymptotically long time satisfies the Einstein relation with the diffusion constant as [39, 40]

$$D_0 \;=\; \frac{k_{\mathrm{B}} T}{\gamma}. \tag{3.11}$$

The dynamics of the particle is considered under the overdamped limit, subjected to an external force, friction force and thermal force. The external force is assigned as a constant bias only applied along the x-direction $\vec{F} = F\vec{e}_x$ in x-direction. The frictional force is $-\gamma\dot{x}$ with the friction constant γ, and thermal force is $\sqrt{2\gamma k_B T}\xi(t)$ under the environment temperature T. For modeling the thermal fluctuations, ξ is Gaussian white noise with $\langle\xi(t)\rangle = 0$ and $\langle\xi(t)\xi(t')\rangle = \delta(t-t')$. The dynamics of the BM under a constant bias in the overdamped limit in 1D is described by corresponding Langevin equation [71, 110]

$$\gamma\dot{x} = F + \sqrt{2\gamma k_B T}\xi(t). \qquad (3.12)$$

It is reported in Ref. [71], that the particle current $\langle\dot{x}\rangle$ under the steady state is proportional to F for any $k_B T$ as long as F is constant. By taking the transformation $x(t) \rightarrow x(t) - \frac{F}{\gamma}t$, the diffusion coefficient D_0 is proved to be independent of the external force F.

It is worth to note that it is similar process for a Brownian particle diffusing in a flat channel, for the reason that there is no obstacles in the direction for particle transport. In the following subsection, we discuss on the Brownian particles in non-flat channels, which can play impacts on the particle transport behaviors. We consider the solvable condition of the Brownian transport in periodic potential.

3.3.2 Brownian transport in 1D periodic potentials

With the periodic potential in 1D with period L denoted as

$$V(x + L) = V(x), \qquad (3.13)$$

the Langevin dynamics of the diffusion of a particle in the potential $V(x)$ and constant bias perviously considered is written as

$$\gamma \dot{x} = -V'(x) + F + \sqrt{2\gamma k_{\mathrm{B}} T} \xi(t). \tag{3.14}$$

It is elaborated [95, 183] that for the situation $F < \max\{V'(x)\}$, the particle is spatially limited around the trough of the potential $V(x)$ for most of the time. Differently, the particle subjected to F can always deterministically overcome the potential barrier if $F > \max\{V'(x)\}$, and the particle is driven in the direction of F with the mean velocity approaching to the constant value F/γ. With $P(x,t)$ denoting 1D probability distribution function, the corresponding Fokker-Planck equation in 1D for such system reads [183–186]

$$\frac{\partial P(x,t)}{\partial t} = \frac{\partial}{\partial x} \left(\frac{U'(x)}{\gamma} + D_0 \frac{\partial}{\partial x} \right) P, \tag{3.15}$$

in which $U(x) \equiv V(x) - Ft$. Denote $\beta = k_{\mathrm{B}} T^{-1}$, Eq. 3.15 can be written as

$$\frac{\partial P(x,t)}{\partial t} = D_0 \frac{\partial}{\partial x} \left(\beta U'(x) + \frac{\partial}{\partial x} \right) P \tag{3.16}$$

To characterize the transport of the system, the average current $\langle \dot{x} \rangle$ and normal diffusion coefficient $D(F)$ are introduced as

$$\dot{x} \equiv \lim_{t \to \infty} \frac{\langle x(t) \rangle}{t}, \tag{3.17}$$

$$D(F) \equiv \lim_{t \to \infty} \frac{\langle x(t)^2 \rangle - \langle x(t) \rangle^2}{2t}. \tag{3.18}$$

These two characterization quantities can be calculated by the mean-first-passage-time approach[183, 185–188]. The explicit expression of

the average can be obtained by some algebraic derivations [182, 185]

$$\dot{x} \;=\; D_0 L \; \frac{1 \,-\, e^{-\beta F L}}{\int_0^L \, I_+(x) dx},$$

(3.19)

and the normal diffusion coefficient reads [183, 186]

$$D(F) \;=\; D_0 L^2 \; \frac{\int_0^L I_+^2(x) I_-(x) dx}{\left[\int_0^L I_+(x) dx\right]^3},$$

(3.20)

in which the integral functions $I_\pm(x)$ are given as

$$I_\pm \;=\; \int_0^L e^{(\pm V(x) \mp V(x \mp y) \,-\, y\beta F)} dy.$$

(3.21)

It is proved that the analytical expression of average current and normal diffusion constant can be generalized to the anomalous sub-diffusion by substituting the free diffusion constant D_0 by the fractional diffusion constant involved in the anomalous diffusion equation [189, 190].

3.4 Fick-Jacobs approximation

Based on the discussions of transport in 1D periodic potential in last section, we consider 2D or 3D diffusion problem in channels described in Sec. 3.2. Despite that the exact solution for such problems can not be obtained as mentioned, the methods for approximated solution can be deduced by reducing the dimensionality of the initial channel diffusion Eqs. 3.8.

The idea for FJ approximation approach is elaborated intensively in the book by M. H. Jacobs [63] and later re-interpreted by R. Zwanzig [62], that the periodically corrugated channel can be simulated by a

1D periodic potential along the transport direction. It is based on the assumption that the Brownian particles reach the equilibrium infinitely fast in the transverse directions of the transport direction. Give the distribution of the particles in the cross sections of the channel is supposed to be uniform, the probability density function in 2D (or 3D) position $P(\vec{r}, t)$ can be reduced to $P(x, t)$ by integration over the transverse coordinates y (and z), leaving x the coordinate of the transport direction. The FJ approximation approach gives the corresponding 1D diffusion equation, which treats the geometric constrains and the involved bottlenecks as the entropic barriers.

In order to give a concise derivation of FJ equation, we consider a 2D potential in general version $U(x, y)$. Similar to Eq. 3.16, with $P(x, y, t)$ denoting the probability density of finding the particle in 2D postion (x, y) at time t, the corresponding Smoluchowski equation in a 2D potential $U(x, y)$ is written as [62]

$$
\begin{aligned}
\frac{\partial P(x, y, t)}{\partial t} \;=\;& D_0 \, \frac{\partial}{\partial x} e^{-\beta U(x,y)} \, \frac{\partial}{\partial x} e^{\beta U(x,y)} \; P(x, y, t) \\
& + \; D_0 \, \frac{\partial}{\partial y} e^{-\beta U(x,y)} \, \frac{\partial}{\partial y} e^{\beta U(x,y)} \; P(x, y, t).
\end{aligned} \quad (3.22)
$$

Introduce the local probability density in $x-$direction denoted as $G(x, t)$, which is defined as the integral over y of $P(x, y, t)$:

$$
G(x, t) \;\equiv\; \int \, dy \; P(x, y, t). \quad (3.23)
$$

With the purpose to derive the diffusion equation of $G(x, t)$ equivalent to Eq. 3.22, integrate Eq. 3.22 over y, we obtain

$$
\begin{aligned}
\frac{\partial G(x, t)}{\partial t} \;=\;& D_0 \int \, dy \, \left[\frac{\partial}{\partial x} e^{-\beta U(x,y)} \, \frac{\partial}{\partial x} e^{\beta U(x,y)} \; P(x, y, t) \right] \\
& + \; D_0 \frac{\partial}{\partial y} e^{-\beta U(x,y)} \, \frac{\partial}{\partial y} e^{\beta U(x,y)} \; G(x, t).
\end{aligned} \quad (3.24)
$$

Since the second term of Eq. 3.25 vanishes for $\frac{\partial}{\partial y}G(x,t) = 0$, Eq. 3.22 is rewritten as

$$\frac{\partial G(x,t)}{\partial t} = D_0 \int dy \left[\frac{\partial}{\partial x} e^{-\beta U(x,y)} \frac{\partial}{\partial x} e^{\beta U(x,y)} P(x,y,t) \right]. \quad (3.25)$$

According to the assumption that the local equilibrium can be extremely rapidly approached in $y-$direction, the conditional probability of a certain transverse coordinate y given the particle is located in a certain x is calculated as

$$\rho(y|x) \equiv \frac{e^{-\beta U(x,y)}}{\int dy \ e^{-\beta U(x,y)}}. \quad (3.26)$$

Here we define a $x-$dependent free energy $A(x)$:

$$e^{-\beta A(x)} \equiv \int dy \ e^{-\beta U(x,y)}. \quad (3.27)$$

The 2D probability density function satisfies the form

$$P(x,y,t) = \rho(y|x)G(x,t). \quad (3.28)$$

Finally, the integrated probability density $G(x,t)$ obeys the 1D Smoluchowski equation

$$\frac{\partial G(x,t)}{\partial t} = D_0 \frac{\partial}{\partial x} e^{-\beta A(x)} \frac{\partial}{\partial x} e^{\beta A(x)} G(x,t), \quad (3.29)$$

which is referred to as a generalized form of FJ equation to diffusion in a 2D channel [62]. For 3D channel diffusion, the FJ equation can be obtained simply by replacing integration over y by double integration over y and z.

In Eq. 3.29, the boundary condition is involved in the potential $U(x,y)$, which represents the constrict effects of the boundary. For

a 2D diffusion confined in a tube with upper(lower) boundary function $w_+(x)(w_-(x))$, the corresponding 2D potential $U(x, y)$ should be written as [62]

$$U(x, y) = \begin{cases} \infty & \text{if } y > w_+(x) \text{ or } y < w_-(x) \text{ ,} \\ 0 & \text{if } w_-(x) < y < w_+(x). \end{cases}$$

Thus the introduced free energy in Eq. 3.27 is calculated as

$$e^{-\beta A(x)} = w_+(x) - w_-(x) = w(x), \qquad (3.30)$$

in which $w(x)$ denotes the width for 2D channel. Insert Eq. 3.30 into Eq. 3.29, the FJ equation is obtained as

$$\frac{\partial G(x, t)}{\partial t} = D_0 \frac{\partial}{\partial x} \left[w(x) \frac{\partial}{\partial x} \frac{G(x, t)}{w(x)} \right]. \qquad (3.31)$$

Here D_0 denotes the solution diffusion coefficient in the bulk and $w(x)$ represents the width for a 2D channel at the position x, which can be also extended as the cross section area of a 3D tube at x. Zwanzig proposed the generalized FJ equation as

$$\frac{\partial G(x, t)}{\partial t} = \frac{\partial}{\partial x} \left[D(x) w(x) \frac{\partial}{\partial x} \frac{G(x, t)}{w(x)} \right], \qquad (3.32)$$

with $D(x)$ is introduced as a position-dependent diffusion coefficient, for extending its validity to more winding confinements [62].

3.5 Summary

In this chapter, we briefly review the previous studies on BM of zero-sized particles in confined channels. We introduce the channel diffusion model with diffusion equations and boundary conditions

in 3D, then discuss the diffusion on the energy landscape with exact solution in 1D. With the idea of simplification of the diffusion equation for higher dimension, we introduce the FJ approach with the approximate solutions obtained in 2D. This approach treats the confined Brownian diffusion in 2D or 3D as diffusion on effective 1D potential landscape. However for the JP in the confinement, the FJ equations are still very difficult to solve analytically. As the result, we focus on the numerical simulation of the confine active BM in the later chapters.

Chapter 4

Model and Simulation Algorithm

In this chapter, we mathematically model the 2D motion of the active particles in the bulk by Langevin equations. Correspondingly, the finite difference equations are implemented for numerical simulation. We verify the algorithm by looking into time evolution profile of MSD. With the confined geometries introduced for the study on active transport, the algorithm for simulating the active BM near the boundary is proposed. Finally, we take an example for simulation showing how active particles are different from passive particles, which can be funneled in a ratchet-like channels.

4.1   Mathematical model: Langevin dynamics

Assume that the active microswimmers are moving in a 2D homogeneous environment. For simplicity, we restrict the discussion of the thesis to the case of point-like active particles [191]. This kind of JP is subject to a continuous push from the suspension fluid, which contributes to the rotating self-propulsion velocity $\vec{v_0}$ with constant modulus v_0 and angular velocity Ω, illustrated in Fig. 4.1(a). Accordingly, the motion of the active particle consists of four different

processes, a random translational and rotational diffusion process, self-propulsion, and a torque in case of a chiral JP. In particular, we consider a spherical particle undergoes active Brownian diffusion with translational diffusion coefficient D_0, and rotational diffusion with rotational diffusion coefficient as D_θ. Here in this thesis, we consider D_0 and D_θ as independent parameters, which is a more general case than Eq. 2.10 describes, for the orientational noise can be produced independently from D_0.
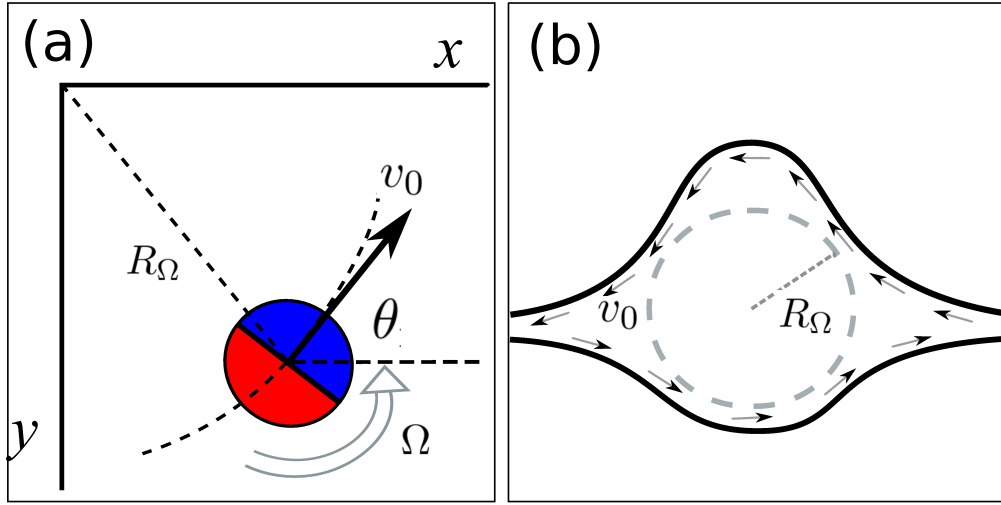
FIGURE 4.1: Illustration of a chiral JP in the bulk and a corrugated channel. (a) A noiseless chiral-JP in the bulk with self-propulsion velocity v_0 and torque frequency $\Omega > 0$, moves in a circle with radius R_Ω, shown in dashed line; (b) A chiral JP moves in a corrugated channel with upside-down asymmetric compartment. The arrows are drawn for the explanatory purpose of the boundary flow of chiral JPs in the steady state.

The dynamics of overdamped JP obeys Langevin equations [145, 157]

$$\dot{x} = v_0\cos\theta + \sqrt{2D_0}\xi_{\mathrm{x}} \tag{4.1}$$

$$\dot{y} = v_0\sin\theta + \sqrt{2D_0}\xi_{\mathrm{y}} \tag{4.2}$$

$$\dot{\theta} = \Omega + \sqrt{2D_\theta}\xi_\theta \tag{4.3}$$

where ξ_{x}, ξ_{y} and ξ_θ are Gaussian white noise satisfying $\langle\xi_{\mathrm{i}}\rangle = 0$ and $\langle\xi_{\mathrm{i}}(t)\xi_{\mathrm{j}}(t')\rangle = \delta_{i,j}\delta(t-t')$.

For the reason that typically JPs move in a low Reynolds number regime, the inertial effects are neglected. For a non-chiral JP ($\Omega = 0$), the self-propulsion mechanism results in a directed motion, as illustrated in Fig. 4.2. Meanwhile, there are several real examples of chiral JPs in nature, such as *E. Coli* bacteria and spermatozoa performing helicoidal motion. The chiral JP ($\Omega \neq 0$), which is subjected to a torque, can also rotate with angular velocity Ω as shown in Fig. 4.3. Additionally, the direction of JP randomly varies with the time scale $\tau_\theta = 2/D_\theta$. As a result, the trajectory of the self-propulsion path approximately combines the self-propulsion length $l_\theta = v_0\tau_\theta$, and a circular movement with the radius $R_\Omega = v_0/|\Omega|$. Illustrated in Fig. 4.3, different R_Ω are compared under varying v_0 and Ω.

4.2 Finite difference equations

It is difficult to solve Eqs. 4.1-4.3 analytically, but the continuous-time solution $\{x(t),\ y(t), \theta(t)\}$ to Eqs. 4.1-4.3 can be approximated by a discrete-time sequence $\{x_i,\ y_i,\ \theta_i\}$, which is the solution of corresponding finite difference equation set. To derive the finite difference equations, we first treat the noise term with procedure by performing first order integration method, the stochastic Euler-algorithm, as follows [192]:

- Substitute $\{x(t),\ y(t),\ \theta(t)\}$ by $\{x_i,\ y_i,\ \theta_i\}$ in Eqs. 4.1-4.3 like

$$x(t) \longrightarrow x_i,\ y(t) \longrightarrow y_i,\ \theta(t) \longrightarrow \theta_i; \qquad (4.4)$$
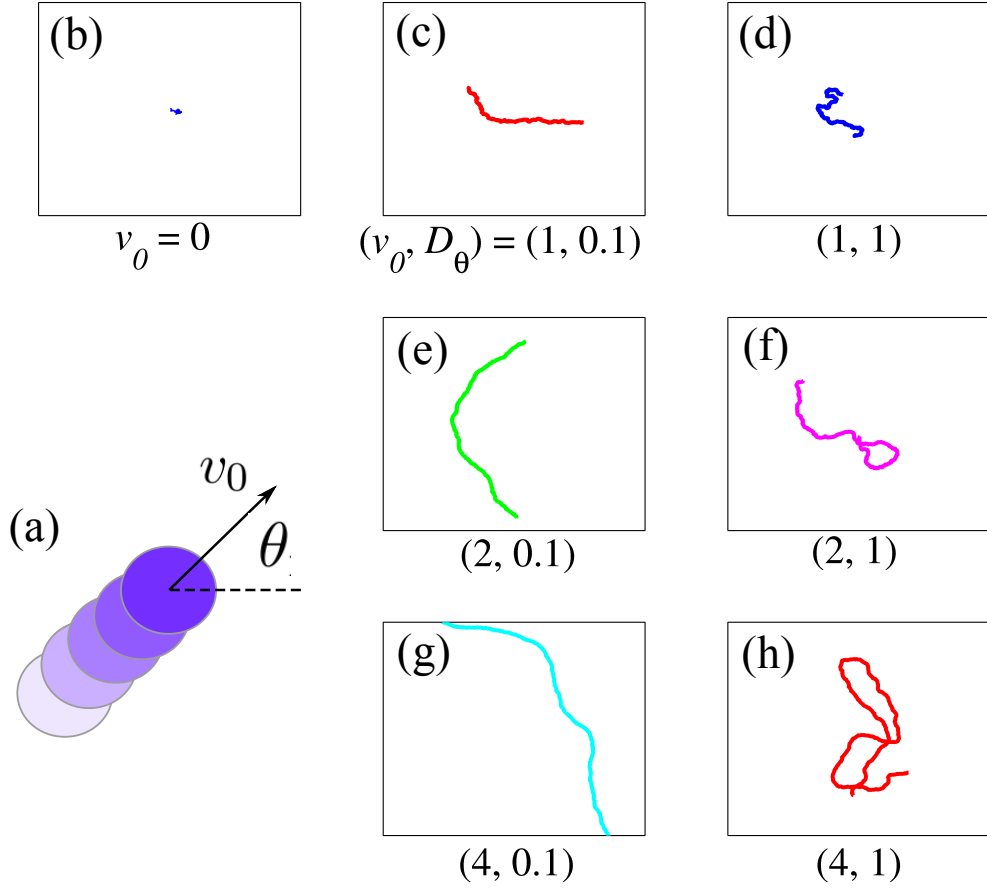
FIGURE 4.2: Trajectory examples of non-chiral active BM in 2D. (a) Illustration of a non-chiral active movement. The non-chiral JP is self-propelled by the speed of v_0, while undergoes Brownian diffusion both in translation and rotation coordinates. (b)-(h) Simulated trajectories of normal BM and non-chiral active BMs under different self-propulsion parameters respectively, shown in the same scale for comparison. Different appearances of the trajectory are due to the difference of self-propulsion lengths for each. The translational diffusion coefficient is set as the same level for all these simulations with $D_0 = 0.01$.

- Substitute first derivative of coordinates versus time by

$$\frac{d}{dt}x(t) \longrightarrow \frac{x_i - x_{i-1}}{\Delta t}, \quad \frac{d}{dt}y(t) \longrightarrow \frac{y_i - y_{i-1}}{\Delta t},$$

$$\frac{d}{dt}\theta(t) \longrightarrow \frac{\theta_i - \theta_{i-1}}{\Delta t}; \quad (4.5)$$

- Substitute the noise term by

$$\xi_x(t) \longrightarrow \frac{\xi_{x,i}}{\sqrt{\Delta t}}, \quad \xi_y(t) \longrightarrow \frac{\xi_{y,i}}{\sqrt{\Delta t}}, \quad \xi_\theta(t) \longrightarrow \frac{\xi_{\theta,i}}{\sqrt{\Delta t}}. \quad (4.6)$$

$\frac{\xi_{x,i}}{\sqrt{\Delta t}}, \frac{\xi_{y,i}}{\sqrt{\Delta t}}, \frac{\xi_{\theta,i}}{\sqrt{\Delta t}}$ are sequences of random numbers in standard Gaussian distribution. Technically, it is possible to generate Gaussian random numbers using Box-Müller algorithm or Marsaglia polar algorithm [193]. We simply call the random number generator functions from CUDA library "curand.h" in our program. Thus, we obtain the iteration functions after some arrangement of for later simulation as

$$x_i = x_{i-1} + v_0 \cos\theta \Delta t + \sqrt{2D_0 \Delta t}\, \xi_{x,i} \qquad (4.7)$$

$$y_i = y_{i-1} + v_0 \sin\theta \Delta t + \sqrt{2D_0 \Delta t}\, \xi_{y,i} \qquad (4.8)$$

$$\theta_i = \theta_{i-1} + \Omega \Delta t + \sqrt{2D_\theta \Delta t}\, \xi_{\theta,i} \qquad (4.9)$$

Consequently, the numerical solution of the time sequences $\{x_i,\ y_i,\ \theta_i\}$ can be obtained from the iterations Eqs. 4.7-4.9 above.

4.3   Active Brownian motion in the bulk

At the beginning, we consider the active BM of non-chiral JPs ($\Omega = 0$) in the bulk. Take $v_0 = 0$, then the particle is moving in the manner of passive BM with diffusion coefficient D_0, illustrated in Fig. 4.2(c,d). While v_0 increases, the movement with persistent length l_θ characterize the active trajectories in short time period, as shown in Fig. 4.2(d,f,h). For a better quantitative consideration, we calculate the time dependent MSD(τ), which is defined as

$$\text{MSD}(\tau) = \langle [(x(t+\tau) - x(t))^2 + (y(t+\tau) - y(t))^2] \rangle. \qquad (4.10)$$

In discrete-time presentation, MSD can be calculated from the coordinates of trajectories $\{x_i, y_i\}$, with time step $\Delta t = 10^{-5}$. According to the previous literature, the analytical result of MSD is given by

[26, 194]

$$\text{MSD}(\tau) \; = \; (4D_0 \; + \; v_0{}^2\tau_\theta)\tau \; + \; \frac{v_0{}^2\tau_\theta{}^2}{2}(e^{-2\tau/\tau_\theta} - 1) \qquad (4.11)$$

(a)

(b) $(v_0, \Omega) = (1, 0.1)$

(c) $\times 10$ $(10, 0.1)$

(d) $(1, 1)$

(e) $\times 10$ $(10, 1)$

(f) $(1, 10)$

(g) $(10, 10)$
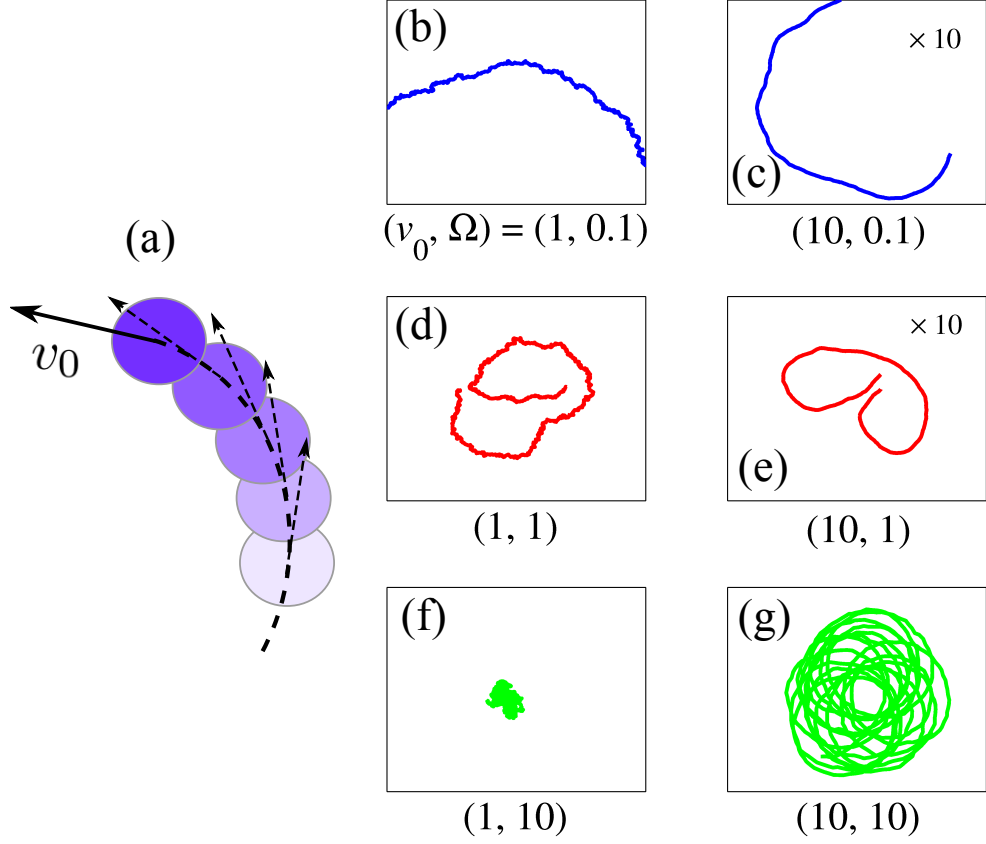
FIGURE 4.3: Trajectory examples of chiral active BM in 2D. (a) Illustration of a chiral active movement. The chiral-JP is subjected to a self-propelled velocity v_0 and also a torque with angular velocity Ω. (b)-(g) Simulated trajectories of chiral active BM under different parameters, drawn with the same length scale in (b)(d)(g)(f) and in 10 times larger scale in (c)(e). Different appearances of the trajectory are due to the difference of self-propulsion lengths $l_\theta = v_0\tau_\theta$ and chiral radius $R_\Omega = v_0/\Omega$. The other parameters are set as $D_0 = 0.01$, $D_\theta = 0.1$.

In the extremely short time scale with $\tau \ll \tau_\theta$, we can perform Taylor expansion on the exponential term in Eq. 4.11 as

$$e^{-2\tau/\tau_\theta} \; = \; 1 \; - \; 2\tau/\tau_\theta \; + \; \frac{-(2\tau/\tau_\theta)^2}{2!} \; + \; \cdots, \qquad (4.12)$$

in which the higher order terms are ignored. After inserting Eq. 4.12 into Eq. 4.11, we obtain that

$$
\begin{aligned}
\text{MSD}(\tau) & \simeq (4D_0 + v_0{}^2\tau_\theta)\tau + \frac{v_0{}^2\tau_\theta{}^2}{2}[-2\tau/\tau_\theta + \frac{-(2\tau/\tau_\theta)^2}{2!}] \\
& = 4D_0\tau + \frac{v_0{}^2}{\tau_\theta{}^2}\tau^2.
\end{aligned} \tag{4.13}
$$

Under the other limit with $\tau \gg \tau_\theta$, the exponential term approaches to zero, thus $\text{MSD}(\tau)$ of effective diffusion can be written as

$$
\text{MSD}(\tau) \simeq (4D_0 + v_0{}^2\tau_\theta)\tau. \tag{4.14}
$$

Combined with the numerical results shown in Fig. 4.4, we can conclude that the ballistic motion plays a dominating role with $\text{MSD}(\tau) \propto \tau^2$ in a small time scale $\tau \ll \tau_\theta$ when self-propulsion velocity $v_0 > 0$. For a long time scale $\tau \gg \tau_\theta$, the active BM becomes diffusive $\text{MSD}(\tau) \propto \tau$, with an enhanced diffusion coefficient $D_0 + v_0{}^2\tau_\theta/4$, compared with the passive BM with diffusion coefficient D_0.

Now we consider the active BM of chiral JPs ($\Omega \neq 0$). The simulated trajectories are shown in Fig. 4.3, which are almost clockwise circular movements under the modification of Brownian fluctuation. Similarly, we can obtain counterclockwise circular trajectories by resetting the chirality sign ($\Omega < 0$).

4.4 Active Brownian motion in confined geometries

In the last section, we briefly study the case of active BM of JPs in the bulk. In order to investigate the case with more realistic applications,
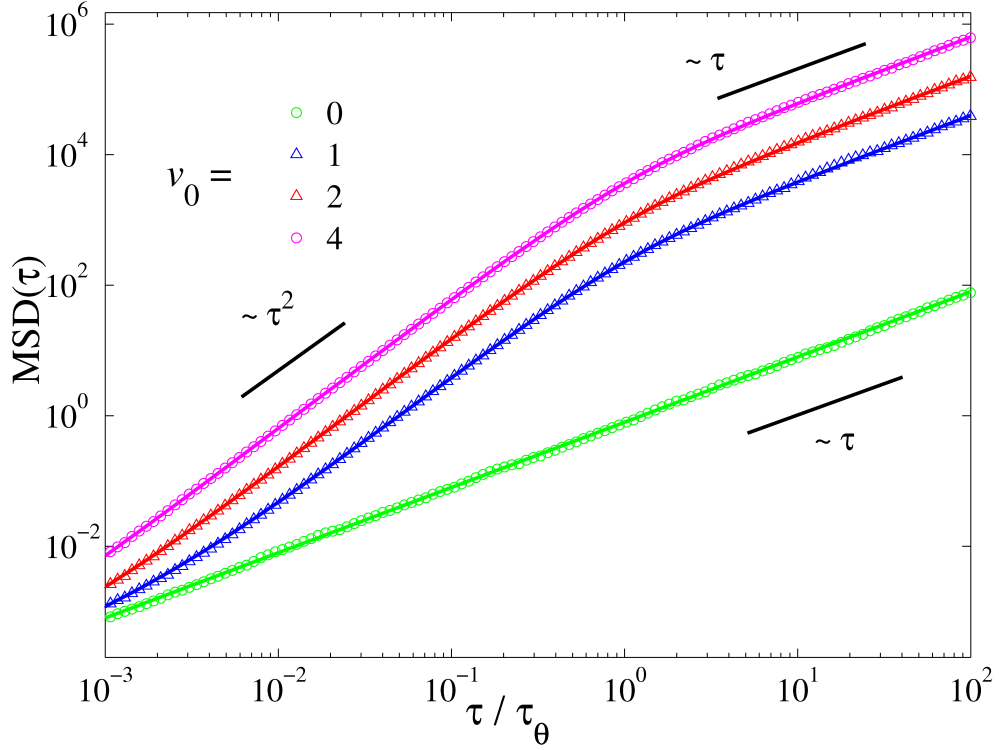
FIGURE 4.4: MSDs of active BM in the bulk are calculated under the different self-propulsion velocity v_0. For $v_0 > 0$, there is an additional transition in the profile of $MSD(\tau)$, compared with that of normal BM by setting $v_0 = 0$. The analytical results are shown in dashed line, which are in a good agreement with numerical results represented by dots. The other parameters are unified with $D_\theta = 0.1$ and $D_0 = 0.01$.

such as chemotactic bacteria spreading through porous polluted soils during bioremediation [195], we study in details of the case of active particles swimming within confined geometries. Intuitively, when the active particle encounters with an obstacle, it swims along the obstacle until its orientation pointing into the direction away from it. From the numerical point of view, the process can be simulated by reflective boundaries, which is shown in Fig. 4.5. In this thesis, we mainly focus on 2D narrow channels with an upper boundary represented by function $w_+(x)$ and lower boundary $w_-(x)$.
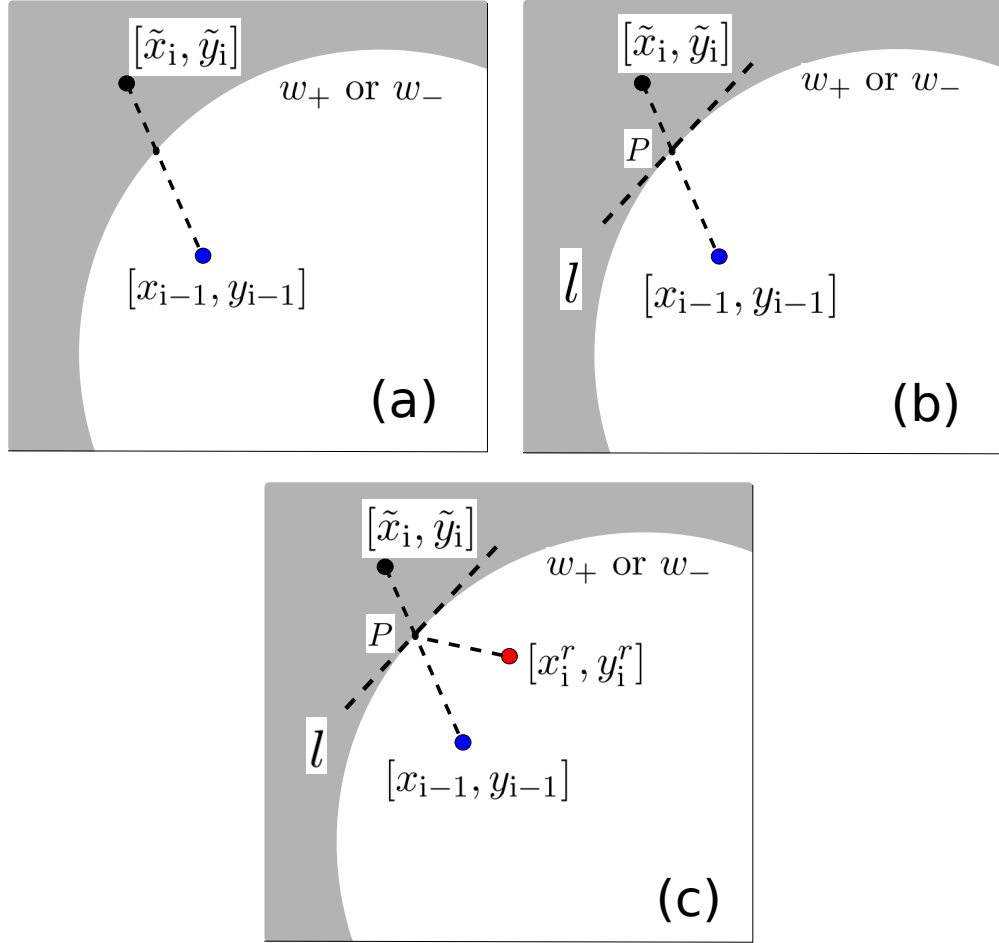
FIGURE 4.5: Implementation of sliding boundary algorithm. At every time step t_i, (a) first check if this intending position $[\tilde{x}_i, \tilde{y}_i]$ is out of the wall, which is forbidden; (b) if OUT, perform the reflecting algorithm by approximating the wall as its tangent l at the bounding position P; and (c) the particle is reflected to l obtaining $[x_i^r, y_i^r]$ after this reflective correction, and iterate.

4.4.1   Algorithm for boundary condition

When the confined geometry is considered, simulation of the diffusing of JPs requires the definition of its collisional dynamics at the boundary. With the assumption that the translational velocity undergoes elastic reflection, there are two possibilities of the boundary conditions regarding the different settings of the orientational dynamics. If θ is supposed to be unchanged during the collision, it turns to be sliding boundary condition described in Ref. [196]. The

other boundary condition can be employed if θ is assumed to be randomized [197].

(a) Sliding boundary condition with θ unchanged.

Under this assumption, JPs tends to slide along the boundaries for an average time of the order of τ_θ. They only leave the boundaries and are redirected towards the inside area of the channel due to the interference of $\theta(t)$ fluctuations, which can be regarded as a frictionless collisions. For simplicity, this sliding boundary condition is applied for all the simulation results displayed in this thesis. The detail procedures of this boundary algorithm is presented here.

When active particles approach to the boundary, the reflective implementation is achieved by modifying the intending position calculated from Eqs. 4.7 - 4.9. Note the present position of the active particle as $[x_{i-1}, y_{i-1}]$, the intending position as $[\tilde{x}_i, \tilde{y}_i]$, and the modified position $[x_i^r, y_i^r]$. During this reflecting process, θ_i keeps unchanged as required. The modification procedures are as follows.

1. Calculate the intending position $[\tilde{x}_i, \tilde{y}_i]$ according to Eqs. 4.7 - 4.9;

2. If $[\tilde{x}_i, \tilde{y}_i]$ is within the boundary, which satisfies $w_-(\tilde{x}_i) < \tilde{y}_i < w_+(\tilde{x}_i)$, assign $[x_i = \tilde{x}_i, y_i = \tilde{y}_i]$;

3. Otherwise, if $[\tilde{x}_i, \tilde{y}_i]$ is outside the boundary, as portrayed in Fig. 4.5,

   a. Calculate the intersection point P between the intending trajectory and boundary curve w_+ or w_-, with position $[x_p, y_p]$;

    b. Figure out the tangent line l along the boundary curve at P;

    c. Take l as the mirror line, calculate the mirror-symmetric point of $[\tilde{x}_i, \tilde{y}_i]$, which is represented as $[x_i^r, y_i^r]$;

    d. If the modified position $[x_i^r, y_i^r]$ is within the boundary, assign $[x_i, y_i] = [x_i^r, y_i^r]$;

    e. Otherwise, if the modified position $[x_i^r, y_i^r]$ is still outside the boundary, assign the $[x_i, y_i] = [x_{i-1}, y_{i-1}]$.

(b) Boundary condition with randomized θ

When θ is assumed to be randomized during the collision, rotation is thus induced by a tangential friction. This boundary dynamics makes JPs moving away rather than sliding along the boundaries. For this reason, the rectification function induced by the boundaries, such as ratchet, is suppressed as pointed out in Ref. [197]. Here we emphasize that in this thesis the boundary condition is only kept with *(a)*.

4.4.2   Numerics settings

Referred to App. A, this algorithm is realized within the compute unified device architecture (CUDA) framework [198], which is performed on a NVIDIA Tesla graphic processing unit (GPU). The significant precondition of this algorithm to be available is that, the average displacement for each step of a simulated trajectory should be significantly small compared to the distinctive size of the confinement, such as the bottleneck width of corrugated channels shown in Fig. 4.1(b). The precondition mentioned above enable us to estimate the boundary with its tangent line at its crossing point, and
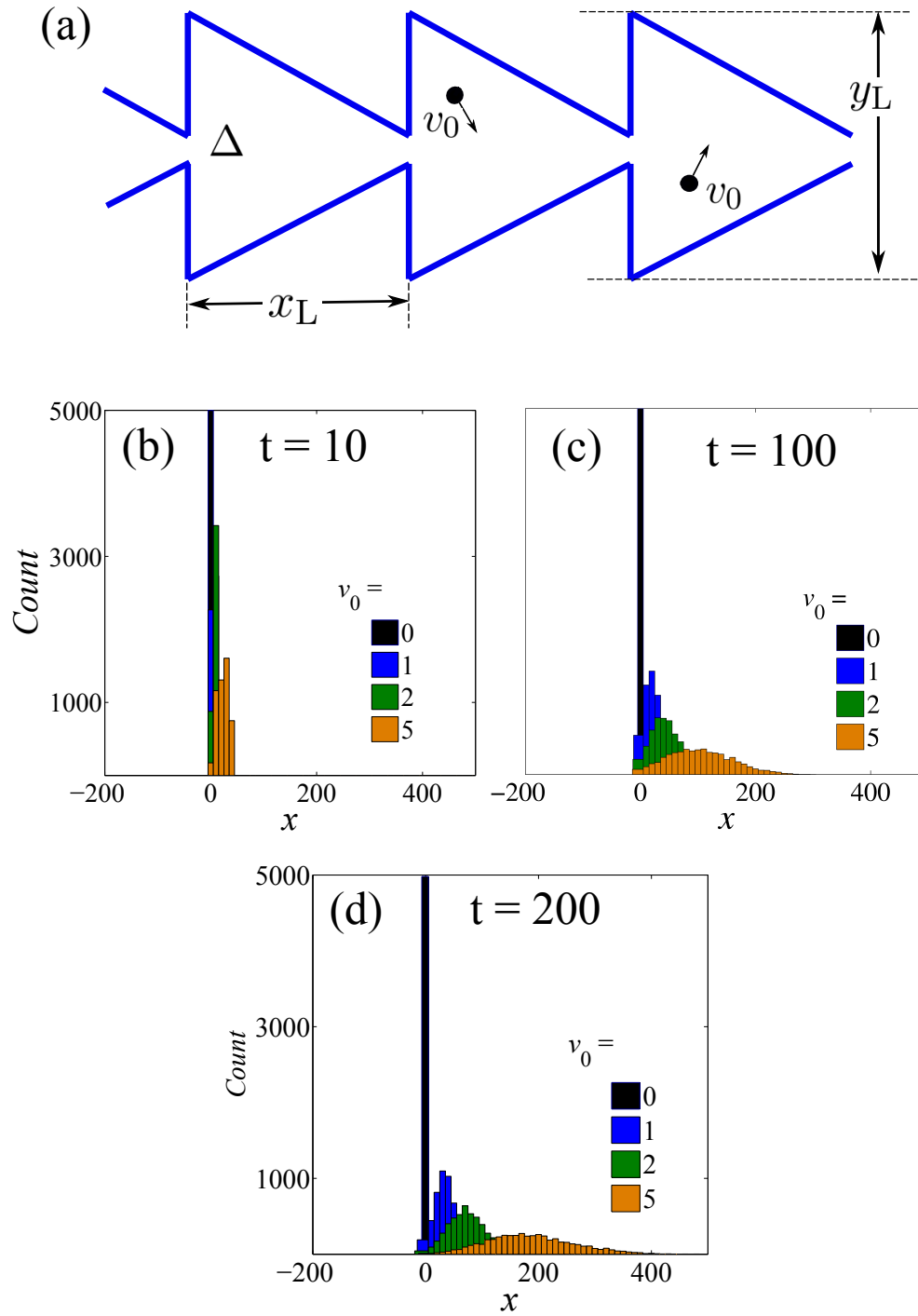
FIGURE 4.6: Rectification of active BM in a ratchet-like channel. (a) The ratchet-like channel along which the non-JPs diffuse in our simulation. The periodic channel can be extended in x-direction by this segment. (b)-(d) Histograms of x-position for JPs evolving after different time periods are calculated from 5000 trajectories for each graph, with the uniformed original positions at original point. The profiles with different self-propulsion velocity are compared, with the conclusion of the funneling effect induced by the ratchet for active particles. The other parameters applied are $D_\theta = 0.1$, $D_0 = 0.01$.

we can only consider one boundary once at a time, which realizes the simulation simplified. To avoid the instability of the numerics when the particle is near to the sharp corner, like the case shown in Fig. 4.6(a), the time step Δt should remain rather small. We keep Δt as 10^{-5} in the following simulation in Chap. 5 and 6.

On modeling the boundary conditions, note again that we can make following simplifications based on the assumption of zero-sized particle. The influence of the particle distance from the walls on the self-propulsion mechanism can be ignored, as well as the hydrodynamic interactions between particle and walls [199]. For the situation of the accumulation of particles against walls, the treatment can remain as the simplest with extra complexities ignored [200].

4.4.3 Example: Rectification by a ratchet-like channel

Unlike the left-right symmetric channel shown in the illustration Fig. 4.1(b), when the 2D channel is asymmetric along its transport direction, e.g. ratchet-like channel illustrated in Fig. 4.6(a), the boundary contributes to rectification of active BM of JPs. The evolution of the probability density of the particles is shown in Fig. 4.6, the particles are released from the same initial position at $t = 0$. By taking different v_0, the diffusion motion of passive and active Brownian particles are compared. We observe that the active particles can be funneled by the ratchet-like channel, which is resulted from the average directed motion carried out on the active particles. This effect has been applied in a sorting mechanism to separate active particles according to different self-propelled velocity v_0 [148]. This motion rectification is considered to be induced by the geometric asymmetry of the channel, which is further discussed in Chap. 5.

4.5   Summary

The approach proposed in this section can be further applied to more complicated cases, as mentioned in Ref. [201]. For the reason that active particles are far away from thermal equilibrium in the environment, ideas for separating, trapping or sorting can be actualized by designing certain shape of barriers correspondingly [196]. What is interesting as an extension, one can consider the case of the spherical active particle moving in 3D geometries, in which we can use 3D displacement coordinates and two-degree freedom of orientation to present the particle position and the orientation respectively.

Chapter 5

Autonomous transport of active particles in channels

First, we study autonomous transport of a JP in two different kinds of channels in 2D. In order to characterize the autonomous current it causes, we introduce the rectification power

$$\eta = \frac{|\bar{v}|}{v_0},$$ (5.1)

in which $\bar{v} = \lim_{t\to\infty}\langle v(t)\rangle = \lim_{t\to\infty}\langle x(t) - x(0)\rangle/t$.

In Chap. 4, the Langevin equations are simulated for the active particles in a periodic channel with triangular compartments, shown in Fig. 4.6. It is found that the triangular compartment channel tends to funnel the particle to the right direction with $\bar{v} > 0$. This funneling effect is mainly due to the asymmetry in left-right direction. In this section, we calculate the rectification power and discuss on the autonomous transport of a non-chiral and chiral active particle in left-right asymmetric channel. After that, we extent the discussion into the chiral active transport in upside-down asymmetric channel. We assume the channel with small width of bottleneck and the thermal noise level is relatively low, so that we can consider that the

bottleneck and thermal fluctuation play no significant role in this transport issue. Most of the results in this section are presented in our recent paper Ref. [202].

For later use of the simulation and the explanation, we take rescaling steps as follows. The spacial coordinates can be first rescaled as $x \rightarrow x/\lambda$ and $y \rightarrow y/\lambda$, with its dimensions conveniently set to $x_L = y_L = 1$. Similarly, the time is rescaled as $t \rightarrow v_0 t/\lambda$. For simplicity, if we assign self-propulsion velocities as a constant value, the result of our numerical simulation should only depend on following characteristic lengths: the self-propulsion length, l_θ ; the thermal length, D_0/v_0;the bottleneck width, Δ; and the chiral radius, R_Ω, which are compared with the compartment dimensions set to one.

For our simulation analysis, we prefer the dimensionless quantities such as τ_θ/τ_x and $\Omega\tau_\theta$, in which τ_θ is the self-propulsion time, Ω representing the chiral frequency and $\tau_x = x_L/v_0$ a characteristic compartment crossing time.

5.1   Non-chiral JPs in a left-right asymmetric channel

For non-chiral JPs, $\Omega = 0$, the results of previous study were first reported in [196]. In the following subsections we study the parameter dependences of the autonomous transport of the non-chiral JPs.

5.1.1 The role of persistent length

From the brief study in Chap. 4, the rectification function is found of the active particle in a ratchet-like channel while increasing the self-propulsion velocity as shown in Fig. 4.6. Here we look into the role of the persistent length $l_\theta = v_0 \tau_\theta$ by simulating the active Brownian motion in the steady-state under different v_0 and D_θ, while keeping the thermal noise level D_0 unchanged. The plots of the probability density function (PDF) of non-chiral JPs in logarithmic contour plots are displayed in Figs. 5.1,5.2, with varying l_θ. Obviously shown in Fig. 5.1(d) and Fig. 5.2(a), the funneling effect is enhanced when l_θ is increasing.

In Fig. 5.3, it shows that the rectification power in varying τ_θ with fixed v_0 and D_0. Since the active particles ballistically move with a self-persistent length, the particles may undergo collisions during the time period of τ_θ, when the self-propulsion length l_θ is larger than the scale of the channel compartment. While the self-propulsion length l_θ is increasing, the movement of the active particle is considerably more sensitive to the confinement. For different fixed v_0 and D_0, the rectification power is creasing monotonously with l_θ, until it reaches to a upper limit, seeing Fig. 5.3.

At large τ_θ, that is, when D_θ is rather small, microswimmer diffusion is of Knudsen type and the rectification power is dominated by self-propulsion mechanism. It is worth to mention that, the upper limit value of η is much higher than the rectification power induced by thermal ratchets studied in the early literature Ref. [167].

FIGURE 5.1: Stationary PDF of non-chiral JPs in a triangular channel with varying v_0, drawn in logarithmic contour plots. The triangular compartment is of the size $x_L = y_L = 1$ and the pore width $\Delta = 0.1$. The PDFs under different self-propulsion velocity are compared, with the other parameters fixed as $D_\theta = 0.1$, $D_0 = 0.01$.

5.1.2 The impact of the thermal noise

While fixing the self-propulsion velocity v_0 and rotational diffusion coefficient D_θ, the plots of PDF under different thermal noise levels are shown in Fig. 5.4, for investigating the impact of the thermal noise.

Mentioned in the previous literature Ref. [196], the self-propulsion velocity changes its direction rapidly for $l_\theta \ll x_L$, usually before the particle reaches to the confinement. As illustrated in Fig. 5.5, the curves are the rectification power η under varying D_0 with different fixed D_θ. The thermal fluctuation acts as a lubricant, push the

FIGURE 5.2: Stationary PDF of non-chiral JPs in a triangular channel with varying D_θ, drawn in logarithmic contour plots. The triangular compartment is of the size $x_L = y_L = 1$ and the pore width $\Delta = 0.1$. The PDFs under different rotational diffusion coefficients are compared, with the other parameters fixed as $v_0 = 1$, $D_0 = 0.01$.

particles towards the central area of the channel. As a comparison, for $l_\theta \gg x_L$, the thermal noise impels the particle to get over the blocking action of the corner of the corrugated channel which can suppress the rectification, shown in Fig. 5.4.

5.1.3 The effect of asymmetry degree of compartment

As to the practical cases of boundaries with diverse shapes, we investigate the robustness of the rectification effect for active particles in triangular-compartment channel with the different degree of asymmetry. In order to vary the degree of asymmetry, we modify the
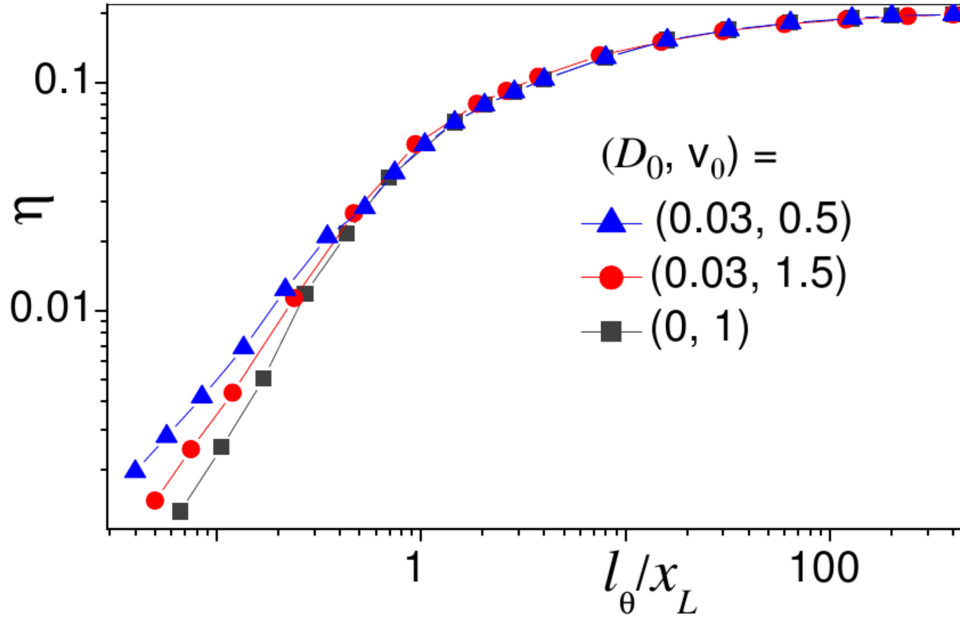
FIGURE 5.3: The dependence of rectification on self-persistent length for non-chiral JPs in a triangular channel, under the different D_0 and v_0. The other parameters are $x_L = y_L = 1$ and $\Delta = 0.1$.

compartment shape by introducing the tuning parameter x_0, which is the corner coordinate from 0 to $x_L/2$, and η is calculated as shown in Fig. 5.6. It can be immediately observed that η decreases to its half for x_0 up to 0.2. In Ref. [196], the conclusion was made that the rectification is quite insensitive to the rescale factor of the compartment λ in the Knudsen regime $l_\theta > \lambda x_L$.

For the regime with very large λ, according to the rescaling steps mentioned in the beginning of this chapter, the rescaled intensity of noise $D_0/\lambda v_0$ turns out to be very small. Under this circumstance, the thermal fluctuation plays a role with no significance. As a result, η is closing to a constant as shown in Fig. 5.6, equivalently speaking, $\bar{v}$ is proportional to λ^{-1}.

Concluded by the authors in Ref. [196], for very narrow bottleneck, $\Delta \ll y_L$, Δ causes a little influences on η, that is, η slightly decreases
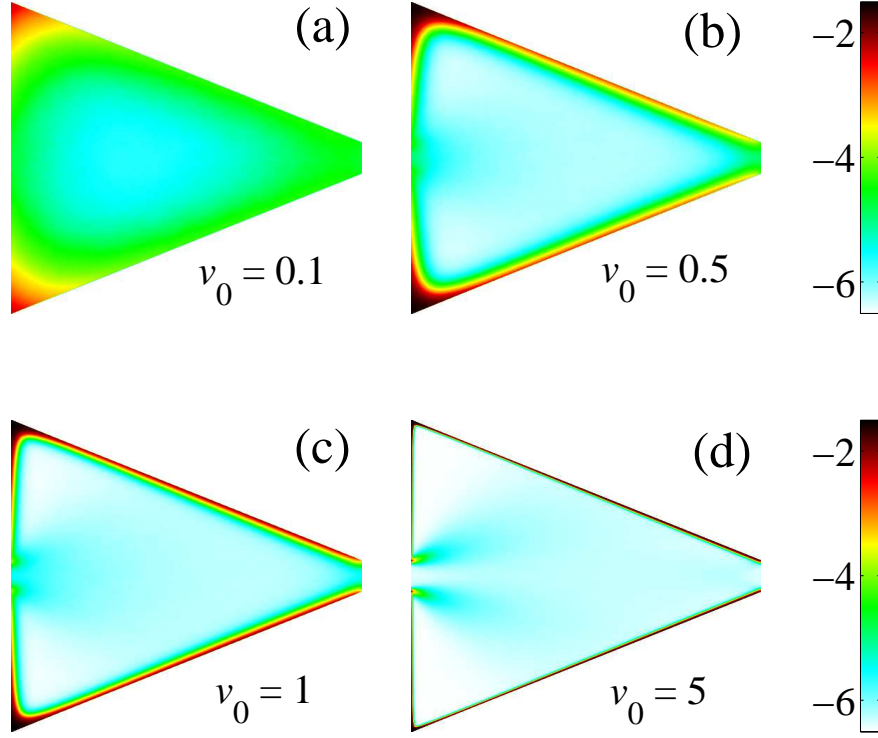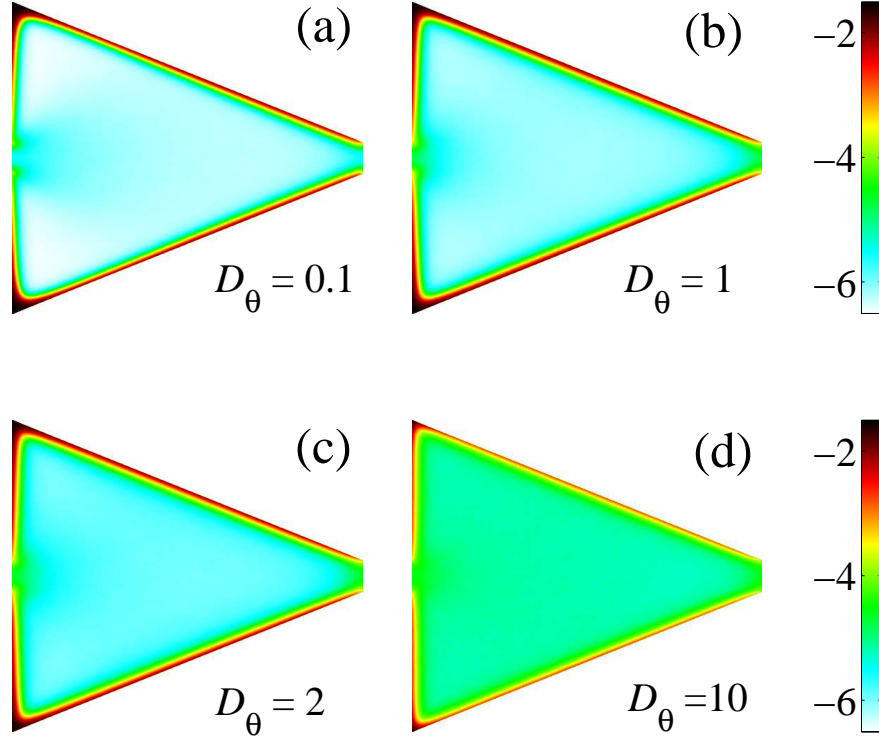
FIGURE 5.4: Stationary PDF of non-chiral JPs in a triangular channel with varying D_0, drawn in logarithmic contour plots. The triangular compartment is of the size $x_{\mathrm{L}} = y_{\mathrm{L}} = 1$ and the pore width $\Delta = 0.1$. The PDFs under different rotational diffusion coefficients are compared, with the other parameters fixed as $v_0 = 1$, $D_\theta = 0.05$, $l_\theta = v_0 \tau_\theta = 40 \gg x_{\mathrm{L}}$.

when reducing Δ. The reason is that, the sidewalls of the compartment become longer with the shrinking bottleneck, thus it is more time-consuming for the particle to slide along them until they reach to the exit of the bottleneck. From another point of view, the flow of the movement in negative direction is obstructed mostly at the compartment corners, with nearly no relevance of the bottleneck size. This finding provides the evidence of extending this numerical study on JPs into more practical active swimmers with a finite radius.
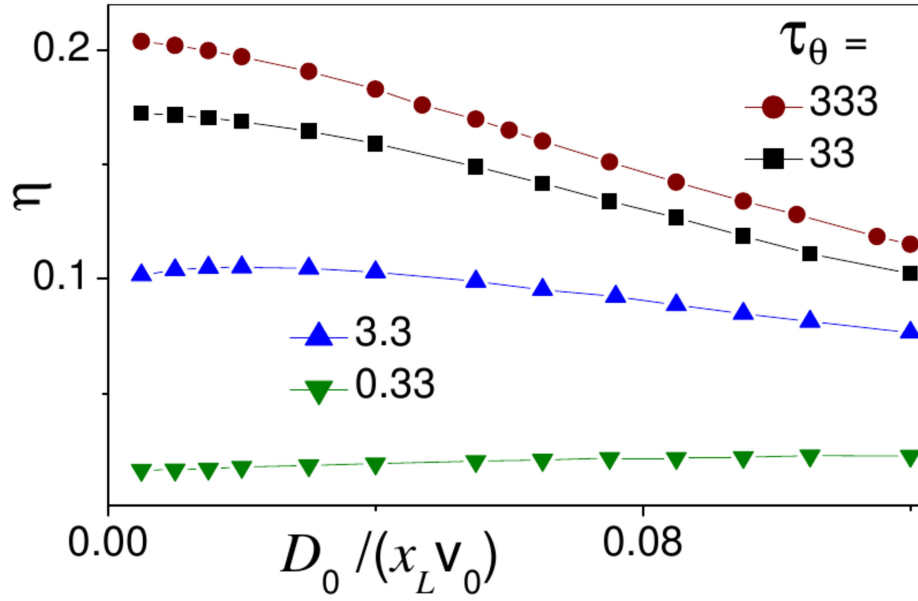
FIGURE 5.5: Rectification power *vs.* D_0 for non-chiral JPs in a triangular channel, for $v_0 = 1$ and different D_θ The triangular compartment is of the size $x_L = y_L = 1$ and the pore width $\Delta = 0.1$.
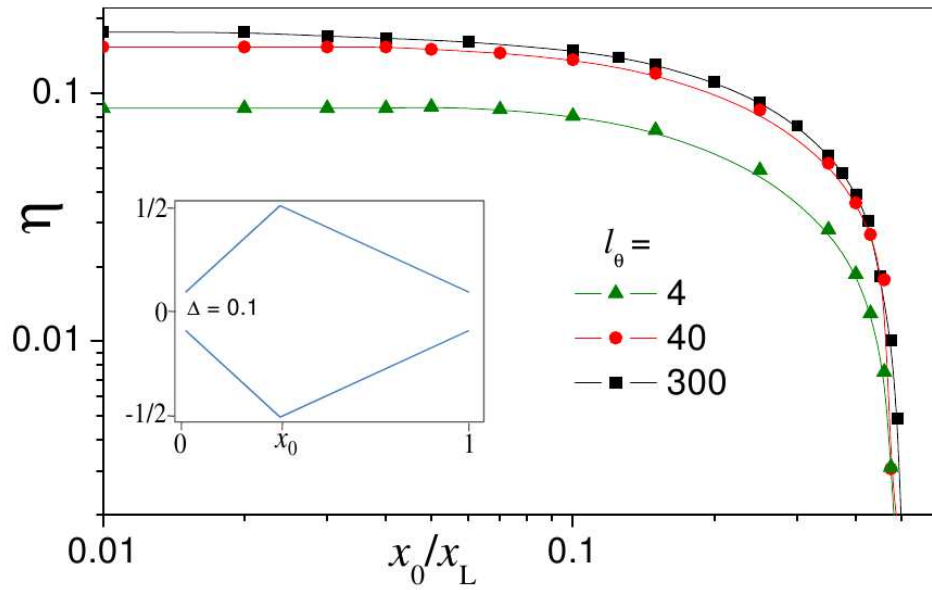
FIGURE 5.6: Effect of asymmetry degree on the rectification of a non-chiral JP in a triangular channel. A typical compartment is illustrated in the inset, with $x_L = y_L = 1$ and $\Delta = 0.1$, while the corners are variable by setting x_0. The parameters are $v_0 = 1$, $D_0 = 0.03$ for the curves η vs. x_0 under different D_θ.

5.2 Chiral JPs in a left-right asymmetric channel

In this section, we discuss on the rectification of a chiral active particle in a left-right asymmetric channel. The parameters dependence are studied and shown in the following simulation results for the confined transport of the chiral JPs.

5.2.1 Funneling effect affected by chirality

It is observed that the funneling effect of the active particles can be induced by left-right asymmetric channel mentioned in Chap. 4. However, the chirality can make a negative influence on such effect, shown in Fig. 5.7. From the plot of PDF we can find that the funneling effect of the triangular ratchet is weakened when $\Omega > 0$, by decreasing the boundary flows.

5.2.2 The impact of chirality on the transport

As it is discussed so far, the chirality Ω can provide a function as the angular bias, which can affect the autonomous funneling effect in the strong chirality regime. In Fig. 5.8, we numerically research on the rectification power of chiral JPs in the triangular channel of Fig. 4.6, and compare the rectification under different Ω. It can be found that, under smaller Ω, the rectification power η goes up as τ_θ increases, and finally reaches its horizontal asymptote monotonically.

Nevertheless, it turns out to be considerably different for larger Ω. In this case, the rectification power η goes up and down as τ_θ increasing, which makes a distinct maximum of η, and finally it approaches to a lower asymptote value, see Fig. 5.8. From the observations above,
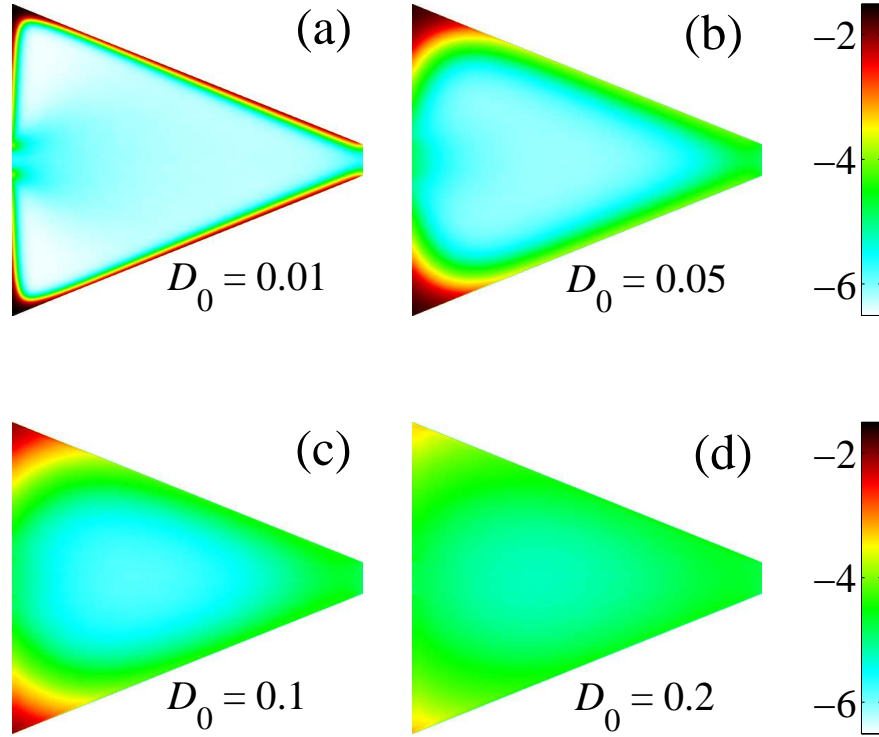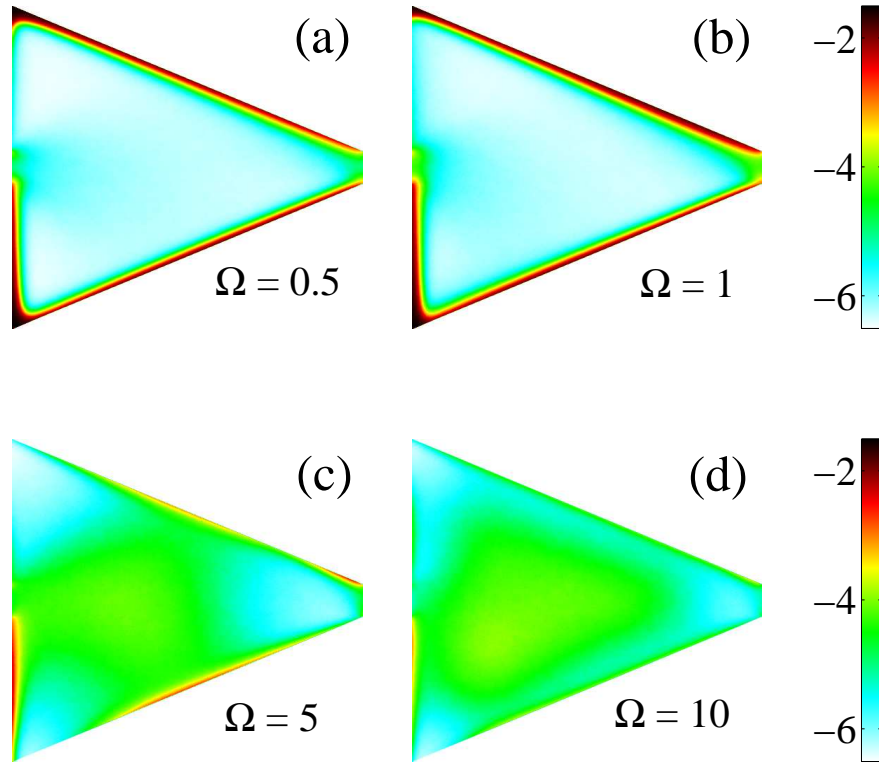
FIGURE 5.7: Stationary PDF of chiral JPs in a triangular channel, drawn in logarithmic contour plots. The triangular compartment is of the size $x_{\mathrm{L}} = y_{\mathrm{L}} = 1$ and the pore width $\Delta = 0.1$. The PDFs under different chirality are compared, with the other parameters fixed as $v_0 = 1$, $D_\theta = 0.1$, $D_0 = 0.01$.

we can conclude that the regimes of weak and strong chirality can be distinguished approximately.

We consider the comparison of two characteristic time scales, the auto-correlation time of its self-propulsion velocity $\tau_\theta/2$ and the reciprocal of the cyclotron frequency Ω. If they are of the same order of magnitude, namely τ_θ, the chiral nature of the active particle dynamics can be considered influential. This simple argument turns out to be in a good agreement with the locate of the maxima of η in the inset of Fig. 5.8.

The dependence of the rectification power on Ω is illustrated in Fig.

FIGURE 5.8: Rectification of a chiral JP vs. τ_θ in a triangular channel, under the different chirality. Here the parameters are $D_0 = 0.03$, $v_0 = 1$, and $\tau_{\mathrm{x}} \equiv x_{\mathrm{L}}/v_0$.

5.9. Independently of the level of translational noise D_0, we can find that η does hardly rely on the chiraly Ω as its increasing. From a certain value of Ω, the rectification power η decreases dramatically to zero.

We can notice that there is a so-called threshold value of Ω for the rapid dropping of η. Here we name it as Ω_{M}. As Ω increasing, the chiral radius $R_\Omega = v_0/\Omega$ decreases at first, while thΩ continuing with going up, R_Ω becomes small enough so that the active particle can perform a full circular movement within a certain compartment, without bouncing to the channel walls. We can consider to estimate Ω_{M} as the Ω at this transition point. For an insightful observation, it is declared that the trajectory of this movement is actually a logarithmic spiral with exponentially small steps [145].

As an approximation, we take the noiseless limit $D_0 \to 0$, and assume that the self-propulsion time is sufficiently long enough with $\Omega_{\mathrm{M}}\tau_\theta > 1$. In this case, the threshold value Ω_{M} satisfies $2R_\Omega$, which gives

$\Omega_{\mathrm{M}} = 2v_0/x_{\mathrm{L}}$. Under this estimation of Ω_{M}, we can obtain a good explanation for the curves shown in Fig. 5.9. Furthermore, this estimation can be applied to interpret the peaks in Fig. 5.14 which comes later in Sec. 5.3.3.

As shown in the inset of Fig. 5.9, it is remarkable to mention that while Ω increasing, the horizontal asymptote of average velocity $\bar{v}$ change from positive value to negative value. Discussed by the previous literature [167], this turns out to be as an example of the reversal current effect, which occurs in a ratchet-like channel.

With a very large chirality Ω, the chiral movement radius is smaller than or comparable with the width of the bottleneck, namely, $R_\Omega \simeq \Delta$. In this situation, we can imaging that the movement of the active particle does not influenced much by the pore crossing. Under such strong chirality, the self-propulsion mechanism is suppressed and thus the particle's movement can be approximated with an effective translational fluctuations. This is a colored noise, with time constant τ_θ, to be added to the white noise with constant D_0, referred to the discussions in Chap. 6.

5.3 Chiral JPs in an upside-down asymmetric channel

Following the last section, in this section we discuss the autonomous transport of active particles moving in upside-down asymmetric channels, illustrated in Fig. 5.10. Due to the self-propulsion mechanism, the active particle tends to slide along the wall once touching the boundary. Under this set-up, we can imagine for non-chiral active
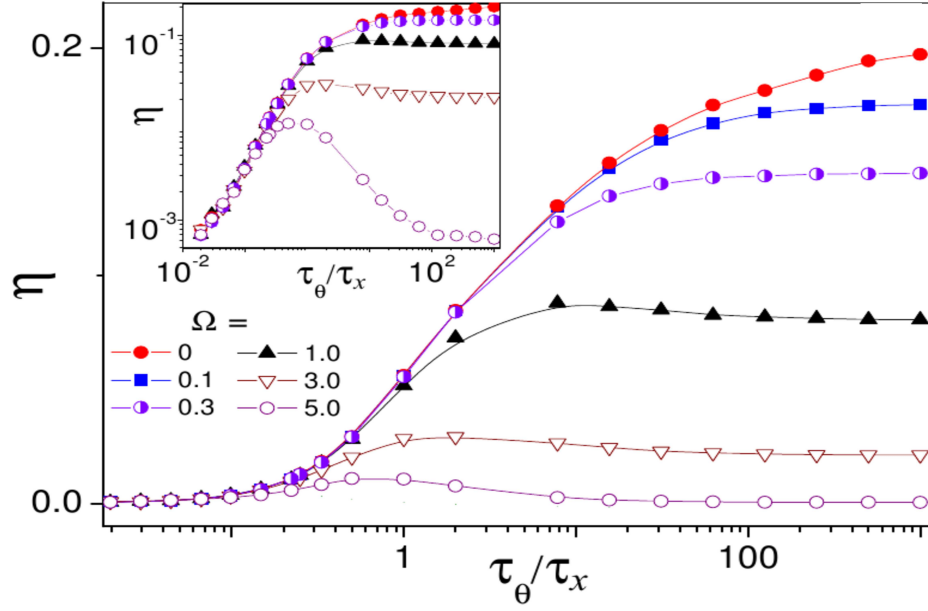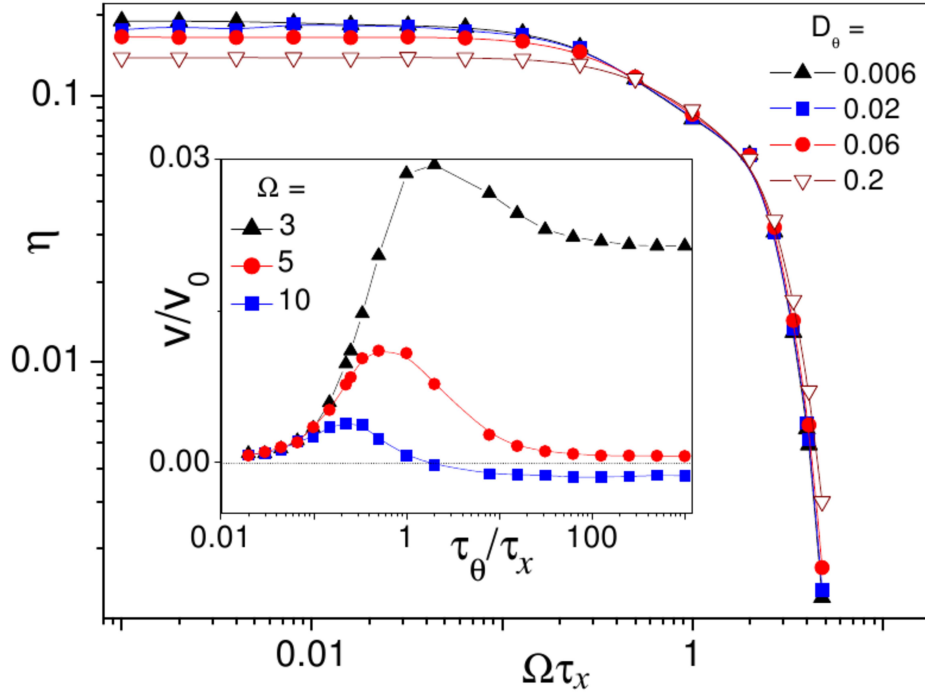
FIGURE 5.9: Rectification of a chiral JP *vs.* Ω in a triangular channel, under the different D_θ. Here the parameters are $D_0 = 0.03$, $v_0 = 1$, and $\tau_\mathrm{x} \equiv x_\mathrm{L}/v_0$.

particles without the external torque driven, probabilities for a certain particle to sliding to left and right are equal when JPs touch such boundary with left-right symmetric shape. Thus, we can conclude that there is no autonomous transport on the whole for active particles in upside-down asymmetric yet left-right symmetric channels. Consequently, it is only necessary to consider the transport effect of chiral active particles with $\Omega \neq 0$ in upside-down asymmetric channels.

5.3.1 Definition of an upside-down asymmetric channel

For quantitative study later in this section, we introduce the periodic upside-down asymmetric channel as follows

$$w_+(x) = \frac{1}{2}\left[\Delta + \epsilon(y_\mathrm{L} - \Delta)\sin^2\left(\frac{\pi}{x_\mathrm{L}}x + \frac{\phi}{2}\right)\right], \qquad (5.2)$$

$$w_-(x) \;=\; -\frac{1}{2}\left[\Delta \;+\; (y_\text{L}-\Delta)\sin^2\left(\frac{\pi}{x_\text{L}}x\right)\right], \qquad (5.3)$$

where x_L denotes the compartment length, y_L the channel width, and Δ the bottleneck size. There are two geometrical parameters introduced in $w_+(x)$ for varying the upside-down asymmetric degree, namely ϵ and ϕ. ϵ is defined as positive real number for tunning the amplitude of the upper wall compared to the lower wall, and ϕ is for tuning the shift of the upper wall from corresponding position of lower wall, referred to Figs. 5.10, 5.15.
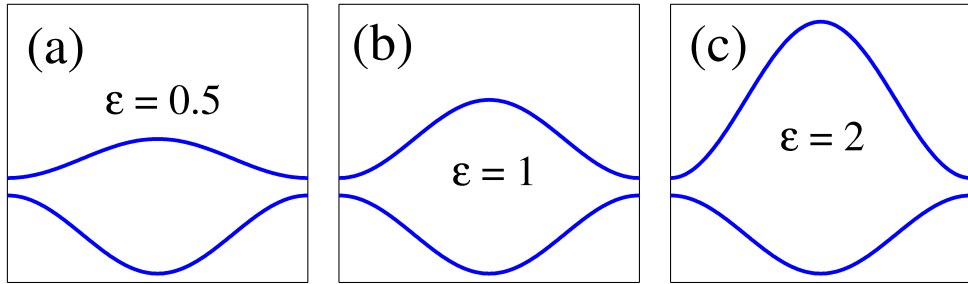
FIGURE 5.10: Illustrations of upside-down asymmetric channels for different shape parameter ϵ with $\phi = 0$.

5.3.2 The effect of the degree of asymmetry

For the reason of the self-propulsion mechanism, the active particle has a tendency of aligning its velocity parallel to the boundaries, if the size of the channel compartment is smaller than its self-propulsion length, namely $l_\theta < x_\text{L}$ [126, 148]. As the result, for the chiral active particles, there are two flows produced by upper boundary and lower boundary respectively, which flow towards the opposite directions. With the different curvature of the upper and lower boundaries, the autonomous transport flow can be induced in this way, shown in the plots of PDF of chiral active transport in upside-down asymmetric channel in Fig. 5.11.
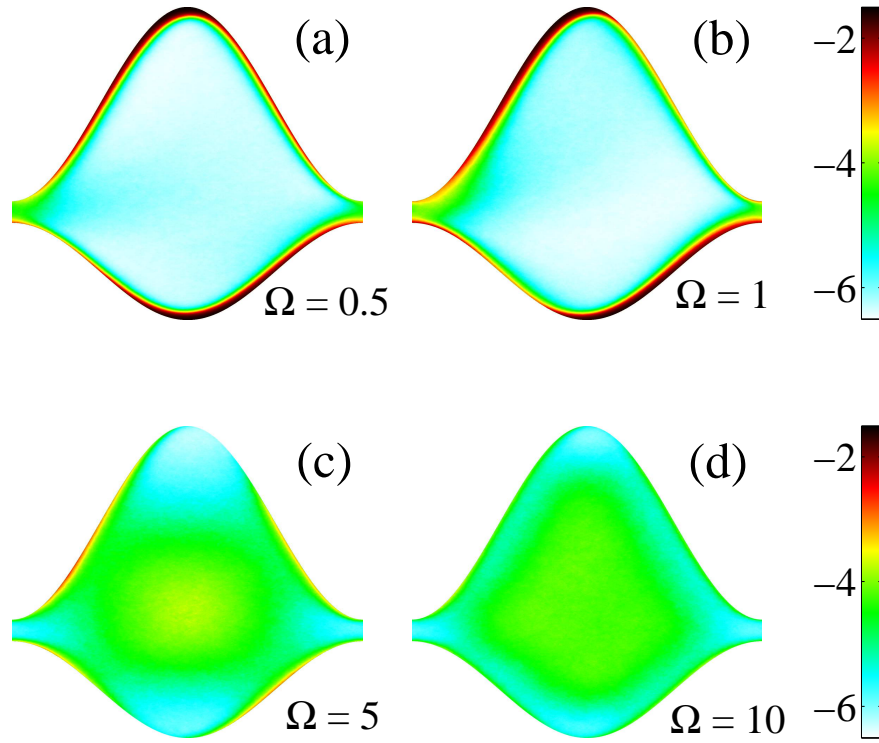
FIGURE 5.11: Stationary PDF of chiral JPs in upside-down asymmetric channels, drawn in logarithmic contour plots. The triangular compartment is of the size $x_L = 1$ and $\epsilon = 2$ and the pore width $\Delta = 0.1$. The PDFs under different chirality are compared, with the other parameters fixed as $v_0 = 1$, $D_\theta = 0.1$, $D_0 = 0.01$.

For $\Omega > 0$, the active particle is so-called "levogyre" with the counterclockwise orbit. Obviously, we can obtain the result intuitively that the upper and lower flows caused by boundaries are steered to the left and right, respectively. Thus, normally there is a net ow along the free direction of channel axis, which is the autonomous transport as expected. Not difficult to find out that, the average velocity of the particles $\bar{v}$ turns out to takes the same sign of the ow carried by the boundary with less corrugated curvature. To explain it explicitly, if $\epsilon < 1$, the direction of net flow should be the same with that of the upper boundary flow, and for $\epsilon > 1$, the net flow is in the same direction with lower boundary flow. The flow vanishes

when $\epsilon = 1$ that the channel is in upside-down symmetry.

The numerical simulation is performed for calculating the average velocity versus the asymmetry parameter ϵ under different chirality Ω, shown in Fig. 5.12. The mechanism of the reverse flow of the active particles in upside-down asymmetric channel above can be applied to explain the division of negative and positive average velocity in Fig. 5.12. The inset figure within Fig. 5.12 shows the dependence of the autonomous current on the shift between the upper and lower boundary ϕ, under the fixed ϵ and chirality Ω.
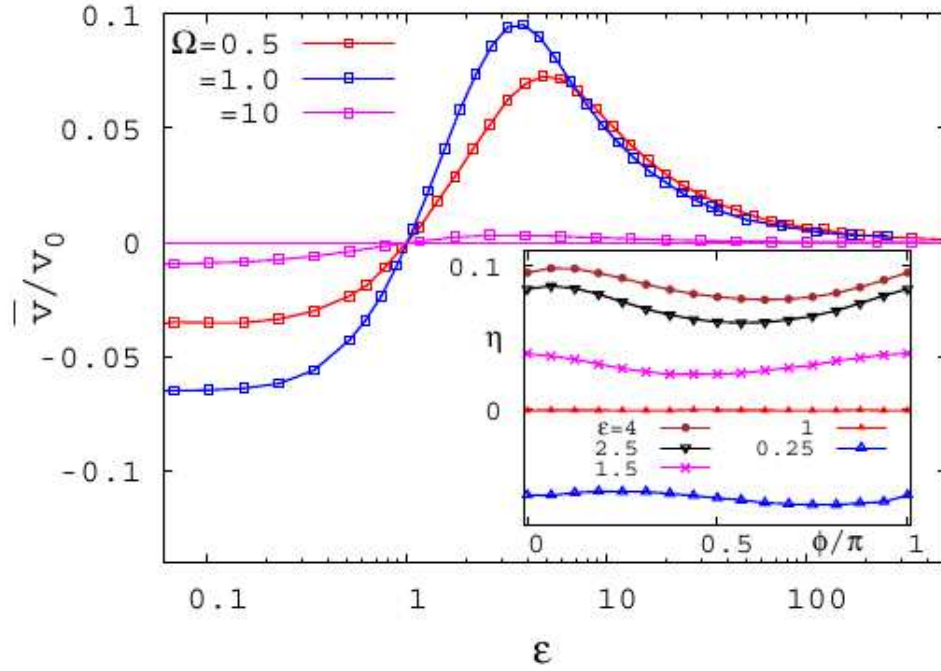
FIGURE 5.12: Dependence of rectification on the asymmetry degree for chiral JPs in upside-down asymmetric channels, shown in the curve of $\bar{v}/v_0$ *vs.* ϵ under different chirality. The inset figure shows η *vs.* ϕ under the different asymmetry degree parameter ϵ. The other parameters here are $\Delta = 0.12$, $D_0 = 0.01$, $D_\theta = 0.3$, $v_0 = 1$.

5.3.3 Optimization of the rectification of JP transport

For the chiral active particles, researching on the influence of thermal fluctuation D_0 and rotational fluctuation D_θ on the rectification

power $\eta\, D_0$ may give a hint for the optimization of the autonomous transport. As illustrated in Fig. 5.13, the dependence of η on D_0 and D_θ are studied while fixing the chirality with different Ω values [203].
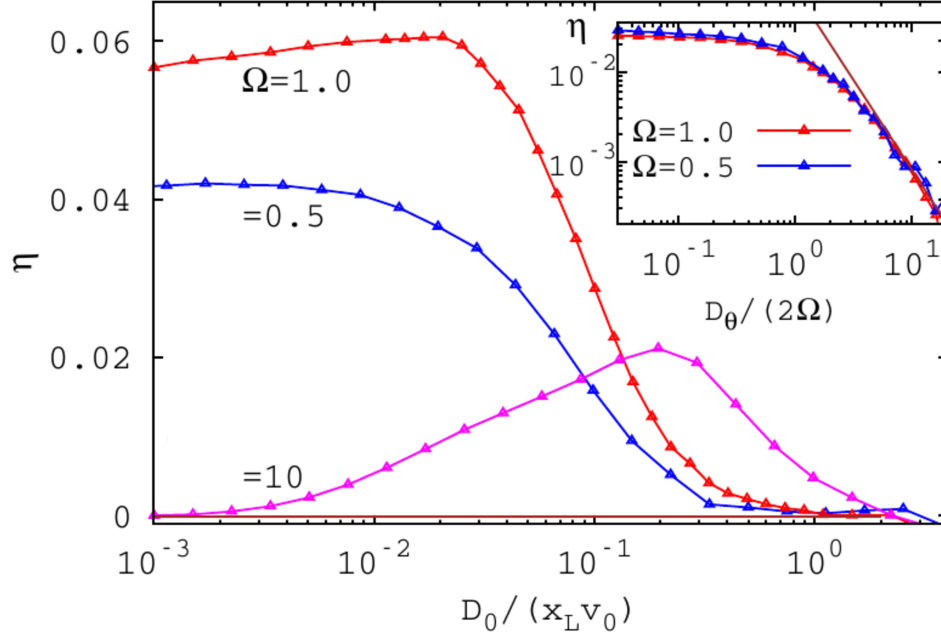
FIGURE 5.13: Optimization of the rectification as a function of D_0 of chiral active transport , under the different chirality. The channel parameters are set as $x_L = y_L = 1$, $\Delta = 0.08$, $\epsilon = 0.25$, $\phi = 0$. The other parameters are $v_0 = 1$, $D_\theta = 0.1$. The inset graph shows η *vs.* D_θ under different chirality with $D_0 = 0.05$, the other parameters are the same.

When we consider the active particle in weak chirality, the rectification power η is proportional to $(\Omega\tau_\theta)^2$. Meanwhile, under the extremely strong chirality with $\Omega\tau \gg 1$, the orientational noise term can be neglected in Eq. 4.3. Thus, the autonomous transport current should only depend on the amplitude of thermal fluctuation D_0 and the chiral radius $R_\Omega = v_0/\Omega$, when the geometry of the boundary is fixed and the self-propulsion velocity v_0 is considered to be a constant, as $v_0 = 1$ is applied in the simulation for Fig. 5.13. Observed from this figure, as the chirality is in low frequency, the rectification

power η is decreasing monotonically while D_0 is increasing. Differently, When the chirality is taken high frequency, η goes up and reaches a maximum and decreases when D_0 is increasing. However, no matter the chiral frequency is high or low, the rectification power finally decays to zero when D_0 is relatively large, $D_0 \gg v_0|\Omega|$. With such analysis, the optimization of the rectification of levogyre active particle can be realized by tunning D_0 as one of the functional parameters.

In order to figure out an optimal value of Ω, which is another parameter for the optimization of the rectification of the transport of active particle. Ideally out of intuition, it is expected that the particle will incline to gather at the corrugated wall with the tangential velocity close to $\pm v_0$ under an optimal value of Ω and small fluctuation. As to the requirement of the optimization of rectification, it is reported in Ref. [203] that the condition is in strong chirality $\Omega\tau_\theta \gg 1$, and low noise level $v_0|\Omega|/D_0 \gg 1$.

Indeed, when the chiral radius is very large which exceeds the size of the compartment $R_\Omega \gg x_{\mathrm{L}}$, a chiral-JP with a strongly chirality intends to shuttle between the upper and lower boundaries, with a rather weak tendency of sliding along the boundaries. Obviously, this causes the weakening of the boundary flows, which eventually diminishes the net flow of the autonomous transport. For another situation, under the regime with $R_\Omega \ll x_{\mathrm{L}}$, the chiral radius is extremely short compared to the compartment size. In this case, the active particle does not strict to move along the boundaries once touching them, as shown by the PDF plots in Fig. 5.11(d). Instead, the chiral microswimmer tends to diffuse away from the boundaries. From the analysis above, the angular momentum employed by Ω

turns out to be inefficient in both R_Ω, which lead to the vanish of the autonomous transport of the chiral active particle. Obviously, we can conclude the rectification effect caused by chirality is insignificant when the chirality is rather weak $|\Omega|\tau_\Omega$.

For the further understanding, we study the dependence of rectification on the chirality Ω under several fixed thermal fluctuation level D_0, shown in Fig. 5.14. The result is in a good agreement with the former statement. In Fig. 5.14, the maximum values of the rectification function curves that η versus Ω can be regarded as a verification of the optimization behavior presented above. While the thermal noise level D_0 is decreasing, the position of the η peak shifts from the high frequency regime to lower regime, yet finally toward a limit value of chirality.
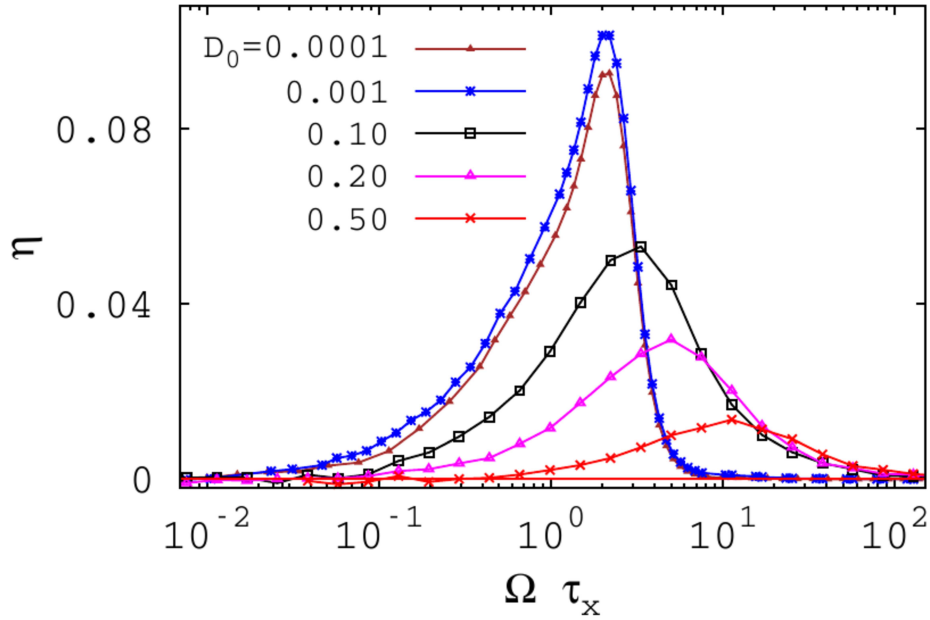
FIGURE 5.14: Optimization of the rectification as a function of Ω for chiral active transport, under the different thermal noise level. The channel parameters are set as $x_L = y_L = 1$, $\Delta = 0.12$, $\epsilon = 0.25$, $\phi = 0$. The other parameters are $v_0 = 1$, $D_\theta = 0.2$, $D_0 = 0.1$.

The Ω value of this limit position is considered to be significant, as this is the threshold value Ω_M mentioned. Note again that under

the chirality Ω_{M}, the active particles tend to swim in a circular orbit hardly being caught by the boundaries of the compartment, which makes the rectification transport optimized. Consider that the chirality Ω is slightly increasing, the radius of chiral orbit $R_\Omega = v_0/\Omega$ becomes smaller, thus the microswimmer moves more closely to the confined geometries. As a result, the active particles is more likely to be captured by the compartment, which can be applied to explain the rapid declination of η for $\Omega > \Omega_{\mathrm{M}}$.

As to the impact of D_0, it has already been discussed that the thermal noise can prompt the particle inside the compartment, thus the thermal noise turns out to play a role of agitating the boundary flows. For the active particle with chirality, the thermal noise can also disturb its circular trajectories and bring more tendency of center diffusion. Consequently, the peak position Ω_{M} shifts to the higher frequency regime as shown in Fig. 5.14, when D_0 is increasing. With such perturbation induced by the thermal noise, the threshold of the chiral radius turns out to be smaller correspondingly. What is more, the peak amplitude of the rectification power η declines and finally disappears as the D_0 increasing, which is predicted in Fig. 5.13.

5.4   Asymmetric channel geometries

Based on our former discussions in this section, the autonomous transport is, as a matter of fact, produced by the flows near to the boundaries. Therefore, the process of rectification transport is controlled and directed by the shape of the boundary confinement, or specifically speaking, the spatial symmetry of the channel walls.
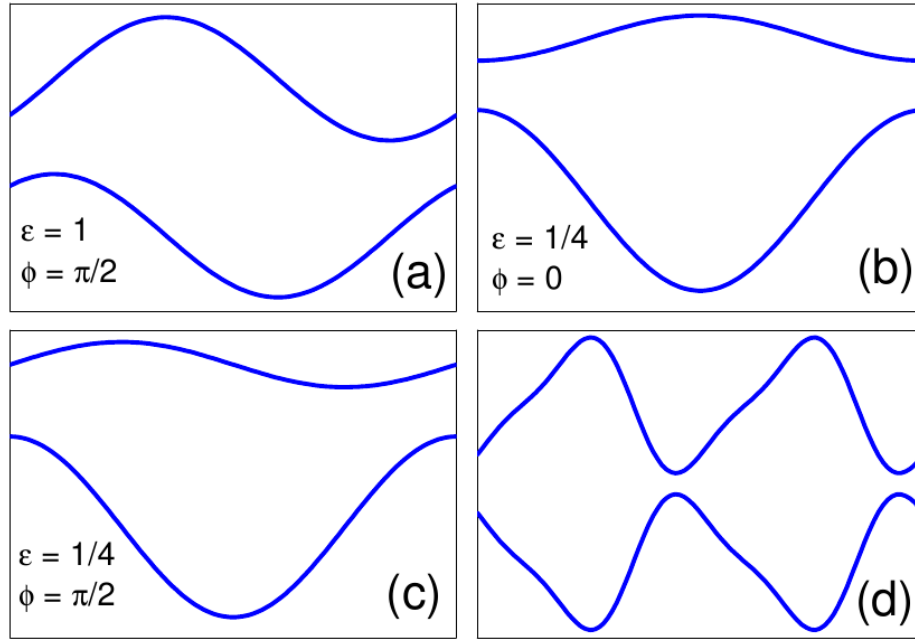
FIGURE 5.15: Corrugated channel geometries with different asymmetries. (a) centrosymmetric or supersymmetric; (b) left-right asymmetric; (c) upside-down asymmetric; (d) upside down symmetric. ϵ and ϕ are parameters introduced in Eq. 5.2.

Further statements can be pronounced from the aspect of the strict symmetry analysis theory [204].

Shown in Fig. 5.15, the 2D channel geometries can be classified into the following divisions:

- *Upside-down asymmetric channel.* This kind of channel is asymmetric under inversion of the y-axis ($y \to -y$), while possesses the symmetry under the inversion of x-axis, shown in Fig. 5.15(b).

- *Left-right asymmetric channel.* This kind of channel is asymmetric under inversion of the x-axis ($x \to -x$), while possesses the symmetry under the inversion of y-axis, shown in Fig. 5.15(d).

- *Centro- or supersymmetric channel.* This kind of channel is invariant under x- or y-axis inversions as shown in Fig. 5.15(a).

- *Asymmetric channel.* It includes the channels which are both left-right asymmetric and upside-down asymmetric as shown in Fig. 5.15(c).

Notice that the Langevin dynamics possess the symmetry properties in our model, it is proved to be interesting to combine the symmetry properties of Langevin dynamics and the compartment shape of channel. Due to the constrict resulted from the upper-lower boundaries, we only consider the invariant property of Langevin Eq. 4.1, which describes the movement in the transport direction. It turns out to be invariant under the transformations $x \rightarrow -x$ and $\theta \rightarrow \pi - \theta$ [202].

1. Consider the channel consisted with right-left symmetric while upside-down asymmetric compartments (b). As to the non-chiral active particles, obviously we conclude that $\bar{v}(\Omega = 0) = 0$, which indicates that the non-chiral particles cannot be rectified by right-left symmetric channel. For the chiral particles, under the transformation $\Omega \rightarrow -\Omega$, it can only causes the directions of the boundary flows reversed according to the invariant property of Eq.4.1. As a result, the mean velocity in x-direction should be the opposite, namely $\bar{v}(-\Omega) = -\bar{v}(\Omega)$.

2. Consider the channel consisted with upside-down symmetric while right-left asymmetric compartments (d). The non-chiral active particles can be rectified by the channel as proved in Fig. 5.3. Similarly with the case in channel (b), we conclude that for chiral particles $\bar{v}(-\Omega) = \bar{v}(\Omega)$, as the consequence of the

equivalent boundary current profile caused by the upside-down symmetric channel. This symmetry relation is supported by the flat branch of the η shown in Fig. 5.9, in which $\bar{v}$ can be explained by supposing $\bar{v}$ as a function of Ω^2.

3. With the comparison of Fig. 5.15(b) and (c), we can obtain (c) by shifting upper channel walls $w_+(x)$ in Eq. 5.2 by ϕ. For right-left symmetric channel, by shifting $w_+(x)$ to the opposite direction with the length $-\phi$, we can easily conclude an additional symmetry relation as $\bar{v}(\phi, \Omega) = \bar{v}(-\phi, \Omega)$ Similarly, for upside-down symmetric channel, this additional symmetry relation turns out to be $\bar{v}(\phi, \Omega) = \bar{v}(\phi, -\Omega)$. Nevertheless, the modulating function on $\bar{v}$ induced by the relative shift ϕ is weak, as we observe in Fig. 5.12.

4. For a centro-symmetric compartment (a), the invariant relations in both x- and y-directions suffice, which leads to $\bar{v}(\Omega) = 0$. We prove this statement by numerical simulation by setting $\epsilon = 1$ and any ϕ.

5. Concluded from point 1 and 2, the chirality $\Omega \neq 0$ is the precondition for the rectification effect of active particles in right-left symmetric channels, but not for the upside-down symmetric channel. We can extend this argument into more class of channels, i.e. (c) supported by the following reasoning. For simplicity, we first consider a passive Brownian particles by assuming $v_0 = 0$. With the Fick-Jacobs reduction technique [62], the normal diffusion in a smoothly and directed channel is dominated by a modulating function $\delta(x) = w_+(x) - w_-(x)$. Given that the boundaries $w_\pm(x)$ are sinusoidal function with period x_L, the difference of their $\delta(x)$ should be with the same period.

As a result, mirror symmetry exists in the suppressed dynamics in longitudinal direction. Based on this, we consider non-chiral active particles with self-propulsion mechanism, which is driven by an additional time-correlated noise. This colored noise indeed makes the diffusing break the time symmetry, but within the mirror symmetric channel, no thermal ratchet effect is expected. Thus, for the rectification power η, there is seldom contribution from the break of the right-left symmetry by shifting one of the wall.

5.5   Summary

In this chapter, we numerically investigate the autonomous transport of JPs in confined geometries, with different categories of asymmetry. Following the fact that the channel with triangular compartment possess the function of funneling non-chiral JPs to the easy-flow direction, according to our numerical results, the rectification power η monotonously depends on the self-propulsion length l_θ increasing. At the large limit of l_θ, the asymptotic value of η is reached. When the chirality taken into account, the rectification power rapidly drops zero when the chirality becomes stronger, with the self-persistent length fixed. The reason for this is that the radius of chiral orbit is highly suppressed when Ω is large, which results in constriction of the chiral JP circling within one compartment.

Later we investigate JPs diffusing in upside-down asymmetric channel, with an example of the sinusoidal channel with tunable height of upper boundary function. The requirement for non-zero net rectification flows is the chirality of JPs. For chiral JPs, the net flow is

detectable due to the upside-down asymmetry of the channel. The dependence of η on the fluctuation parameters D_0 and D_θ are investigated, respectively. It is concluded that the rectification flow much depends on the chirality, and the optimization can be achieved by choosing the proper Ω according to the profiles of rectification power.

Chapter 6

Diffusion of active particles in channels

Besides the autonomous transport that occurs in the asymmetric channels reported in Chap. 5, it is interesting and important to look into the spreading aspect of the JPs. To demonstrate such phenomenon from the experimental point of view, the dispersion of a Brownian particle in the free dimension of the channel can be regarded as a measure of the efficiency of the rectification in channels [205]. Technically, it can be measured over an affordable observation time even for a rather weak autonomous current. Indeed, this measurement is considered to be convincing and efficient only if the dispersion is adequately small.

When we focus on the investigation of active Brownian particles, the issue of dispersion is of overwhelming significance. As defined in the model including self-propulsion mechanism, the stochastic dynamics of JPs is distinguished by long correlation times, which is much different from that of classical Brownian dynamics. Thus, little current literatures on the passive Brownian diffusion can be used for pertinent references [95, 206].

In this section, we investigate the transport diffusivity of active micro-swimmers moving in channels with different geometries. We consider first the case of diffusion of non-chiral JPs, and then the chiral JPs. The results of the diffusivity in the bulk for the JPs without chirality can be solved analytically, and based on that we deduce the bulk diffusivity of chiral particles phenomenologically. In this chapter, the diffusivity in the bulk is denoted as D. To study the diffusion of the JPs in the channel, the channel diffusivity D_{ch} is introduced for the numerical observation and discussion, which is defined as the limit

$$D_{\text{ch}} = \lim_{t \to \infty} [\langle x^2(t) \rangle - \langle x(t) \rangle^2]/(2t). \tag{6.1}$$

6.1 Diffusion of non-chiral active particles

6.1.1 Analytical result of non-chiral JP diffusion in the bulk

First, we start with the bulk diffusion of the non-chiral JP. Indeed, there is seldom possibility to fully solve the Langevin Eqs. 4.1-4.3 analytically, even in the bulk. In spite of that, we can learn from the previous work presented in [196, 207] that

$$\langle \cos\theta(t)\cos\theta(0) \rangle = \langle \sin\theta(t)\sin\theta(0) \rangle = (1/2)e^{-tD_\theta}, \tag{6.2}$$

From this we can notice that the self-propulsion velocity elements in x- or y- direction are $v_{0,\text{x}}$ and $v_{0,\text{y}}$. Combined with Eq. 6.2, $v_{0,\text{x}}$ and $v_{0,\text{y}}$ can be regarded as the color noise defined as $\xi_{\text{s}}(t)$, with zero

mean value and finite-time correlation time as

$$\langle \xi_{s,i} \rangle \; = \; 0, \tag{6.3}$$

$$\langle \xi_{s,i} \xi_{s,j} \rangle \; = \; 2(D_s/\tau_\theta)\delta_{i,j}e^{-2t/\tau_\theta}. \tag{6.4}$$

Here $D_s = v_0^2 \tau_\theta/4$ and $\tau_\theta = 2/D_\theta$. Based on Fürth's Law [208], we obtain MSD of the non-chiral particle in the bulk as

$$\langle \Delta \vec{r}(t)^2 \rangle \; = \; 4(D_0 \; + \; v_0^2 \tau_\theta/4)t + (v_0^2 \tau_\theta^2/2)(e^{-2t/\tau_\theta} - 1), \tag{6.5}$$

in which $\Delta \vec{r}(t)$ is displacement from the initial position $\Delta \vec{r}(t) \equiv \vec{r}(t) - \vec{r}(0)$. When the diffusion time is considered to be long enough with $t \gg \tau_\theta$, MSD can be simplified by ignoring the exponential term in Eq. 6.5 and the asymptotic normal diffusion law can be reverted as

$$\langle \Delta x^2 \rangle \; = \; 2Dt. \tag{6.6}$$

Thus, the diffusivity of non-chiral particles can be obtained as

$$D \; = \; D_0 \; + \; D_s \; \equiv \; D_0 \; + \; v_0^2 \tau_\theta/4. \tag{6.7}$$

Apparently, the diffusion coefficient D here is composed two components with different functions: one is D_0, which is caused by the thermal fluctuations; the other is D_s, which is due to the self-propulsion mechanism with $D_s = v_0^2 \tau_\theta/4$.

6.1.2 Diffusion of non-chiral JPs in a sinusoidal channel

As presented in Sec. 4, the channel can play a significant function, like funneling, on diffusing of JPs because of its spatial constrictions.

Regarding the diffusion in a tube with the uniform width, such diffusion cannot be rectified and the diffusivity is proved to be the same as that in the bulk, see the dotted line in Fig. 6.1. In the absence of the self-propulsion function with $v_0 = 0$, the diffusivity turns out to be $D = D_0$.

Here we consider a sinusoidal channel defined in Sec. 5.3.1, in which the diffusion of the particles is obviously hindered by the spatial constrictions of the bottlenecks. Particularly, the boundary shape function is

$$w_\pm(x) = \pm\frac{1}{2}\left[\Delta + (y_\mathrm{L} - \Delta)\sin^2\left(\frac{\pi}{x_\mathrm{L}}x\right)\right], \qquad (6.8)$$

with Δ as the width of the bottleneck, x_L as the compartment length and y_L as the maximum height of the compartment. As shown in Fig. 6.1, if the self-propulsion mechanism is absence $v_0 = 0$, the channel diffusivity D_ch is assumingly proportional to D_0, which can be written as $D_\mathrm{ch} = \kappa_0 D_0$. The suppression parameter κ_0 is well studied in previous works for the traditional Brownian particles [69, 207], which is proved to be the function of Δ and D_0. In the limit of strong self-propulsion velocity $v_0 \to \infty$, the self-propulsion mechanism becomes a dominating role of the diffusion process, with $D \simeq D_\mathrm{s}$. Accordingly, we introduce a similar parameter of such suppression function κ_s for self-propulsion diffusivity, namely $D_\mathrm{ch} = \kappa_\mathrm{s} D_\mathrm{s}$.

Combining the evaluation under the two limits, the channel diffusivity can be accordingly rewritten as

$$D_\mathrm{ch} = \kappa_0 D_0 + \kappa_\mathrm{s} D_\mathrm{s} \qquad (6.9)$$

In Fig. 6.2, both asymptotic regimes are illustrated under different D_θ and Δ, It can be clearly observed that κ_s is much less sensitive
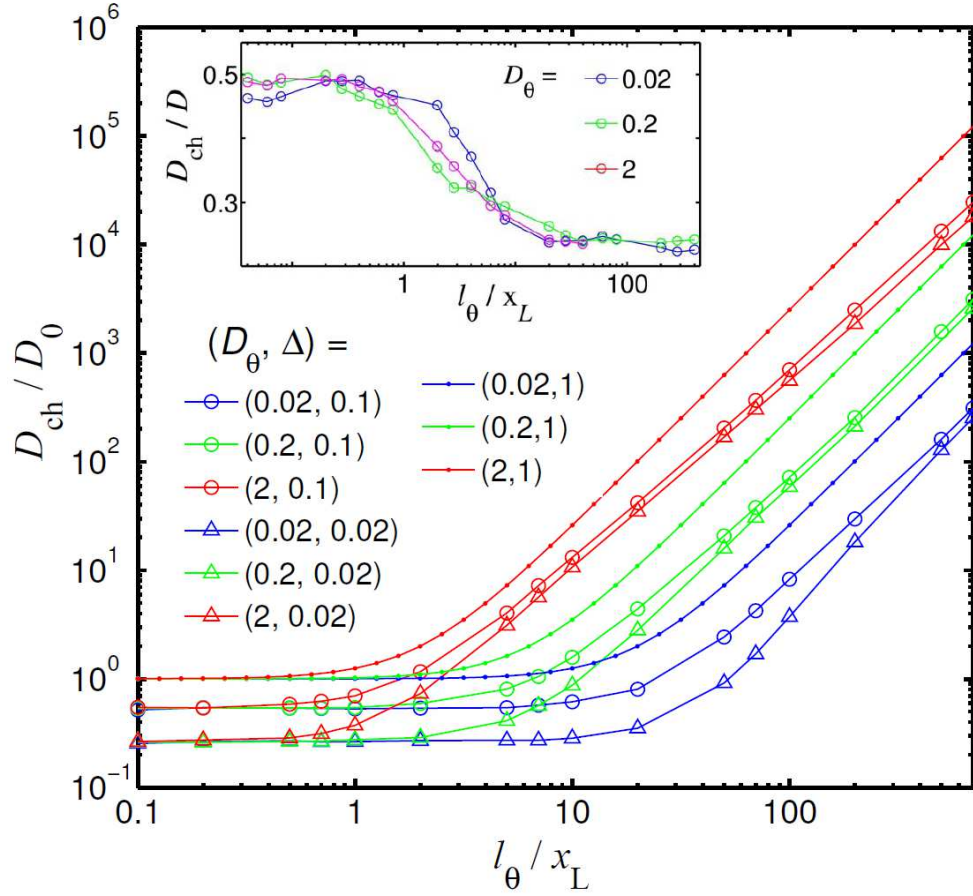
FIGURE 6.1: Diffusivity of non-chiral JPs in a sinusoidal channel, with the boundary functions given in Eq. 6.8. The profile of D_{ch}/D_0 *vs.* l_θ is shown for different D_θ and Δ. The inset graph shows the curve of D_{ch}/D *vs.* l_θ for different D_θ with $\Delta = 0.1$. The other parameters are $x_L = y_L = 1$, $D_0 = 0.01$.

to the bottleneck width compared to κ_0. Apparently, both κ_0 and κ_s are less than one and possess little dependence on D_θ, shown in Fig. 6.2.

It should be remarked that there are different mechanisms underlying the two kinds of suppression of channel diffusion, which are characterized by parameters κ_0 and κ_s respectively.

- *For κ_0*

  For the limit of weak self-propulsion mechanism, JPs behave in a manner which is closed to a traditional unbiased Brownian particle with $v_0 = 0$. As to the constricted diffusion of
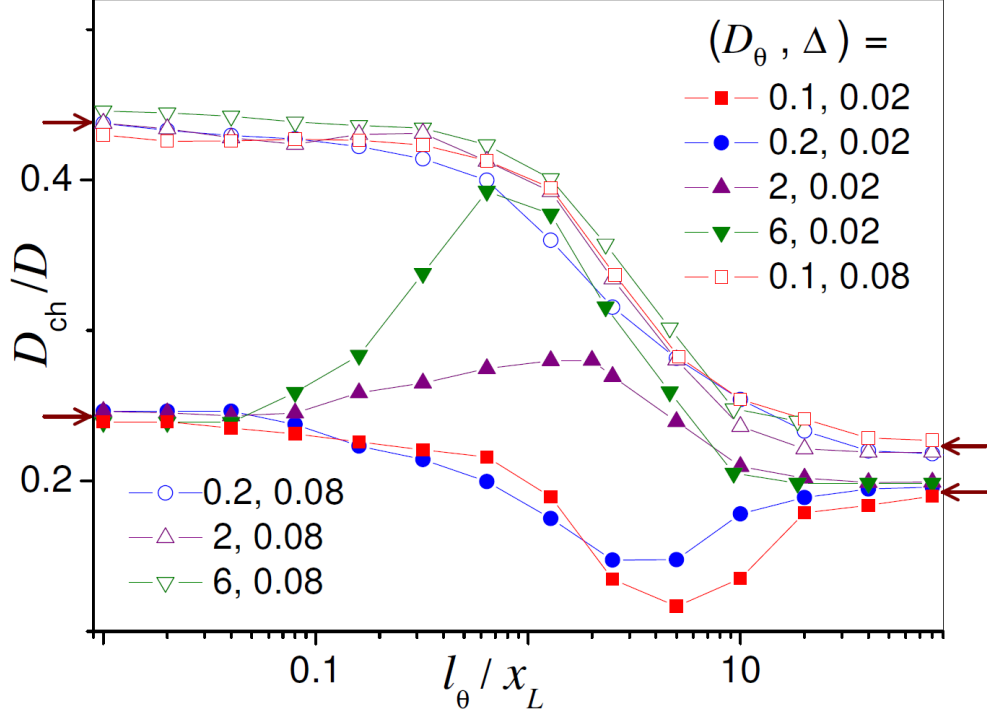
FIGURE 6.2: Diffusivity of non-chiral JPs in a sinusoidal channel, under the different D_θ and Δ. D is the bulk diffusivity of the channeled JP. The other parameters are $D_0 = 0.05$, $x_L = y_L = 1$. The left and right arrows represent the estimated values of the suppression constants κ_0 and κ_s respectively. Here for $\Delta = 0.02$, $\kappa_0 = 0.25$ and $\kappa_s = 0.2$; for $\Delta = 0.08$, $\kappa_0 = 0.45$ and $\kappa_s = 0.23$.

the passive Brownian particle, the situations should be considered respectively according to the shape of the compartment. For smoothly corrugated channels, κ_0 can be obtained approximately by FJ approach [69, 95]. For the channels with sharply septate compartments, the mean-first-exit time formalism can be applied [209, 210]. Due to the fact that the particle diffusion mostly occurs in the inner area away from the walls, it is concluded that κ_0 is strongly influenced by the volume of the compartment, the bottleneck width and thermal noise level.

- *For κ_s*

Under the limit of strong self-propulsion mechanism, the persistent length for a non-chiral particle is far beyond the compartment dimension $l_\theta \gg x_L$ or y_L. In this case, the suppression

constant $\kappa_{\rm s}$ is strongly determined by the boundary geometry and the boundary condition we adopted for simulating the collisions between the particles and the walls. For sliding boundary condition described in Chap. 4, JPs tend to stack to the boundaries, thus the probability current is adjusted by the boundary profile $w_\pm(x)$ [203]. Interestingly, the diffusion is not sensitive to the bottleneck width Δ under the assumption of zero-size particle as shown in Fig. 6.2.

6.1.3 Diffusion of non-chiral JPs in a triangular channel

Here, we observe the diffusion of non-chiral particles in channels with different compartment geometries, i.e. triangular compartment illustrated in Figs. 5.1,5.2,5.4. According to our results, it is concluded that this picture analyzed does not depend much on the actual compartment geometry. The diffusivity of the non-chiral particles in the channel with triangular compartment is calculated and the results are plotted in the inset figure of Fig. 6.6.

Similar to the limit of small self-propulsion velocity, it is shown in this figure that $D \to D_0$ under the limit of short self-propulsion time $\tau_\theta \ll \tau_{\rm x}$. As a consistent understanding, it has been discussed in Sec. 5 that the rectification power η decays to zero when $\tau_\theta \to 0$ shown in Fig. 5.3. Indeed, this limit makes the active Brownian motion fall back to traditional unbiased Brownian motion in the channel with triangular compartments, with $D_{\rm ch} = \kappa_0 D_0$. As mentioned before, κ_0 is confirmed to be a function of the confined geometry, which can be estimated by simulation, e.g. $\kappa_0 \simeq 0.55$ in this compartment settings. As to the other limit of long self-propulsion time $\tau_\theta \gg \tau_{\rm x}$ while η

reaches it horizontal asymptotic value in Fig. 5.3, the suppression parameter of self-propulsion diffusion D_s is estimated as $\kappa_s \simeq 0.16$.

From a phenomenological point of view, we are able to work out the value of κ_s by approximation. In a good agreement with the evaluation of the active diffusion in the bulk $D_s = v_0^2 \tau_\theta / 4$, we can suppose that an JP propels itself to the right and left in the channel alternatively, with time constant $\tau_\theta / 2$. Obviously, due to the constrict of the confinement, the JP can be considered diffusing with the effective self-propulsion velocities to the right or left respectively. Here we introduce mobility constants μ_R and μ_L for right and left velocity, on which the compartment geometry plays a dominant role.

Thus, the rectification power η can be rewritten as

$$\eta = |\mu_R - \mu_L|/2, \tag{6.10}$$

and the corresponding channel diffusivity is calculated as [209, 210]

$$D_{ch} = (\mu_R + \mu_L)^2/2. \tag{6.11}$$

Consider the limit of the weak thermal noise $D_0 \to 0$, the approximations $\mu_L = 0$ and $\mu_R = \cos^2\alpha/\sqrt{2}$ can be applied for the channel with triangular compartments. According to this evaluation method, we obtain the approximated value for the rectification power at zero noise level $\eta^{(0)} = 0.28$ and the suppression parameter $\kappa_s = D_{ch}/D_0 = 0.16$, which are in a good agreement with the asymptotic value shown in Figs. 5.5, 6.6. For $D_0 > 0$, the thermal noise turns out to inhibit the rectification power $\eta < \eta^{(0)}$ as we discussed in Chapter 5. Interestingly, the thermal fluctuations tends

to enhance the diffusivity in channel $D_{\text{ch}} > D_{\text{ch}}^{(0)}$ according to the simulation results.

6.2 Diffusion of chiral active particles

6.2.1 Diffusion of chiral JPs in the bulk

Analytical solution in the phenomenological law

In the last section, we analytically calculate the diffusivity of non-chiral JP in the bulk as given by Eq. 6.7, from which we can conclude that there are two distinctive contributions for the active diffusivity, namely $D = D_0 + D_{\text{s}}$. To calculate the bulk diffusivity of chiral particles with $\Omega \neq 0$ as a more appealing task, we extend the analytical result of the chiral particle diffusivity in the bulk, and the prediction in the phenomenological law is given as follows

$$D(\Omega) \;=\; D_0 \;+\; \frac{D_{\text{s}}}{1 + (\Omega \tau_\theta / 2)^2}. \tag{6.12}$$

We notice that $D(\Omega = 0) = D_0 + D_{\text{s}}$, which matches with Eq. 6.7. Here, we summarize the hints of the derivation of Eq. 6.12 as follows:

- As the separation between thermal and self-propulsion diffusion, we concentrate on the limit case with zero thermal noise D_0 for the convenience.

- According to the identities in Eq. 6.2, it can be concluded that the velocity components x_{L} and y_{L} can be considered as two independent non-Gaussian noise $\xi_{\text{x}}(t)$ and $\xi_{\text{y}}(t)$ with zero-mean and exponential auto-correlation as the calculation in Eqs. 6.3,6.4. The intensity is D_{s} and the correlation time is τ_θ.

- Finally, while setting the thermal Gaussian noise term as zero, $\xi_x = \xi_y = 0$, we carry out the time derivative of Langevin Eqs. 4.1,4.2, and after linearization we obtain the dynamics of chiral particles as

$$\ddot{x} = -\Omega\dot{y} - 2\dot{x}/\tau_\theta + 2\chi_x(t)/\tau_\theta, \qquad (6.13)$$

$$\ddot{y} = +\Omega\dot{x} - 2\dot{y}/\tau_\theta + 2\chi_y(t)/\tau_\theta. \qquad (6.14)$$

  In Eqs. 6.13,6.14, χ_x and χ_y represent the white Gaussian noise with zero mean and intensity D_s.

- We can predict the bulk diffusivity of the chiral particle from the approximate Langevin dynamics of Eqs. 6.13,6.14, as the result shown in Eq. 6.12.

Numerical verification: Diffusivity of JPs in a straight tube

In a straight channel with $w_\pm(x) = \pm y_L/2$, that is, a tube, the bulk and channel diffusivity should be calculated as the result due to the sliding boundary condition applied here. We confirm this conclusion by the comparison between simulation of tube diffusion and analytical solution of bulk diffusion displayed in Fig. 6.3. Simulation of the active diffusion in tubes with different width y_L are compared, and it is observed that the tube diffusivity does not dependent on the channel width. Shown in Fig. 6.3, the numerical results are in a good agreement with the analytical result predicted by the phenomenological law of Eq. 6.12. At $\Omega = 0$, $D(\Omega)$ represents the diffusivity of a non-chiral JP, and for $\Omega \to \infty$ the active diffusivity is equal to the thermal diffusivity D_0. Under this limit of strong chirality, the chiral radius is extremely small with R_Ω/l_θ, thus the self-propulsion function is entirely suppressed [211].
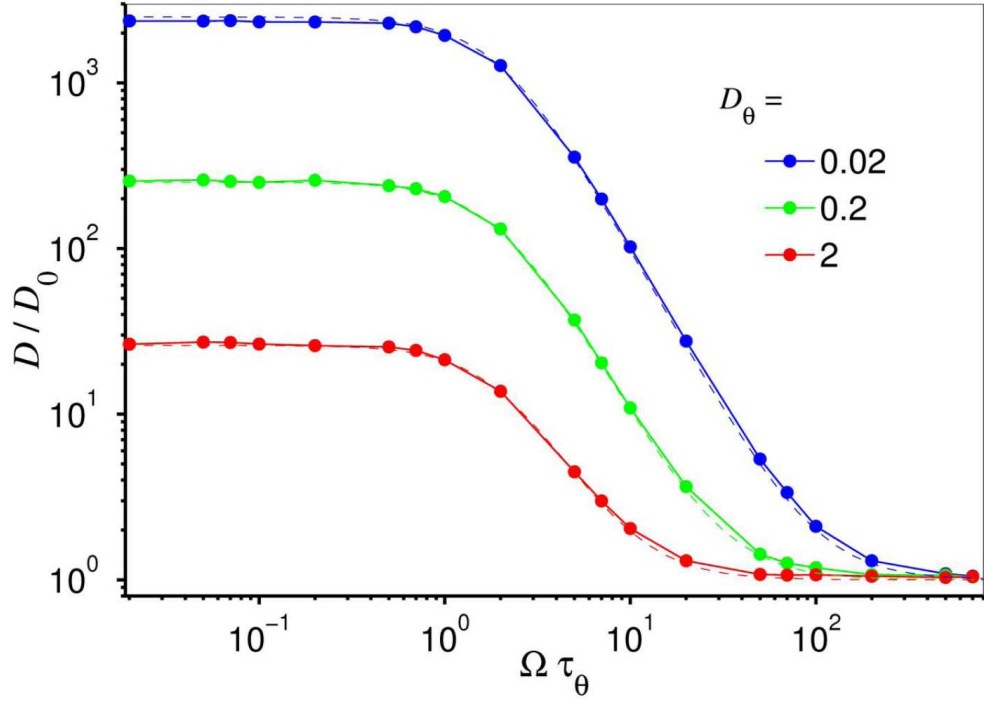
FIGURE 6.3: Diffusivity of chiral JPs in a straight tube, with $\Omega > 0$ and $v_0 = 1$. It shows the profile of D_{ch} *vs.* Ω for different D_θ with $D_0 = 0.01$. The boundary function is given as Eq. 6.8 with $\Delta = y_{\mathrm{L}} = 1$. The dashed lines represent the corresponding phenomenological law given by Eq. 6.12 with $D_{\mathrm{ch}} = D$ for a straight tube. More simulation results prove that the diffusivity is independent on the sign of Ω and the width of the tube.

6.2.2 Diffusion of chiral JPs in a sinusoidal channel

With these prerequisites above, the parameter dependence of the active diffusion of chiral JPs in the corrugated boundaries, i.e. sinusoidal channel is discussed as a further observation, shown in our submitted paper as Ref. [211]. Reported in Fig. 6.4, the dependence of D_{ch} on the self-propulsion mechanism parameters τ_θ is numerically studied under several fixed chirality levels. With the inspection on the figure, we can conclude immediately that for large τ_θ, the thermal noise level D_0 can be ignored under the large limit of self-propulsion time τ_θ. In this case, $D_{\mathrm{ch}} \sim \kappa_{\mathrm{s}} D(\Omega)$, which is similar to non-chiral particles. Interestingly, we notice that the suppression

constant κ_s does not sensibly depend on Ω, which is not in an extremely high level. We can observe that while τ_θ is increasing under fixed chirality, the channel diffusivity D_{ch} goes up to its maximum , that is, $D_{ch}^{max} \simeq \kappa_s D_s/2$. It can be also found that the locates of the peak satisfied $|\Omega|\tau_\theta = 2$, which can be considered insensitive to the channel geometry. What is remarkable, for the D_{ch} curve with the maximal positions locating at $\tau_\theta > \tau_x$, the D_{ch} values can be well estimated by the result of bulk diffusivity as a function of τ_θ shown in Eq. 6.12, combined with the relation $D_{ch} = \kappa_s D$.

Seen from the comparison of different chirality levels, for the finite Ω which is not extremely large, the suppression of active diffusivity due to the channel occurs both for $\tau_\theta \to 0$ and $\tau_\theta \to \infty$. As a result, we can make the prediction that $D_{ch}(\Omega) \to \kappa_0 D_0$, in which κ_0 is the suppression constant obtained in the results shown in Fig. 6.2. When Ω is relatively small, that is, in a low level chirality, the convergence towards the asymptote in large τ_θ regime is rather slow.

The dependence of D_{ch} on Ω at constant D_θ is studied and illustrated in Fig. 6.5. Consistent with the asymptote shown in Fig. 6.4, the same asymptote approached by the large tails of the curves D_{ch}. While the Ω increasing from a very low level, it is explicitly shown in Fig. 6.5 that D_{ch} retains in the initial level. When Ω reaches the regime satisfied $|\Omega|\tau_\theta \geq 2$, D_{ch} starts decreasing, with the maximal values in a good agreement with that displayed in Fig. 6.5. It is noticeable that small diffusivity peaks appears in the regime with $|\Omega|\tau_\theta \gg 1$. These peaks locates around a certain value of Ω namely Ω_M, and they have nearly no relevance on the self-propulsion time τ_θ. Here, the peaks location Ω_M can be approximated by regarding the chiral radius $R_\Omega = v_0/|\Omega|$ decreases on Ω increasing, thus the JP

FIGURE 6.4: Diffusivity of chiral JP in a sinusoidal channel in the function of τ_θ for different Ω. The parameters are $v_0 = 1$, $D_0 = 0.05$, $\Delta = 0.08$, $x_L = y_L = 1$. The dashed line denotes the asymptotic linear power-law of Eq. 6.12.

turns out to play a circular-like movement inside a certain compartment, without touching the boundaries. More details can be referred to Ref. [145], that the trajectory is actually a logarithmic spiral with exponentially small steps. Considering the zero-noise limit, we can estimate Ω_M from $2R_\Omega \simeq x_L$, that $\Omega_M \simeq 2v_0/x_L$. This estimation is proved to be in a close agreement with the data displayed in Fig. 6.5.

According to Brownian transport theory, the motivation of creating a trapping mechanism generally relies on the excess peak in the diffusivity profile [183, 212]. Thus, the small peak mentioned above can be regarded as the foundation of the trapping dynamics. This statement requires the condition that $\Omega_M \tau_\theta \gg 1$, as the self-propulsion time is ensured to be sufficiently long.
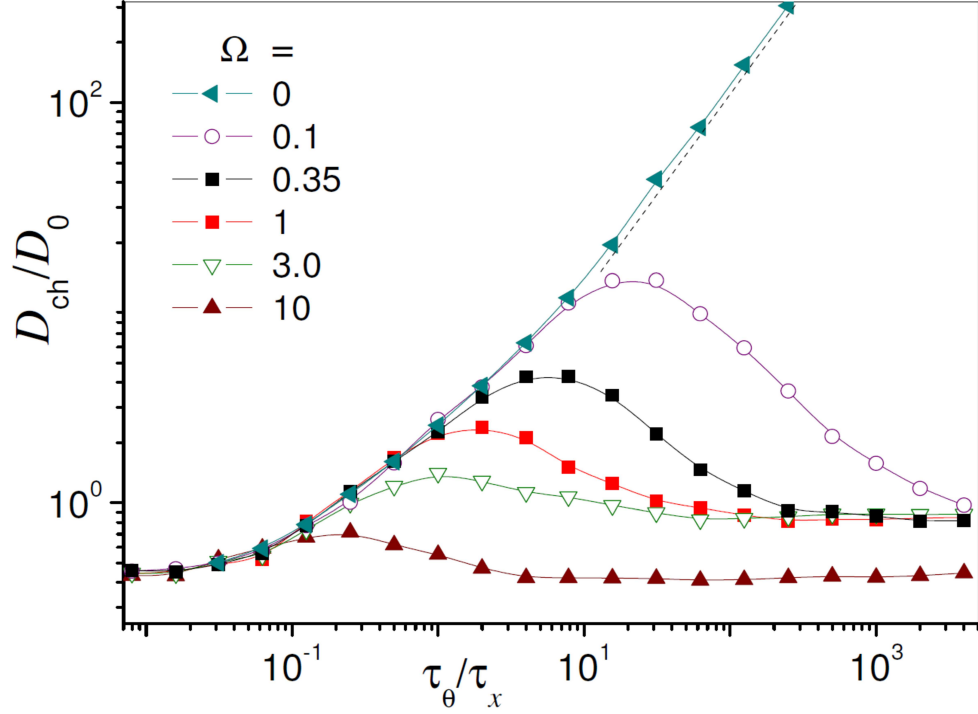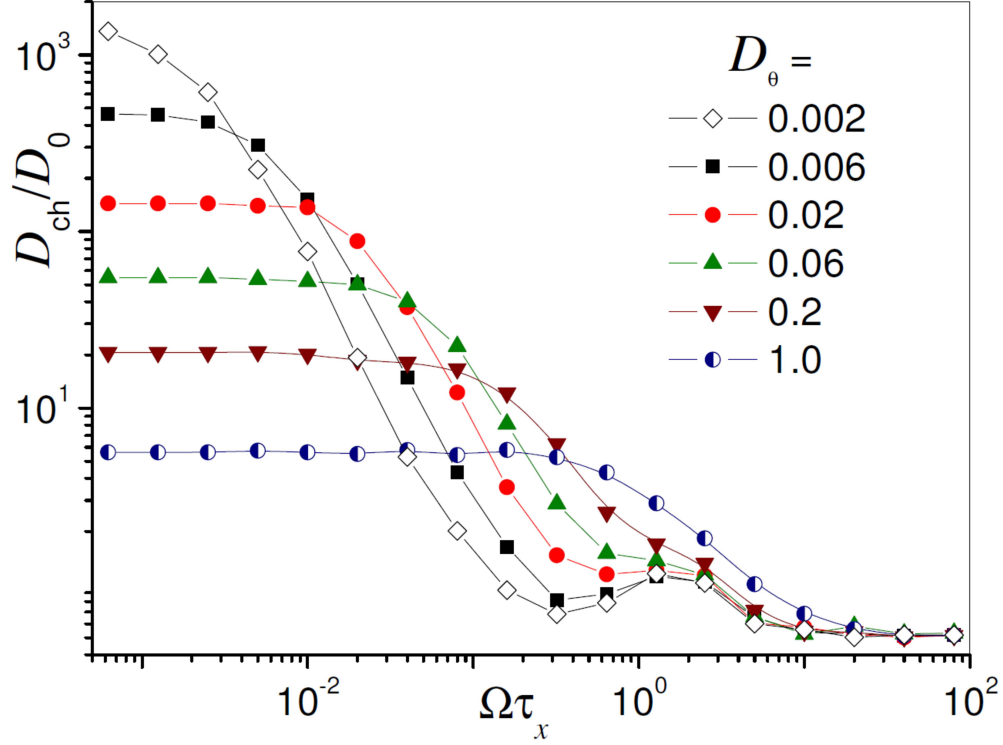
FIGURE 6.5: Diffusivity of chiral JP in a sinusoidal channel in the function of Ω for different D_θ. The parameters are $v_0 = 1$, $D_0 = 0.05$, $\Delta = 0.08$, $x_L = y_L = 1$.

6.2.3 Diffusion of chiral JPs in a triangular channel

Here we numerically investigate the diffusivity of chiral JPs in the channel with triangular compartment illustrated in Fig. 5.7. The dependence of D_{ch} on the Ω with constant τ_θ is displayed in Fig. 6.6, and we can conclude that the curves turn out to be similar with channel chirality for the case in the sinusoidal channel, and in a close agreement with the above interpretations.

Specifically, we can learn from the data sets shown in Fig. 6.6 as follows. Firstly, in the weak chirality regime with $|\Omega|\tau_\theta \ll 1$, the channel diffusivity D_{ch} does no depend on Ω, which is consistent with the result in the profile of rectification power η displayed in Fig. 5.9. Secondly, similar to the diffusivity profile in sinusoidal channel, D_{ch} begins declining with Ω increasing to the regime $|\Omega|\tau_\theta \geq 2$, which

is coincide with the maxima of η shown in the inset figure of Fig. 5.9. Thirdly, in the strong chirality regime with $|\Omega|\tau_\theta \gg 1$, we can observe from the profile that $D(\Omega) \to D_0$, thus $D_{\mathrm{ch}} \simeq \kappa_0 D_0$ with the suppression constant here $\kappa_0 \simeq 0.55$. Finally, in the regime $\Omega\tau_\theta \gg 1$, slight peaks in the diffusivity curves merge as our expectation. The peaks occur when $R_\Omega = v_0/\Omega < x_{\mathrm{L}}$, with the positions represented by Ω_{M}. This is also consistent with the sudden drop in the profile of η shown in Fig. 5.9.
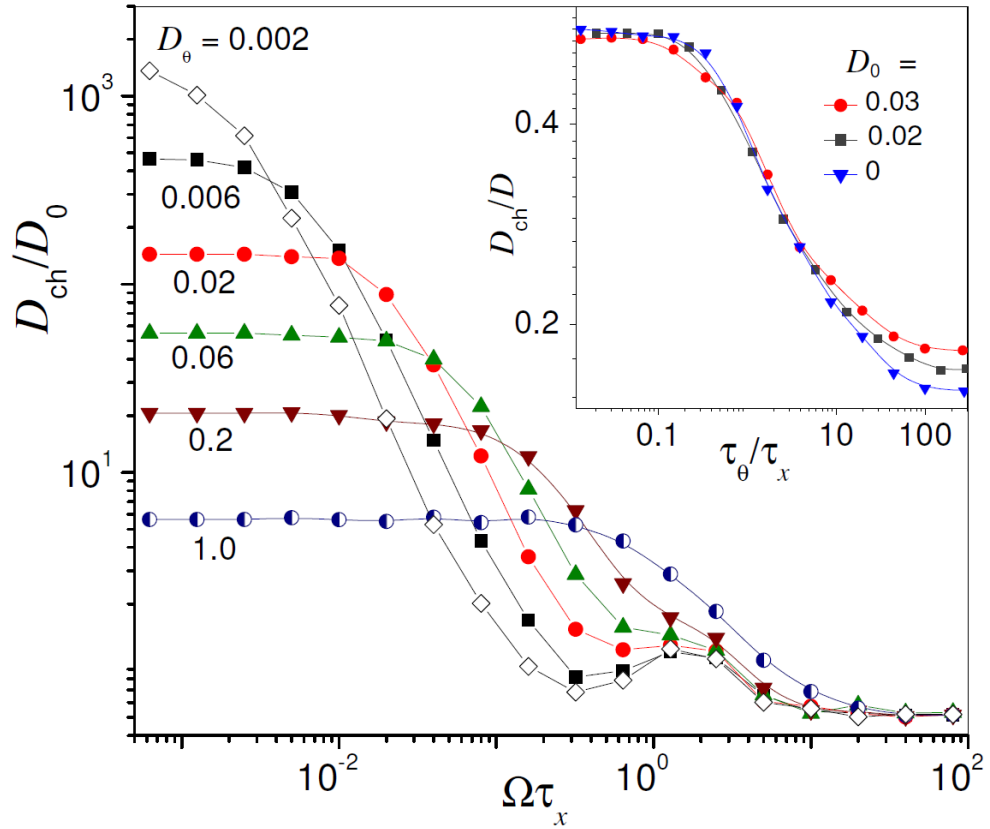

FIGURE 6.6: Diffusivity of chiral JP in a triangular channel in the function of Ω for different D_θ. The parameters are $v_0 = 1$, $D_0 = 0.03$, $\Delta = 0.08$, $x_{\mathrm{L}} = y_{\mathrm{L}} = 1$. The inset graph shows the profile of D_{ch} vs. τ_θ for different D_0 for non-chiral JPs with $\Omega = 0$.

6.3 Summary

In this chapter, we focus on the diffusivity of the non-chiral and chiral JPs in geometries. For chiral JPs in a straight tube, it is found that the diffusivity profile turns out to be the same with the bulk diffusivity, with no regard of the sigh of Ω and the channel width. When we consider the diffusion in corrugated channels, the confined diffusivity is constricted by the bottleneck within the channel, which is proved by our simulation results. We perform the Langevin simulation for sinusoidal and triangular channels, and it turns out that the diffusivity function does not much rely on the detail shape of the channel compartment. For non-chiral JPs diffusing in a sinusoidal channel, we find that when the self-propulsion length is much smaller than the compartment dimension, the diffusivity function strongly depends on the pore width. While the self-propulsion length increasing, this dependence turns out to become weaker. For the case of channeled chiral JPs, the channel diffusivity of a chiral JP is depressed due to the chirality compared with non-chiral JPs. The diffusivity profile of D_{ch} vs. τ_θ and Ω are obtained numerically, from which two mechanisms for the chirality-induced suppression are concluded, with the reason of $R_\Omega \ll l_\theta$ and $R_\Omega \ll x_{\mathrm{L}}$ respectively. In conclusion, the diffusivity function of the channeled active diffusion strongly depends on the self-propulsion and chirality of the particle, and the channel geometry as well.

Chapter 7

Conclusions and Outlook

Under the current interests of artificial active particles diffusing in the microscopic geometries, we numerically study the transport and diffusion of Janus micro-swimmers along a narrow periodically corrugated channel. With the motivation of the recent experimental development of the active particles with or without chirality, we introduce the Langevin approach to describe 2D model of the bulk diffusion of active particles proposed in Ref. [157]. Regarding the extreme difficulty of analytically solving the FJ equations of active diffusion in confinement [62], in this thesis we investigate the confined active transport numerically. We transfer the Langevin equations into finite difference equations, and introduce the algorithm of sliding boundary condition for the investigation of confined active diffusion (see Chap. 4). For the purpose of quantitative characterization, we define two key transport quantifiers: *the rectification power* η and *channel diffusivity* D_{ch} at the steady state. The simulation results and analysis of the autonomous transport and diffusivity are displayed in Chap. 5 and 6 respectively, which are mainly from the author's recently published paper [202].

As the first part of our study referred to Chap. 5, we focus on the autonomous transport induced by confined geometries with different kinds of asymmetry, in the main categories of left-right asymmetric and upside-down asymmetric channel. The channel with triangular compartment, as one example of left-right asymmetric channel, tends to funnel non-chiral JPs to the easy-flow direction [196]. For a non-chiral JP in a triangular channel, the rectification power η is significantly impacted by the self-propulsion length $l_\theta = v_0 \tau_\theta$. Shown in the numerical results, η monotonously goes up with l_θ increasing until the asymptotic upper bound is reached, when l_θ is much larger than the compartment dimension. For a chiral JP in a triangular channel, it is interesting to find that the rectification power dramatically gets lower and drops to zero for the chirality Ω becomes stronger, with the other self-propulsion parameters fixed. It can be explained that under strong enough chirality Ω, the radius of chiral orbit $R_\Omega = v_0/|\Omega|$ is so small that the chiral JPs are confined inside a certain compartment making circles rather than transport to other compartments.

For the investigation of JPs in upside-down asymmetric channels, we introduce the sinusoidal channel with tunable height of upper boundary function. For non-chiral JPs, there is no net autonomous flows. For chiral JPs, the particle flow at the upper and lower boundaries are oriented to opposite directions, and a net flow is thus detectable due to the upside-down asymmetry of the channel. The dependence of η on the translational and rotational diffusion coefficient D_0 and D_θ are investigated, respectively. We find different dependencies for weak and strong chirality regimes and the rectification power finally decay to zero when the thermal noise D_0 is extremely large. It turns out that the rectification flow vanish under the limit $\Omega \to 0$, which is

close to the case of non-chiral JP. η also drops to zero under the limit of $\Omega \to \infty$, for the moving circles are extremely suppressed which makes the transport vanish. While the rectification power does not monotonously depend on Ω, the optimized Ω for rectification power is obtained under the different thermal fluctuation levels.

In Chap. 6, we investigate and calculate the diffusivity of the non-chiral and chiral active JPs in confined geometries. According to our numerical results, we find that the diffusivity of chiral JPs in a straight channel is identical to the bulk diffusivity, which is independent of the width of the straight channel. When constricted by a corrugated channel, the diffusivity of non-chiral and chiral JPs are suppressed by the pores. Supported by our simulation of diffusion in channels with different compartment geometries, the general picture of the diffusivity function does not depend much on the actual shape of compartment. With the simulation results of non-chiral JPs diffusing in a sinusoidal channel which we take for an example of corrugated channel, we conclude that the dependence of the diffusivity on the pore width becomes weaker, with the increasing self-propulsion length. Compared with non-chiral JPs, the channel diffusivity of a chiral JP is depressed due to the chirality, when the chiral radius is smaller than the self-propulsion length or the compartment dimension.

In conclusion, the characterization functions of the confined active diffusion such as the rectification power and diffusivity strongly depend on the self-propulsion mechanism and chirality of the JP, as well as the channel geometry. This simplified model so-far discussed in this thesis can be considered as a stepping stone for more challenging generalizations. Specifically, discussions of parameter-dependence

here can be a useful reference for the real applications of control techniques, which can be approached with current experimental technology. Many microfluidic circuits with specialized functions can be designed and realized, such as the device with the function of guidance the chiral micro-swimmers to a designated target. With the same technique, monodisperse chiral micro-swimmers can be fabricated, which is still a challenging task with the respect of current development of technology. Furthermore, chiral "shuttles" along a specific corrugated channel can be realized in the absence of any external fields, utilizing the active swimmers binding to a load with the capability of inverting chirality.

In the next stage of study of diffusion of active JPs, we can address the following issues:

1. Diffusion gradients. We can take the local inhomogeneities generated for self-propulsion mechanism into account, thus the constant D_{ch} should be x-dependent as $D_{\mathrm{ch}}(x)$ combined with the channel profile bringing in the ratchet effect;

2. Hydrodynamic effects. In this thesis the movement of surrounding fluid near the JP is ignored, and the particle is considered as zero-sized. We can include the impact of the microfluid on the particle by analyzing the boundary flow around the finite-sized particle, by which a more accurate solution can be obtained when treating a finite-sized particle diffusing through a narrow pore of a corrugated channel;

3. Particle-particle interaction. When the particles are in high concentration, the interaction between the particles cannot be ignored. By modeling the inter-particle interaction, the phase

separation and transition phenomenon can be studied, which is significant and hopefully to be compared with the experiments.

4. Wall interactions. When the finite radius particle passing through a narrow confinement such as the channel with pores, the diffusion can be rather sensitive to the particle-wall interactions. By considering these interactions, the active rectification and diffusivity function can be further revised which will be more close to the experimental realizations.

Appendix A

Code in CUDA for the simulation of active BM

The code for the simulation for active BM in the upside-down asymmetric channel is given, which is consisted of a main file and an included header file named *header_Janus.cu* followed. The executable program can be obtained after compiling with the command *nvcc*.

The main file

```
#include <stdio.h>
#include <math.h>
#include <stdlib.h>
#include <cuda.h>
#include <time.h>
#include <float.h>
#include "header_Janus.cu"



int main(int argc, char *argv[])  // the main function
{
    int    iT = 0,std = 0,particle_NNAN,h_N_t_all=0;
    time_t start_time, end_time, moment1;
```

```
    time_t moment2,moment3,moment4,moment5;
    float  mvel[Nmvel],dif[Nmvel],m_vel,err_vel,dif_3,err_dif_3,relax_time;
    FILE  *fpvd;
    char  fnvd[200];


    //////// 1) list the input sequence
    device_no = atof(argv[1]);
   //// choose one of the graphic card
    h_Vph = atof(argv[2]);
    //// phoretic velocity (self-propulsion velocity)
    h_Dr = atof(argv[3]);
    //// rotational diffusion coefficient
    h_Dt = atof(argv[4]);
    //// translational diffusion coefficient
    h_Torque = atof(argv[5]);
    //// torque for chiral particle
    h_Y = atof(argv[6]);
    //// the maximum height of the sinusoidal channel compartment
    h_delta = atof(argv[7]);
    //// the pore width of the sinusoidal channel compartment
    h_eps = atof(argv[8]);
   //// quantisizing the upside-down asymmetry
    h_psi = atof(argv[9]);
   //// the shift between the upper and lower boundary



    //////// 2) create a text file for recording the result
    sprintf(fnvd,"./JANUS_diffusivity.dat");
    fpvd=fopen(fnvd,"w");
    time(&start_time);
    printf("Start from %s\n",asctime(gmtime(&start_time)));



    //////// 3) initialize the CUDA_memory, RNG_seed and parameters
    initialize_CUDA_ME();
    time(&moment1);
    printf("Initialization is over at %s\n",asctime(gmtime(&moment1)));
```

```
//////// 4) initialization for simulation
////////// time step should be small enouth
if (h_Vph >= 100.0)h_dt = dt_cons/h_Vph*100.0;
else h_dt = dt_cons;
//h_dt = dt_cons;
relax_time = relax_time_func(h_Vph);
initial_condition<<< blocksPerGrid, threadsPerBlock>>> (d_NL_x\
    ,d_cell_x,d_y,d_fi,d_t,d_RNG_seed);
cudaMemcpy (&h_x0,&d_cell_x,particle_memsize,cudaMemcpyDeviceToHost);
time(&moment2);
printf("Initial contidions have been set at %s\n"\
        ,asctime(gmtime(&moment2)));



//////// 5) launch the kernel function in device
time(&moment3);
printf("Launching the kernel from %s\n"\
        ,asctime(gmtime(&moment3)));
std = 0;        // std =0 means non-steady-state
m_vel = 0.0;
while (std == 0 ) ///// continue with dynamics if not steady-state
{
        iT = (iT + 1) % Nmvel;
evolve_ME <<< blocksPerGrid, threadsPerBlock >>> (d_NL_x\
                ,d_cell_x,d_y ,d_fi,d_t,d_RNG_seed,h_dt);
time(&moment4);
printf ("Dynamics have been done till %s\n"\
                ,asctime(gmtime(&moment4)));
printf ("particle memsize = %d\n", particle_memsize);

/////////////////// copy_results_from_Device_to_Host
cudaMemcpy (h_y,d_y,particle_memsize,cudaMemcpyDeviceToHost);
cudaMemcpy (h_NL_x,d_NL_x,particle*sizeof(int),cudaMemcpyDeviceToHost);
cudaMemcpy (h_cell_x,d_cell_x,particle_memsize,cudaMemcpyDeviceToHost);
cudaMemcpy (h_fi,d_fi,particle_memsize,cudaMemcpyDeviceToHost);

h_N_t_all = h_N_t_all + 1;
time (&moment5);
printf("Results have been passed to host at %s\n\n" \
```

```
                      ,asctime(gmtime(&moment5)));


/////////////////////  test whether it's in steady state
mvel [iT]= 0.0;
dif [iT] = 0.0;
particle_NNAN = 0;
if (h_N_t_all <= 1 + 0.1 && h_N_t_all> 1)
{
     for (int k =0; k < particle; k++) h_x0[k] = h_NL_x[k]*h_L + h_cell_x[k];
}
for (int k = 0; k < particle; k++)
{
      if (isFiniteNumber(h_cell_x[k]) == 1 && isFiniteNumber(h_y[k]) == 1 )
     {
   h_x[k] = h_NL_x[k]*h_L + h_cell_x[k];
   particle_NNAN = particle_NNAN + 1;
     }
}
for (int kk = 0; kk < particle; kk++)
{
   if ( isFiniteNumber(h_x[kk]) == 1 && isFiniteNumber(h_y[kk]) == 1 )
      {
        mvel[iT] = mvel[iT] + (h_x[kk]-h_x0[kk])/ float(particle_NNAN)\
                            / (h_N_t_all-1)/Tspan ;
        dif[iT] = dif[iT] + (h_x[kk]-h_x0[kk])*(h_x[kk]-h_x0[kk])/2.0\
                            /float(particle_NNAN)/(h_N_t_all-1)/Tspan;
      }
}
if (iT == Nmvel-1 )
{
                 if (h_N_t_all*Tspan >100.0* relax_time\
                         && fabs(dif [iT]- dif [iT-Nmvel/2])\
                          / fabs(dif[iT]) < ThreDif)
                  std = 1;
        else std = 0;
}


/////////////////// make up random number
if ( fmodf(h_N_t_all*Tspan,h_dt*1E7)==0.0 )
```

```
RNG_seedseq_ME<<< blocksPerGrid, threadsPerBlock >>> \
    (d_RNG_seed, time(0),particle);
    }


    ////// 6) calculate and record diffusivity in steady state
    m_vel = 0.0;
    dif_3 = 0.0;
    err_vel = 0.0;
    err_dif_3 = 0.0;
    for (int kk = 0; kk < particle; kk++)
    {
        if ( isFiniteNumber(h_x[kk])==1 && isFiniteNumber(h_y[kk])==1 )
        {
          m_vel = m_vel + (h_x[kk]-h_x0[kk])/float(particle_NNAN)\
                    /(h_N_t_all-1)/Tspan;
          dif_3 = dif_3 + (h_x[kk]-h_x0[kk])*(h_x[kk]-h_x0[kk])/2.0\
                    /float(particle_NNAN)/(h_N_t_all-1)/Tspan;
        }
    }
    for (int kk = 0; kk < particle; kk++)
    {
        if (isFiniteNumber(h_x[kk]) == 1 && isFiniteNumber(h_y[kk]) == 1 )
{

        err_vel = err_vel + ((h_x[kk]-h_x0[kk])\
            /(h_N_t_all-1)/Tspan - m_vel) \
          * ((h_x[kk]-h_x0[kk])/(h_N_t_all-1)/Tspan - m_vel)\
          / float(particle_NNAN);
        err_dif_3 = err_dif_3 + ( (h_x[kk]-h_x0[kk])\
            *(h_x[kk]-h_x0[kk])\
            /2.0/(h_N_t_all-1)/Tspan -dif_3)\
            *((h_x[kk]-h_x0[kk])*(h_x[kk]-h_x0[kk])\
            /2.0/(h_N_t_all-1)\
            /Tspan - dif_3)/float(particle_NNAN);
}
    }
    err_vel = sqrt(err_vel);
    err_dif_3 = sqrt(err_dif_3);

    fprintf(fpvd,"%E  %E  %E  %E  %E  %E   %E   %E   %E \n",\
```

```
            h_Vph,h_Dr,h_Dt,h_Y,h_delta,h_eps,h_psi,m_vel,dif_3);



  ////// 7) close the files and exit CUDA
  fclose(fpvd);
  time(&end_time);
  printf("End at %s\n",asctime(gmtime(&end_time)));
  exit_CUDA();
  return 1;
}


int isFiniteNumber(float d)
// a supplementary function: if d is a finite number then 1
{
return (d <= DBL_MAX && d>=-DBL_MAX);
}


float relax_time_func( float Vph)
// a minimal evolving time before judging the steady-state
{
  float t1;
  if (Vph != 0.0)
  t2 = 1.0/Vph;
  else t1 = 100.0;
  return t1;
}
```

The header file

```
#ifndef header_Janus
#define header_Janus

#include <stdio.h>
#include <stdlib.h>
#include <curand_kernel.h>
#include <math.h>
#include <cuda.h>
#include <time.h>
#include <float.h>


#define particle 256*256   // no. of particle
#define Tspan 50.0  //// interval for testing
#define dt_cons    1E-5
#define N_Tspan  (int)(Tspan/dt_cons)
#define pi  3.1415926
#define ThreDif  1E-2
#define h_L   1.0  /// compartment dimension
#define d_L   1.0
#define Nstuck  2
#define Nmvel   2  // used for steady state check


////////////////  1) variables definition
size_t particle_memsize = particle * sizeof(float);
// variables in host
float h_Dt,h_Dr,h_Y, h_delta,h_Vph,h_dt;
float h_eps,h_psi,h_Torque;
float *h_x, *h_cell_x,*h_y,*h_fi,*h_t,*h_x0,*h_fi0;


// variables in device
float *d_cell_x,*d_y,*d_fi,*d_t;
int *h_NL_x,*d_NL_x;


// constants
__constant__ float d_dt,d_Dt,d_Dr,d_Y,d_Vph,d_delta;
__constant__ float d_eps,d_psi,d_Torque;
```

```
int threadsPerBlock = 256,device_no = 0;
int blocksPerGrid=int(float(particle)/float(threadsPerBlock));
curandState *d_RNG_seed =NULL;



//////////////  2) functions preview
__global__ void RNG_seedseq_ME(curandState *state \
            ,unsigned long seed, int id_max );
//// seeds for random number generator


__host__ void initialize_CUDA_ME();
////initialize the CUDA memory etc.


__global__ void initial_condition(int *NL_x, float *cell_x,float *y\
      , float *fi,float *t,curandState *d_RNG_seed);
//// initial condition


__device__ float bd_shape_Up_ME(float x);
//upper boundary function


__device__ float slope_bd_shape_Up_ME(float x);
// tangential line of upper boundary


__device__ float bd_shape_Down_ME(float x);
//lower boundary


__device__ float slope_bd_shape_Down_ME(float x);
// tangential line of lower boundary


__device__ int bdtest_ME(int NL_xx, float cell_xx, float yy\
     , int NL_x,  float cell_x, float y);
// boundary test


__device__ int bdtest_2_ME(float x_ref, float y_ref);
// boundary test after the reflection


__device__ void update_ME (int *NL_x, float *cell_x\
     , float *y, float *fi, float dt , float r1, float r2, float r3);
// update function for active BM dynamics
```

```
__device__ void reflect_ME (int wall, int *NL_xx, float *cell_xx\
    , float *yy, int *NL_x, float *cell_x, float *y, float *fi);
// reflection function if the particle is OUT


__global__ void evolve_ME( int *NL_x, float *cell_x,float *y\
      , float *t, curandState *d_RNG_seed,float dt);
// the kernel function in GPU


__host__ void exit_CUDA (void);
// Settings for exit



//////////////////////// 3) function definitions
__global__ void RNG_seedseq_ME(curandState *state\
      , unsigned long seed, int id_max)
{
   int id = blockDim.x * blockIdx.x + threadIdx.x;
   if (id < id_max)
    {
           curand_init(seed,id,0,&state[id]);
     }
}


__host__ void initialize_CUDA_ME(void)
{
  /////allocate memory to host variables
  cudaSetDevice(device_no%2);
  h_x0 = (float*) malloc(particle_memsize);
  h_NL_x = (int*) malloc(particle*sizeof(int));
  h_cell_x = (float*) malloc(particle_memsize);
  h_x = (float*) malloc(particle_memsize);
  h_y = (float*) malloc(particle_memsize);
  h_fi = (float*) malloc(particle_memsize);
  h_t = (float*) malloc(particle_memsize);

  //// assign the parameters in device
  cudaMemcpyToSymbol(d_Dt,&h_Dt,sizeof(float));
  cudaMemcpyToSymbol(d_Dr,&h_Dr,sizeof(float));
```

```
cudaMemcpyToSymbol(d_Vph,&h_Vph,sizeof(float));
cudaMemcpyToSymbol(d_Y,&h_Y,sizeof(float));
cudaMemcpyToSymbol(d_delta,&h_delta,sizeof(float));
cudaMemcpyToSymbol(d_Torque,&h_Torque,sizeof(float));
cudaMemcpyToSymbol(d_eps,&h_eps,sizeof(float));
cudaMemcpyToSymbol(d_psi,&h_psi,sizeof(float));
cudaMemcpyToSymbol(d_dt,&h_dt,sizeof(float));


//// allocate memory to device variables
cudaMalloc((void **)&d_NL_x,particle*sizeof(int));
cudaMalloc((void **)&d_cell_x,particle_memsize);
cudaMalloc((void **)&d_y,particle_memsize);
cudaMalloc((void **)&d_fi,particle_memsize);
cudaMalloc((void **)&d_t,particle_memsize);


//// warm up the RNG generating seeds
cudaMalloc((void **)&d_RNG_seed,particle * sizeof(curandState));
RNG_seedseq_ME<<< blocksPerGrid, threadsPerBlock >>>\
          (d_RNG_seed, time(0),particle);
}


__device__ float bd_shape_Up_ME(float x)
{
  float y1;
  y1= 0.5*d_delta+0.5* d_eps* (d_Y-d_delta)*sin(pi*x/d_L \
          + pi * d_psi/2.0)*sin(pi*x/d_L + pi * d_psi/2.0);
  return y1;
}



__device__  float  slope_bd_shape_Up_ME(float x)
{
  float y1;
  y1 = d_eps * pi/d_L*(d_Y - d_delta)/2*2*cos(pi*x/d_L \
          + pi * d_psi/2.0 )*sin(pi*x/d_L + pi * d_psi/2.0);
  return y1;
}


__device__ float bd_shape_Down_ME(float x)
```

```
{
  float y1;
  y1=- 0.5*d_delta- 0.5*(d_Y-d_delta)\
            *sin(pi*x/d_L)*sin(pi*x/d_L);
  return y1;
}


__device__ float slope_bd_shape_Down_ME(float x)
{
  float y2;
  y2 = - pi/d_L*(d_Y - d_delta)/2*2\
              *cos(pi*x/d_L)*sin(pi*x/d_L);
  return y2;
}


__global__ void initial_condition(int *NL_x, float *cell_x\
    ,float *y, float *fi,float *t,curandState *d_RNG_seed)
{
  int i = blockDim.x * blockIdx.x + threadIdx.x;
  NL_x[i] = 0;
  cell_x[i] = float (curand_uniform(&d_RNG_seed[i]));
  y[i] = (float (curand_uniform(&d_RNG_seed[i]))-0.5)\
        * bd_shape_Up_ME(cell_x[i]);
  fi[i] = 2.0*pi*float (curand_uniform(&d_RNG_seed[i]));
  t[i] = 0.0;


}


__device__ void update_ME( int *NL_x, float *cell_x, float *y, float *fi\
    , float dt_up,  float r1, float r2, float r3)
{
  float dx1,dx2,dy1,dy2,dfi;

  dx1 = sqrt(2*d_Dt * dt_up) * r1 ;
  dy1 = sqrt(2*d_Dt * dt_up) * r2 ;
  dx2 = d_Vph * cos(*fi) * dt_up;
  dy2 = d_Vph * sin(*fi) * dt_up;
  dfi = d_Torque* dt_up + sqrt(2*d_Dr * dt_up) * r3;
```

```
  *fi = *fi+dfi;
  *fi = fmodf(*fi,(2*pi));
  if (*fi < 0 )*fi = *fi+2*pi;
  /// update the x position of JP in a certain cell
  *cell_x = *cell_x + dx1 +dx2 ;
  if (*cell_x > 0.0 && *cell_x > fmodf(*cell_x,d_L) )
  {
    *NL_x = *NL_x + 1;
    *cell_x = fmodf(*cell_x,d_L);
  }
  else if ( *cell_x < 0.0 )
  {
    *NL_x = *NL_x - 1;
    *cell_x = d_L + *cell_x;
  }
  *y = *y+dy1+dy2;
}


__device__  int bd_test_ME(int NL_xx, float cell_xx, float yy\
    , int NL_x, float cell_x, float y)
// x,y are intending position; xx,yy are former position
{
  int bdtest;  /// 2,3 OUT; 1 IN
  if (y > bd_shape_Up_ME(cell_x)) bdtest = 2; // OUT from above
  else if ( y < bd_shape_Down_ME(cell_x)) bdtest = 3;
  else if (NL_x > NL_xx && y > bd_shape_Down_ME (cell_x) \
        && y < bd_shape_Up_ME(cell_x) && yy \
        + (NL_x -NL_xx-cell_xx)*(y -yy) /(NL_x \
        + cell_x - NL_xx-cell_xx) > d_delta /2.0)
  bdtest = 2;  /// OUT from below
  else if (NL_x > NL_xx && y > bd_shape_Down_ME (cell_x) \
        && y < bd_shape_Up_ME(cell_x) && yy \
        + (NL_x -NL_xx-cell_xx)*(y -yy) /(NL_x
        + cell_x - NL_xx-cell_xx) < - d_delta /2.0)
  bdtest = 3;  /// OUT from above
  else if (NL_x < NL_xx && y > bd_shape_Down_ME (cell_x) \
        && y < bd_shape_Up_ME(cell_x) && y + (NL_xx\
         -NL_x-cell_x)*(yy -y) /(NL_xx + cell_xx - NL_x\
         - cell_x ) > d_delta /2.0)
```

```
  bdtest = 2; /// OUT from above
  else if (NL_x < NL_xx && y > bd_shape_Down_ME (cell_x) \
          && y < bd_shape_Up_ME(cell_x) && y + (NL_xx\
          -NL_x-cell_x)*(yy -y) /(NL_xx + cell_xx - NL_x\
          - cell_x) < - d_delta /2.0)
  bdtest = 3;  /// OUT from below
  else
  bdtest = 1;  /// IN the confinement

  return bdtest;
}


__device__ int bd_test_2_ME(float cell_x_ref, float y_ref)
\\\ for final check after the reflection
{
     int bdtest_2; /// in or output
     if  (y_ref < bd_shape_Up_ME (cell_x_ref) \
          &&  y_ref > bd_shape_Down_ME (cell_x_ref))
     bdtest_2 = 1; //// IN
     else
     bdtest_2 = 0;  /// OUT
     return bdtest_2;
}



__device__ void reflect_ME (int wall, int *NL_xx, float *cell_xx\
      , float *yy, int *NL_x, float *cell_x, float *y, float *fi)
//// input: old position(xx,yy) and intending position (x,y)
{
     float x_p = 0.0, y_p = 0.0, x_mirror = 0.0, y_mirror = 0.0;
     float   slope_p,ref_x,ref_y;
     float xx, x;
     // (x_p, y_p)  bouncing point, slope_p is the slope at p
     // (x_mirror,y_mirror) position after reflecting
     xx = (*NL_xx) * d_L + *cell_xx;
     x = (*NL_x) * d_L + *cell_x ;
     if (wall == 2)  //// OUT from above
     {
   x_p = xx + (x -xx)/(1 + (bd_shape_Up_ME(x) - *y)\
```

```
                        /(bd_shape_Up_ME(xx) - *yy));
    y_p = bd_shape_Up_ME(x_p);


    slope_p = slope_bd_shape_Up_ME(x_p);
    x_mirror = (*y + x/slope_p - y_p + slope_p * x_p)\
                     /(1/slope_p + slope_p);
    y_mirror = *y + (x - x_mirror)/slope_p;


    ref_x = 2* x_mirror - x;
    ref_y = 2* y_mirror - *y;
      }


      if (wall == 3)  //// OUT from below
      {
    x_p = xx + (x -xx)/(1 + (bd_shape_Down_ME(x) - *y)\
                     /(bd_shape_Down_ME(xx) - *yy));
    y_p = bd_shape_Down_ME(x_p);


    slope_p = slope_bd_shape_Down_ME(x_p);
    x_mirror = (*y + x/slope_p - y_p + slope_p * x_p)\
                     /(1/slope_p + slope_p);
    y_mirror = *y + (x - x_mirror)/slope_p;


    ref_x = 2* x_mirror - x;
    ref_y = 2* y_mirror - *y;
       }


   *NL_x = ref_x -fmodf(ref_x,d_L);
   *cell_x = fmodf(ref_x,d_L);
   if (*cell_x < 0.0)
   {
       *NL_x = *NL_x - 1;
       *cell_x = *cell_x + d_L;
   }
  (*y) = ref_y;
}



__global__ void evolve_ME( int *NL_x, float *cell_x,float *y, float *fi\
```

```
            , float *t, curandState *d_RNG_seed,float dt)
{
    int i = blockDim.x * blockIdx.x + threadIdx.x;
    int counter, bdtest=1,bdtest_2=1;
    //bdtest: out(in) of the wall;
    float r1,r2,r3;
    float cell_x_upd,y_upd,fi_upd;
    int NL_x_upd, istuck = 0 ;

    bdtest = 0;
    for (counter = 0; counter < N_Tspan; counter++)
    {
         ///// [1] record the state of last time step
bdtest = 0;
istuck = 0;
          NL_x_upd = NL_x[i];
cell_x_upd = cell_x[i];
y_upd = y[i];
fi_upd = fi[i];



 ///// [2] obtain random numbers for update
          r1 = float (curand_normal (&d_RNG_seed[i]));
r2 = float (curand_normal (&d_RNG_seed[i]));
r3 = float (curand_normal (&d_RNG_seed[i]));
while( r1==0.0||r2==0.0||r1 ==1.0||r2 == 1.0\
                     || r3 == 0.0|| r3 == 1.0)
  {
    r1 = float (curand_normal (&d_RNG_seed[i]));
    r2 = float (curand_normal (&d_RNG_seed[i]));
    r3 = float (curand_normal (&d_RNG_seed[i]));
  }



       //// [3] call for update function
update_ME(&NL_x_upd,&cell_x_upd,&y_upd,&fi_upd,dt,r1,r2,r3);


//// [4] test IN/ OUT for the intending position
```

```
bdtest = bd_test_ME (NL_x[i],cell_x[i],y[i]\
                    ,NL_x_upd,cell_x_upd,y_upd);


if (bdtest!=1 )  /// if OUT, call for reflecting function
{
      reflect_ME( bdtest, &NL_x[i],&cell_x[i],&y[i]\
                        , &NL_x_upd,&cell_x_upd,&y_upd,&fi_upd);
      fi_upd = fi[i];
      bdtest_2 = bd_test_2_ME (cell_x_upd,y_upd);
                istuck = istuck + 1;
  }


if (bdtest!=1)   /// the treatment for "stuck"
{
            while (istuck <= Nstuck && bdtest_2 == 0)
 {
                istuck =istuck +1;
                NL_x_upd=NL_x[i];
                cell_x_upd=cell_x[i];
                y_upd=y[i];
                fi_upd = fi[i];

                r1 = float (curand_normal (&d_RNG_seed[i]));
                r2 = float (curand_normal (&d_RNG_seed[i]));
                r3 = float (curand_normal (&d_RNG_seed[i]));
                while ( r1==0.0||r2==0.0||r1 ==1.0 || r2 == 1.0\
                        || r3 == 0.0 || r3 == 1.0)
                {
                        r1 = float (curand_normal (&d_RNG_seed[i]));
                        r2 = float (curand_normal (&d_RNG_seed[i]));
                        r3 = float (curand_normal (&d_RNG_seed[i]));
                 }
                update_ME(&NL_x_upd,&cell_x_upd,&y_upd,&fi_upd\
                            ,dt,r1,r2,r3);
                bdtest = bd_test_ME (NL_x[i],cell_x[i],y[i],NL_x_upd\
                            ,cell_x_upd,y_upd);
                if (bdtest !=1 )  // if OUT
                {
                        reflect_ME( bdtest, &NL_x[i],&cell_x[i],&y[i]\
```

```
                                    , &NL_x_upd,&cell_x_upd,&y_upd,&fi_upd);
                        fi_upd = fi[i];
                        bdtest_2 = bd_test_2_ME (cell_x_upd,y_upd);
                 }
                else break;
      }
}



//// [5] assign the update state
            if ( bdtest_2 == 0 && istuck > Nstuck)
{
    fi[i] = fi_upd;
    t[i] = t[i]+dt;
}
else if ((bdtest_2 == 1 && bdtest != 1) || bdtest == 1)
{
  NL_x[i] = NL_x_upd;
  cell_x[i] = cell_x_upd;
  y[i] = y_upd;
  fi[i] = fi_upd;
  t[i] = t[i] +dt;
}
      }
 }


__host__ void exit_CUDA (void)
{
free(h_x0);
free(h_x);
free(h_cell_x);
free(h_NL_x);
free(h_y);
free(h_fi);
free(h_t);
cudaFree(d_cell_x);
cudaFree(d_y);
cudaFree(d_fi);
cudaFree(d_t);
```

```
cudaFree(d_RNG_seed);
}


#endif
```

Bibliography

[1] G. M. Cooper. *The Cell: A Molecular Approach.* Sinauer Associates, Sunderland, MA, USA), 2000.

[2] B. Alberts and R. Miake-Lye. Unscrambling the puzzle of biological machines: The importance of the details. *Cell*, 68(415), 1992.

[3] B. Alberts. The cell as a collection of protein machines: Preparing the next generation of molecular biologists. *Cell*, 92(291), 1998.

[4] C. Mavroidis, A. Dubey, and M. L. Yarmush. Molecular machines. *Annu. Rev. Biomed. Eng*, 6(363), 2004.

[5] M. Schliwa and G. Woehlke. Molecular motors. *Nature*, 422(01601), 2003.

[6] R. Ballardini, V. Balzani, A. Credi, M. T. Gandolfi, and M. Venturi. Artificial molecular-level machines: Which energy to make them work? *Acc. Chem. Res.*, 34(6)(445), 2001.

[7] R. Kapral. Perspective: Nanomotors without moving parts that propel themselves in solution. *J. Chem. Phys.*, 138(020901), 2013.

[8] J.-S. Shin and N. A. Pierce. A synthetic DNA walker for molecular transport. *J. Am. Chem. Soc.*, 126(10834), 2004.

[9] P. Yin, H. Yan, X. G. Daniell, A. J. Turberfield, and J. H. Reif. A unidirectional DNA walker moving autonomously along a linear track. *Angew. Chem. Int. Ed.*, 43(4906), 2004.

[10] Y. Tian, Y. He, Y. Chen, P. Yin, and C. Mao. A DNAzyme that walks processively and autonomously along a one-dimensional track. *Angew. Chem. Int. Ed.*, 44 (4355), 2005.

[11] R. Pei, S. K. Taylor, D. Stefanovic, S. Rudchenko, T. E. Mitchell, and M. N. Stojanovic. Behavior of polycatalytic assemblies in a substrate-displaying matrix. *J. Am. Chem. Soc.*, 128(12693), 2006.

[12] P. Yin, H. M. T. Choi, C. R. Calvert, and N. A. Pierce. Programming biomolecular self-assembly pathways. *Nature*, 451(318), 2008.

[13] T. Omabegho, R. Sha, and N. C. Seeman. A bipedal DNA Brownian motor with coordinated legs. *Science*, 67(324), 2009.

[14] E. H. C. Bromley, N. J. Kuwada, M. J. Zuckermann, R. Donadini, L. Samii, G. A. Blab, G. J. Gemmen, B. J. Lopez, P. M. G. Curmi, and N. R. Forde. The tumbleweed: Towards a synthetic protein motor. *HFSP J.*, 3(204), 2009.

[15] K. Lund, A. J. Manzo, N. Dabby, N. Michelotti, A. Johnson-Buck, J. Nangreave, S. Taylor, R. Pei, M. N. Stojanovic, and N. G.Walter. Molecular robots guided by prescriptive landscapes. *Nature*, 465(206), 2010.

[16] V. Balzani, M. Venturi, and A. Credi. *Molecular Devices and Machines: A Journey into the Nano World*. Wiley-VCH, Weinheim, 2002.

[17] K. Hoki, M. Yamaki, S. Koseki, and Y. Fujimura. Molecular motors driven by laser pulses: Role of molecular chirality and photon helicity. *J. Chem. Phys.*, 118 (497), 2003.

[18] H. Hess, G. D. Bach, and V. Vogel. Powering nanodevices with biomolecular motors. *Chem. Eur. J.*, 10(2110), 2004.

[19] R. Dreyfus, J. Baudry, M. L. Roper, M. Fermigier, J. Bibette, and H. A. Stone. Microscopic artificial swimmer. *Nature*, 437(862), 2005.

[20] S. P. Fletcher, F. Dumur, M. M. Pollard, and B. L. Feringa. A reversible, unidirectional molecular rotary motor driven by chemical energy. *Science*, 310(80), 2005.

[21] D. H. Qu, Q. C. Wang, and H. Tian. A half-adder based on a photochemically driven. *Angew. Chem. Int. Ed.*, 44(5296), 2005.

[22] E. R. Kay, D. A. Leigh, and F. Zerbetto. Synthetic molecular motors and mechanical machines. *Angew. Chem. Int. Ed.*, 46(72), 2007.

[23] V. Balzani, A. Credi, and M. Venturi. Molecular machines working on surfaces and at interfaces. *ChemPhysChem*, 9(202), 2008.

[24] H. A. Zambrano, J. H. Walther, and R. L. Jaffe. Thermally driven molecular linear motors: A molecular dynamics study. *J. Chem. Phys.*, 131(241104), 2009.

[25] I. Buttinoni, G. Volpe, G. Volpe F. Kümmel, and C. Bechinger. Active Brownian motion tunable by light. *J. Phys.: Condens. Matter*, 24(284129), 2012.

[26] J. R. Howse, R. A. Jones, A. J. Ryan, T. Gough, R. Vafabakhsh, and R. Golestanian. Self-motile colloidal particles: From directed propulsion to random walk. *Phys. Rev. Lett.*, 99(048102), 2007.

[27] W. F. Paxton, S. Sundararajan, T. E. Mallouk, and A. Sen. Chemical locomotion. *Angew. Chem., Int. Ed.*, 45(5420), 2006.

[28] G. A. Ozin, I. Manners, S. Fournier-Bidoz, and A. Arsenault. Dream nanomachines. *Adv. Mater.*, 17(3011), 2005.

[29] Y. Wang, R. M. Hernande, D. J. Bartlett, J. M. Bingham, T. R. Kline, A. Sen, and T. E. Mallouk. Bipolar electrochemical mechanism for the propulsion of catalytic nanomotors in hydrogen peroxide solutions. *Langmuir*, 22(10451), 2006.

[30] L. F. Valadares, Y. G. Tao, N. S. Zacharia, V. Kitaev, F. Galembeck, R. Kapral, and G. A. Ozin. Catalytic nanomotors: Self-propelled sphere dimers. *Small*, 6 (565), 2010.

[31] W. F. Paxton, K. C. Kistler, C. C. Olmeda, A. Sen, S. K. St. Angelo, Y. Cao, T. E. Mallouk, P. E. Lammert, and V. H. Crespi. Catalytic nanomotors: Autonomous movement of striped nanorods. *J. Am. Chem. Soc.*, 126(13424), 2004.

[32] S.Fournier-Bidoz, A. C. Arsenault, I. Manners, and G. A. Ozin. Synthetic self-propelled nanorotors. *J. Chem. Soc. Chem. Commun.*, 11(4), 2005.

[33] R. Laocharoensuk, J. Burdick, and J. Wang. Carbon-nanotube-induced acceleration of catalytic nanomotors. *ACS Nano*, 2(1069), 2008.

[34] H. Ke, S. Ye, R. L. Carroll, and K. Showalter. Motion analysis of self-propelled Pt-silica particles in hydrogen peroxide solutions. *J. Phys. Chem. A*, 114(5462), 2010.

[35] G. Rückner and R. Kapral. Chemically powered nanodimers. *Phys. Rev. Lett.*, 98 (150603), 2007.

[36] J. Kärger and D. M. Ruthven. *Diffusion in Zeolites and Other Microporous Solids.* Wiley, New York, 1992.

[37] A. Fick. Über diffusion. *Ann. Phys.*, 94(59), 1855.

[38] R. Brown. Xxvii. A brief account of microscopical observations made in the months of june, july and august, 1827, on the particles contained in the pollen of plants; and on the general existence of active molecules in organic and inorganic bodies. *Phil. Mag.*, 4(161), 1828.

[39] A. Einstein. Über die von der molekularkinetischen Theorie der Wärme geforderte Bewegung von in ruhenden Flüssigkeiten suspendierten Teilchen. *Ann. Phys. (Leipzig)*, 17(549), 1905.

[40] A. Einstein. Eine neue Bestimmung der Moleküldimensionen. *Ann. Phys. (Leipzig)*, 19(289), 1906.

[41] W. Sutherland. LXXV. A dynamical theory of diffusion for non-electrolytes and the molecular mass of albumin. *Phil. Mag.*, 9(781), 1905.

[42] M. von Smoluchowski. Zur kinetischen Theorie der Brownschen Molekularbewegung und der Suspensionen. *Ann. Phys.*, 326(14), 1906.

[43] P. Langevin. Sur la théorie du mouvement Brownien. *C. R. Acad. Sci.*, 146(530), 1908.

[44] H. B. Callen and T. A. Welton. Irreversibility and generalized noise. *Phys. Rev.*, 83(1), 1951.

[45] R. Kubo. Statistical-mechanical theory of irreversible processes. I. General theory and simple applications to magnetic and conduction problems. *J. Phys. Soc. Jpn.*, 12(6), 1957.

[46] J. Perrin. Les atomes. *Competes. Rendues. Acad. Sci.*, 158(1168), 1914.

[47] T. Li, S. Kheifets, D. Medellin, and M. G. Raizen. Measurement of the instantaneous velocity of a Brownian particle. *Science*, 328(5986), 2010.

[48] R. Huang, I. Chavez, K. M. Taute, B. Lukic, S. Jeney, M. G. Raizen, and E. L. Florin. Direct observation of the full transition from ballistic to diffusive Brownian motion in a liquid. *Nat. Phys.*, 7(7), 2011.

[49] B. Hille. *Ion Channels of Excitable Membranes.* Sinauer, Sunderland, 2001.

[50] R. M. Barrerr. *Zeolites an Clay Minerals as Sorbents and Molecular Sieves.* Academic Press, London, 1978.

[51] C. Baerlocher, W. M. Meier, and D. H. Oslon. *Atlas of Zeolite Framework Types.* Elsevier, Amsterdam, 2001.

[52] J. Kärger and D. M. Ruthven. *Diffusion in Zeolites and Other Microporous Solids.* Wiley, New York, 1992.

[53] T. Chou and D. Lohse. Entropy-driven pumping in zeolites and biological channels. *Phys. Rev. Lett.*, 82(3552), 1999.

[54] L. Liu, P. Li, and S. A. Asher. Entropic trapping of macromolecules by mesoscopic periodic voids in a polymer hydrogel. *Nature*, 397(141), 1999.

[55] Z. Siwy and A. Fulinski. Fabrication of a synthetic nanopore ion pump. *Phys. Rev. Lett.*, 89(198103), 2002.

[56] Z. Siwy, I. D. Kosinska, A. Fulinski, and C. R. Martin. Asymmetric diffusion through synthetic nanopores. *Phys. Rev. Lett.*, 94(048102), 2005.

[57] I. D. Kosinska, I. Goychuk, M. Kostur, G. Schmid, and P. Hänggi. Rectification in synthetic conical nanopores: A one-dimensional Poisson-Nernst-Planck modeling. *Phys. Rev. E.*, 77(031131), 2008.

[58] A. M. Berezhkovskii and S. M. Bezrukov. Optimizing transport of metabolites through large channels: Molecular sieves with and without binding. *Biophys. J.*, 88(3), 2005.

[59] C. Kettner, P. Reimann, P. Hänggi, and F. Müller. Drift ratchet. *Phys. Rev. E*, 61(312), 0000.

[60] S. Matthias and F. Müller. Asymmetric pores in a silicon membrane acting as massively parallel Brownian ratchets. *Nature*, 4240(53), 2003.

[61] F. Müller, A. Birner, J. Schilling, U. Gösele, Ch. Kettner, and P. Hänggi. Membranes for micropumps from macroporous silicon. *Physica Status Solidi (a)*, 182 (585), 2000.

[62] R. Zwanzig. Diffusion past an entropy barrier. *J. Phys. Chem*, 96(3926), 1992.

[63] M. H. Jacobs. *Diffusion Processes*. Springer, New York, 1976.

[64] D. Reguera and J. M. Rubi. Kinetic equations for diffusion in the presence of entropic barriers. *Phys. Rev. E*, 64(061106), 2001.

[65] W. D. Volkmuth and R. H. Austin. DNA electrophoresis in microlithographic arrays. *Nature*, 358(600), 1992.

[66] G. I. Nixon and G. W. Slater. Saturation and entropic trapping of monodisperse polymers in porous media. *J. Chem. Phys.*, 117(4042), 2002.

[67] R. Chang and A. Yethiraj. Dynamics of chain molecules in disordered materials. *Phys. Rev. Lett.*, 96(107802), 2006.

[68] D. Reguera, G. Schmid, P. S. Burada, and J. M. Rubi. Entropic transport: kinetics, scaling, and control mechanisms. *Phys. Rev. Lett.*, 96(130603), 2006.

[69] P. S. Burada, G. Schmid, D. Reguera, J. M. Rubi, and P. Hänggi. Bias diffusion in confined media: Test of the Fick-Jacobs approximation and validity criteria. *Phys. Rev. E*, 75(051111), 2007.

[70] P. Talkner P. Hänggi D. Reguera P. S. Burada, G. Schmid and J. M. Rubi. Entropic particle transport in periodic channels. *BioSystems*, 93(16), 2008.

[71] S. Burada. *Entropic Transport in Confined Media*. PhD thesis, Universität of Augsburg, Germany, 2008.

[72] S. Martens. *Transport of Brownian Particles in Confined Geometries: Steps beyond the Fick-Jacobs Approach*. PhD thesis, Humboldt-Universität zu Berlin, Germany, 2012.

[73] F. J. Keil, R. Krishna, and M.-O. Coppens. Modeling of diffusion in zeolites. *Rev. Chem. Eng.*, 16(2), 2000.

[74] B. Lindner, J. Garcia-Ojalvo, A. Neiman, and L. Schimansky-Geier. Effects of noise in excitable systems. *Phys. Rep.*, 392(321), 2004.

[75] Z. Siwy and A. Fulinski. A nanodevice for rectification and pumping ions. *Am. J. Phys.*, 72(567), 2004.

[76] M. Firnkes, D. Pedone, J. Knezevic, M. Döblinger, and U. Rant. Electrically facilitated translocations of proteins through silicon nitride nanopores: Conjoint and competitive action of diffusion, electrophoresis, and electroosmosis. *Nano Lett.*, 10(6), 2010.

[77] D. Pedone, M. Langecker, G. Abstreiter, and U. Rant. A pore-cavity-pore device to trap and investigate single nanoparticles and DNA molecules in a femtoliter compartment: Confined diffusion and narrow escape. *Nano Lett.*, 11(4), 2011.

[78] T. M. Squires and S. R. Quake. Microfluidics: Fluid physics at the nanoliter scale. *Rev. Mod. Phys.*, 77(3), 2005.

[79] D. Schuring. *Diffusion in Zeolites: Towards a Microscopic Understanding*. PhD thesis, Eindhoven University of Technology, The Netherlands, 2002.

[80] W. J. Roth, P. Nachtigall, R. E. Morris, and J. Cejka. Two-dimensional zeolites: Current status and perspectives. *Chem. Rev.*, 114(4807), 2014.

[81] T. A. J. Duke and R.H. Austin. Microfabricated sieve for the continuous sorting of macromolecules. *Phys. Rev. Lett.*, 80(1552), 1998.

[82] J. Fu, J. Yoo, and J. Han. Molecular sieving in periodic free-energy landscapes created by patterned nanolter arrays. *Phys. Rev. Lett.*, 97(018103), 2006.

[83] J. B. Heng, C. Ho, T. Kim, R. Timp, A. Aksimentiev, Y. V. Grinkova, S. Sligar, K. Schulten, and G. Timp. Sizing DNA using a nanometer-diameter pore. *Biophys. J.*, 87(2905), 2004.

[84] A. J. Storm, J. H. Chen, X. S. Ling, H. W. Zandbergen, and C. Dekker. Fabrication of solid-state nanopores with single-nanometer precision. *Nature Mater.*, 2(537), 2003.

[85] S. Van Dorp D. Krapf R. M. M. Smeets S. G. Lemay N. H. Dekker U. F. Keyser, B. N. Koeleman and C. Dekker. Direct force measurements on DNA in a solid-state nanopore. *Nat. Phys.*, 2(473), 2006.

[86] U. F. Keyser, J. van der Does, C. Dekker, and N. H. Dekker. Optical tweezers for force measurements on DNA in nanopores. *Rev. Sci. Instrum.*, 77(105105), 2006.

[87] A. Schüring, S. M. Auerback, S. Fritzsche, and R. Haberlandt. On entropic barriers for diffusion in zeolites: A molecular dynamics study. *J. Chem. Phys.*, 116(10890), 2002.

[88] A. M. Berezhkovskii, M. A. Pustovoit, and S. M. Bezrukov. Diffusion in a tube of varying cross section: Numerical study of reduction to effective one-dimensional description. *J. Chem. Phys.*, 126(134706), 2007.

[89] A. S. Verkman. Solute and macromolecule diffusion in cellular aqueous compartments. *Trends Biochem.*, 27(1), 2002.

[90] A. E. Cohen and W. E. Moerner. Suppressing Brownian motion of individual biomolecules in solution. *Proc. Nat. Ac. Sc. U.S.A*, 103(12), 2006.

[91] B. Alberts, A. Johnson, J. Lewis, M. Raff, K. Roberts, and P.Walter. *Molecular Biology of the Cell.* Garland Science, New York, 2002.

[92] A. M. Berezhkovskii and S. M. Bezrukov. Counting translocations of strongly repelling particles through single channels: Fluctuation theorem for membrane transport. *Phys. Rev. Lett.*, 100(3), 2008.

[93] S. Rüdiger and L. Schimansky-Geier. Dynamics of excitable elements with time-delayed coupling. *J. Theo. Bio.*, 259(1), 2009.

[94] I. V. Grigoriev, Y. A. Makhnovskii, A. M. Berezhkovskii, and V. Y. Zitserman. Kinetics of escape through a small hole. *J. Chem. Phys.*, 116(22), 2002.

[95] P. S. Burada, P. Hänngi, F. Marchesoni, G. Schmid, and P. Talkner. Diffusion in the confined geometries. *ChemPhysChem*, 10(45), 2009.

[96] P. S. Burada, G. Schmid, D. Reguera, M. H. Vainstein, J. M. Rubi, and P. Hänggi. Entropic stochastic resonance. *Phys. Rev. Lett.*, 101(130602), 2008.

[97] P. S. Burada, G. Schmid, P. Talkner, P. Hänggi, D. Reguera, and J. M. Rubi. Entropic particle transport in periodic channels. *BioSystems*, 93(16), 2008.

[98] P. S. Burada and G. Schmid. Steering the potential barriers: Entropic to energetic. *Phys. Rev. E*, 82(051128), 2010.

[99] L. A. Cameron, M. J. Footer, A. van Oudenaarden, and J. A. Theriot. Motility of ActA protein-coated microspheres driven by actin polymerization. *Proc. Natl. Acad. Sci. USA*, 96(4908), 1999.

[100] D. Pantaloni, C. Le Clainche, and M. F. Carlier. Mechanism of actin-based motility. *Science*, 292(1502), 2001.

[101] A. B. Groswasser, S. Wiesner, R. M. Golsteyn, M. F. Carlier, and C. Sykes. The dynamics of actin-based motility depend on surface parameters. *Nature*, 417(308), 2002.

[102] H. Berg. *E. Coli in Motion.* Springer Verlag, New York, 2004.

[103] D. B. Weibel, P. Garstecki, D. Ryan, W. R. DiLuzio, M. Mayer, J. E. Seto, and G. M. Whitesides. Microoxen: Microorganisms to move microscale loads. *Proc. Natl. Acad. Sci. USA,*, 102(11963), 2005.

[104] C. D. Chin, V. Linder, and S. K. Sia. Lab-on-a-chip devices for global health. *Lab Chip*, 7(41), 2007.

[105] W. Yang, V. R. Misko, K. Nelissen, M. Kong, and F. M. Peeters. Using self-driven microswimmers for particle separation. *Soft Matter*, 8(5175), 2012.

[106] Z. Ghalanbor, S. A. Mareshi, and B. Ranjbar. Nanotechnology helps medicine: Nanoscale swimmers and their future applications. *Med. Hypo.*, 65(198), 2005.

[107] S. J. Ebbens and J. R. Howse. In the pursuit of propulsion at the nanoscale. *Soft Matter*, 6(726), 2010.

[108] S. Childress. *Mechanics of Swimming and Flying.* Cambridge University Press, Cambridge, 1981.

[109] J. Happel and H. Brenner. *Low Reynolds Number Hydrodynamics.* Prentice-Hall, Englewood Cliffs, NJ, 1965.

[110] E. M. Purcell. Life at low Reynolds number. *Am. J. Phys*, 45(3), 1977.

[111] R. Lipowsky, Y. Chai, S. Klumpp, S. Leipelt, and M. J. I. Muller. Molecular motor traffic: From biological nanomachines to macroscopic transport. *Phys. A*, 372(34), 2006.

[112] R. F. Ismagilov, A. Schwartz, N. Bowden, and G. M. Whitesides. Autonomous movement and self-assembly. *Angew. Chem.*, 114(674), 2002.

[113] W. F. Paxton, K. C. Kistler, C. C. Olmeda, A. Sen, S. K. Angelo, Y. Cao, T. E. Mallouk, P. E. Lammert, and V. H. Crespi. Catalytic nanomotors: Autonomous movement of striped nanorods. *J. Am. Chem. Soc.*, 126(13424), 2004.

[114] W. F. Paxton, A. Sen, and T. E. Mallouk. Motility of catalytic nanoparticles through self-generated forces. *Chem. Eur. J.*, 11(6462), 2005.

[115] T. R. Kline, W. F. Paxton, T. E. Mallouk, and A. Sen. Catalytic nanomotors: Remote-controlled autonomous movement of striped metallic nanorods. *Angew. Chem., Int. Ed.*, 44(744), 2005.

[116] J. M. Catchmark, S. Subramanian, and A. Sen. Directed rotational motion of microscale objects using interfacial tension gradients continually generated via catalytic reactions. *Small*, 1(202), 2005.

[117] P. Dhar, T. M. Fischer, Y. Wang, T. E. Mallouk, W. F. Paxton, and A. Sen. Autonomously moving nanorods at a viscous interface. *Nano Lett.*, 6(66), 2006.

[118] T. R. Kline, M. Tian, J. Wang, A. Sen, M. W. H. Chan, and T. E. Mallouk. Template-grown metal nanowires. *Inorg. Chem.*, 45(7555), 2006.

[119] W. F. Paxton, P. T. Baker, T. R. Kline, Y. Wang, T. E. Mallouk, and A. Sen. Catalytically induced electrokinetics for nanomotors and nanopumps. *J. Am. Chem. Soc.*, 128(14882), 2006.

[120] P. Dhar, Y. Y. Cao, T. Kline, P. Pal, C. Swayne, T. M. Fischer, B. Miller, T. E. Mallouk, A. Sen, and T. H. Johansen. Autonomously moving local nanoprobes in heterogeneous magnetic fields. *J. Phys. Chem. C*, 111(3607), 2007.

[121] M. E. Ibele, Y. Wang, T. R. Kline, T. E. Mallouk, and A. Sen. Hydrazine fuels for bimetallic catalytic microfluidic pumping. *J. Am. Chem. Soc.*, 129:7762, 2007.

[122] S. Fournier-Bidoz, A. C. Arsenault, I. Manners, and G. A. Ozin. Synthetic self-propelled nanorotors. *Chem. Commun.*, (441), 2005.

[123] Y. Hong, N. M. K. Blackman, N. D. Kopp, A. Sen, and D. Velegol. Chemotaxis of nonbiological colloidal rods. *Phys. ReV. Lett.*, 99(178103):178103, 2007.

[124] T. R. Kline, J. Iwata, P. E. Lammert, T. E. Mallouk, A. Sen, and D. Velegol. Catalytically driven colloidal patterning and transport. *J. Phys. Chem. B*, 110 (24513), 2006.

[125] G. Volpe, I. Buttinoni, D. Vogt, H. J. Kümmer, and C. Bechinger. Microswimmers in patterned environments. *Soft Matter*, 7(8810), 2011.

[126] F. Kümmel, B. ten Hagen, R. Wittkowski, I. Buttinoni, R. Eichhorn, G. Volpe, H. Löwen, and C. Bechinger. Circular motion of asymmetric self-propelling particles. *Phys. Rev. Lett.*, 110(198302), 2013.

[127] G. Zhao and M. Pumera. Geometric asymmetry driven Janus micromotors. *Nanoscale*, 10(1039), 2014.

[128] Wikipedia. http://en.wikipedia.org/wiki/Phoresis_(biology).

[129] J. L. Anderson, M. E. Lowell, and D. C. Prieve. Motion of a particle generated by chemical gradients. Part I: Non-electrolytes. *J. Fluid Mech.*, 117(107), 1982.

[130] J. L. Anderson and D. C. Prieve. Diffusiophoresis: migration of colloidal particles in gradients of solute concentration. *Sep. Purif. Rev.*, 13(67), 1984.

[131] J. L. Anderson. Colloid transport by interfacial forces. *Ann. Rev. Fluid Mech.*, 21 (61), 1989.

[132] J. L. Anderson and D. C. Prieve. Diffusiophoresis of particles in gradients of strongly adsorbing solutes. *Langmuir*, 7(403), 1991.

[133] F. Jülicher and J. Prost. Generic theory of colloidal transport. *Eur. Phys. J.*, 29 (27), 2009.

[134] X. C. Lu, J. P. Hsu, and S. Tseng. Diffusiophoresis of a nonuniformly charged sphere in an electrolyte solution. *J. Chem. Phys.*, 134(064708), 2011.

[135] B. J. Kirby. *Micro- and Nanoscale Fluid Mechanics: Transport in Microfluidic Devices*. Cambridge University Press, Cambridge, 2010.

[136] J. L. Anderson. Colloid transport by interfacial forces. *Annu. Rev. Fluid Mech.*, 21(61), 1989.

[137] P. E. Lammert, J. Prost, and R. Bruinsma. Ion drive for vesicles and cells. *J. Theor. Biol.*, 178(387), 1996.

[138] J. P. Ebel, J. L. Anderson, and D.C. Prieve. Diffusiophoresis of latex particles in electrolyte gradients. *Langmuir*, 4(396), 1988.

[139] R. Golestanian, T.B. Liverpool, and A. Ajdari. Propulsion of a molecular machine by asymmetric distribution of reaction products. *Phys. Rev. Lett.*, 94(220801), 2005.

[140] N. Mano and A. Heller. Bioelectrochemical propulsion. *J. Am. Chem. Soc.*, 127 (11574), 2005.

[141] J. Gibbs and Y. Zhao. Autonomously motile catalytic nanomotors by bubble propulsion. *Appl. Phys. Lett.*, 94(163104), 2009.

[142] H. R. Jiang, N. Yoshinaga, and M. Sano. Active motion of a Janus particle by self-thermophoresis in a defocused laser beam. *Phys. Rev. Lett.*, 105(268302), 2010.

[143] B. ten Hagen, S. van Teeffelen, and H. Löwen. Brownian motion of a self-propelled particle. *J. Phys.: Condens. Matter*, 23(194119), 2011.

[144] M. Doi and S. F. Edwards. *The Theory of Polymer Dynamics*. Oxford Science Publications, Oxford, 1986.

[145] S. van Teeffelen and H. Löwen. Dynamics of a Brownian circle swimmer. *Phys. Rev. E*, 78(020101), 2008.

[146] M. T. Downton and H. Stark. Simulation of a model microswimmer. *J. Phys.: Condens. Matter*, 21(204101), 2009.

[147] K. Drescher, R. E. Goldstein, N. Michel, M. Polin, and I. Tuval. Direct measurement of the flow field around swimming microorganisms. *Phys. Rev. Lett.*, 105 (168101), 2010.

[148] M. Mijalkov and G. Volpe. Sorting of chiral microswimmers. *Soft Matter*, 9(6376), 2013.

[149] E. Lauga, W. R. DiLuzio, George, M. Whitesides, and H. A. Stone. Swimming in circles: Motion of bacteria near solid boundaries. *Biophys. J.*, 90(400), 2006.

[150] D. M. Woolley. Motility of spermatozoa at surfaces. *Reproduction (Bristol, U.K.)*, 126(259), 2003.

[151] I. H. Riedel, K. Kruse, and J. Howard. A self-organized vortex array of hydrodynamically entrained sperm cells. *Science*, 309(300), 2005.

[152] A. Walther and A. H. Müller. Janus particles. *Soft Matter*, 4(663), 2008.

[153] A. Kudrolli, G. Lumay, D. Volfson, and L. S. Tsimring. Swarming and swirling in self-propelled granular rods. *Phys. Rev. Lett.*, 100(058001), 2008.

[154] A. Boymelgreen, G. Yossifon, S. Park, and T. Miloh. Spinning Janus doublets driven in uniform AC electric fields. *Phys. Rev. E*, 89(011003), 2014.

[155] A. Zöttl and H. Stark. Nonlinear dynamics of a microswimmer in Poiseuille flow. *Phys. Rev. Lett.*, 108(218104), 2012.

[156] P. K. Radtke and L. Schimansky-Geier. Directed transport of confined Brownian particles with torque. *Phys. Rev. E*, 85(051110), 2012.

[157] S. Ebbens, R. A. Jones, A. J. Ryan, R. Golestanian, and J. R. Howse. Self-assembled autonomous runners and tumblers. *Phys. Rev. E*, 82(015304), 2010.

[158] B. Alberts, A. Johnson, J. Lewis, M. Raff, K. Roberts, and P. Walter. *Molecular Biology of the Cell*. Garland Science, New York, 2007.

[159] A. Berezhkovskii and G. Hummer. Single-file transport of water molecules through a carbon nanotube. *Phys. Rev. Lett.*, 89(064503), 2002.

[160] J. C. T. Eijkel and A. van den Berg. Nanofluidics: What is it and what can we expect from it? *Microfluid Nanofluid*, 1(249), 2005.

[161] Kärger, D. M. Ruthven, and D. N. Theodorou. *Diffusion in Nanoporous Materials*. Wiley-VHC, Weinheim, 2012.

[162] M. Gershow and J. A. Golovchenco. Recapturing and trapping single molecules with a solid-state nanopore. *Nat. Nanotechnol.*, 2(775), 2007.

[163] C. Dekker. Solid-state nanopores. *Nature Nanotechnology*, 2(209), 2007.

[164] S. Pagliara, C. Schwall, and U. F. Keyser. Optimizing diffusive transport through a synthetic membrane channel. *Advanced Materials*, 25(844), 2013.

[165] R. M. Mazo. *Brownian Motion: Fluctuations, Dynamics and Applications*. Clarendon Press, Oxford, 2002.

[166] P. Hänggi and F. Marchesoni. 100 years of Brownian motion. *Chaos*, 15(026101), 2005.

[167] P. Hänggi and F. Marchesoni. Artificial Brownian motors: Controlling transport on the nanoscale. *Rev. Mod. Phys.*, 81(387), 2009.

[168] K. Healy. Nanopore-based single-molecule DNA analysis. *Nanomedicine*, 2(459), 2007.

[169] K. Healy, B. Schmidt, and A. P. Morrison. Solid-state nanopore technologies for nanopore-based DNA analysis. *Nanomedicine*, 2(875), 2007.

[170] R. Eichhorn, P. Reimann, and P. Hänggi. Brownian motion exhibiting absolute negative mobility. *Phys. Rev. Lett.*, 88(190601), 2002.

[171] M. Kostur, L. Machura, P. Talkner, P. Hänggi, and J. Luczka. Anomalous transport in biased ac-driven Josephson junctions: Negative conductances. *Phys. Rev. B*, 77(104509), 2008.

[172] E. Arvanitidou and D. Hoagland. Chain-length dependence of the electrophoretic mobility in random gels. *Phys. Rev. Lett.*, 67(1464), 1991.

[173] J. J. Kasianowicz, E. Bradin, D. Branton, and D. W. Deemer. Characterization of individual polynucleotide molecules using a membrane channel. *Proc. Natl. Acad. Sci. USA*, 93(13770), 1996.

[174] J. Han, S. W. Turner, and H. G. Craighead. Entropic trapping and escape of long DNA molecules at submicron size constriction. *Phys. Rev. Lett.*, 83(1688), 1999.

[175] J. Han and H. G. Craighead. Separation of long DNA molecules in a microfabricated entropic trap array. *Science*, 288(1026), 2000.

[176] B. Cui, H. Diamant, and B. Lin. Screened hydrodynamic interaction in a narrow channel. *Phys. Rev. Lett.*, 89(188302), 2002.

[177] Q. H. Wei, C. Bechinger, and P. Leiherer. Single-file-diffusion of colloids in one-dimensional channels. *Science*, 287(625), 2000.

[178] H. Lamb. *Hydrodynamics*. Dover, New York, 1945.

[179] L. G. Leal. *Laminar Flow and Convective Transport*. Butterworth-Heinmann, Boston, 1992.

[180] Z. U. A. Warsi. *Fluid Dynamics*. CRC, Boca Raton, 1992.

[181] R. Kubo. The fluctuation-dissipation theorem. *Rep. Prog. Phys*, 29(255), 1966.

[182] H. Risken. *The Fokker-Planck Equation: Methods of Solution and Applications*. Springer, Berlin, 1989.

[183] P. Reimann, C. Van den Broek, H. Linke, P. Hänggi, J. M. Rubi, and A. Perez-Madrid. Giant acceleration of free diffusion by use of tilted periodic potential. *Phys. Rev. Lett.*, 87(010602), 2001.

[184] P. Reimann. Brownian motors: Noisy transport far from equilibrium. *Physics Report*, 361(57), 2002.

[185] P. Hänggi, P. Talkner, and M. Borkovec. Reaction-rate theory: Fifty years after Kramers. *Rev. Mod. Phys.*, 62(251), 1990.

[186] P. Reimann, C. V. Broeck, H. Linke, P. Hänggi, J. M. Rubi, and A. Perez-Madrid. Diffusion in tilted periodic potentials: Enhancement, universality, and scaling. *Phys. Rev. E*, 65(031104), 2002.

[187] M. Khantha and V. Balakrishnan. First passage time distributions for finite one-dimensional random walks. *Pramana*, 21(111), 1983.

[188] B. Lindner, M. Kostur, and L. Schimansky-Geier. Optimal diffusive transport in a tilted periodic potential. *Fluct. Noise Lett.*, 1(R25), 2001.

[189] I. Goychuk, E. Heinsalu, M. Patriarca, G. Schmid, and P. Hänggi. Current and universal scaling in anomalous transport. *Phys. Rev. E*, 73(020101), 2006.

[190] E. Heinsalu, M. Patriarca, I. Goychuk, and P. Hänggi. Fractional diffusion in periodic potentials. *J. Phys. Condens. Matter*, 19(065114), 2007.

[191] S. Jiang and S. Granick. *Janus Particle Synthesis, Self-Assembly and Applications*. PSC Publishing, Cambridge, 2012.

[192] G. Volpe and G. Volpe. Simulation of a Brownian particle in an optical trap. *Am. J. Phys.*, 81(1236), 2013.

[193] P. E. Kloeden and R. A. Pearson. *Numerical Solution of Stochastic Differential Equations*. Springer, Heidelberg, 1999.

[194] K. Franke and H. Gruler. Galvanotaxis of human granulocytes: Electric field jump studies. *Eur. Biophys. J.*, 18(334), 1990.

[195] R. M. Ford and R. W. Harvey. Role of chemotaxis in the transport of bacteria through saturated porous media. *Adv. Water Res*, 30(1608), 2007.

[196] P. K. Ghosh, V. R. Misko, F. Marchesoni, and F. Nori. Self-propelled Janus particles in a ratchet: Numerical simulations. *Phys. Rev. Lett.*, 110(268301), 2013.

[197] P. K. Ghosh, P. Hänggi, F. Marchesoni, F. Nori, and G. Schmid. Directed transport of confined Brownian particles with torque. *Europhys. Lett.*, 98(50002), 2012.

[198] NVIDIA. http://www.nvidia.com/object/cuda_home_new.html.

[199] S. E. Spagnolie and E. Lauga. Hydrodynamics of self-propulsion near boundaries: Predictions and accuracy of far-field approximations. *J. Fluid Mech.*, 700(105), 2012.

[200] D. Takagi, J. Palacci, A. B. Braunschweig, M. J. Shelley, and J. Zhang. Hydrodynamic capture of microswimmers into sphere-bound orbits. *Soft Matter*, 10(1784), 2014.

[201] Giorgio Volpe, S. Gigan, and G. Volpe. Simulation of the active Brownian motion of a microswimmer. *Am. J. Phys.*, 82(659), 2014.

[202] X. Ao, P. K. Ghosh, Y. Li, G. Schmid, P. Hänggi, and F. Marchesoni. Active Brownian motion in a narrow channel. *Eur. Phys. J. Special Topics*, (arXiv:1409.5061[cond-mat.soft]), accepted, 2014.

[203] Y. Li, P. K. Ghosh, F. Marchesoni, and B. Li. Manipulating chiral microswimmers in a channel. *Soft Matter*, Submitted, 2014.

[204] S. Denisov, S. Flach, and P. Hänggi. Tunable transport with broken space-time symmetries. *Phys. Rep.*, 538(77), 2014.

[205] L. Machura, M. Kostur, P. Talkner, J. Luczka annd F. Marchesoni, and P. Hänggi. Brownian motors: Current fluctuations and rectification efficiency. *Phys. Rev. E.*, 70(061105), 2004.

[206] H. Brenner and D. A. Edwards. *Macrotransport Processes*. Butterworth-Heinemann, New York, 1993.

[207] Y. Fily and M. C. Marchetti. A thermal phase separation of self-propelled particles with no alignment. *Phys. Rev. Lett.*, 108(235702), 2012.

[208] R. Fürth. Die Brownsche Bewegung bei Berücksichtigung einer Persistenz der Bewegungsrichtung. Mit Anvendungen auf die Bewegung lebender ii. *Z. Physik*, (244).

[209] M. Borromeo and F. Marchesoni. Particle transport in a two-dimensional septate channel. *Chem. Phys.*, 375(536), 2010.

[210] M. Borromeo, F. Marchesoni, and P. K. Ghosh. Communication: Driven Brownian transport in eccentric septate channels. *J. Chem. Phys.*, 134(051101), 2011.

[211] X. Ao, P. K. Ghosh, Y. Li, G. Schmid, P. Hänggi, and F. Marchesoni. Diffusion of chiral Janus particles in a sinusoidal channel. *Europhys. Lett.*, Submitted,2014.

[212] G. Costantini and F. Marchesoni. Threshold diffusion in a tilted washboard potential. *Europhys. Lett.*, 48(491), 1999.

Acknowledgements

Curriculum Vitae

Date of birth:	26.12.1987
Nationality:	Chinese
Martial status:	single
Parents:	Shuang-Zhi Ao and Xia Bai

Education

9.1993 - 6.1999	Elementary school
9.1999 - 6.2002	Middle school
9.2002 - 6.2005	High school
9.2005 - 6.2009	B. Sc in Physics, Sun Yat-sen University, China
	Thesis title: Review on previous research of Berry phase
	Supervisor: Prof. Shi-Dong Liang
9.2009 - 2.2012	M. Phil. in Physics, Hong Kong Baptist University, Hong Kong
	Thesis title: Study of fluctuations in gene regulation circuits with memory
	Supervisor: Prof. Lei-Han Tang
4.2012 - now	Doctoral studies in Physics, University of Augsburg, Germany
	Thesis title: Active Brownian motion in a narrow channel
	Supervisor: Prof. Peter Hänggi